PROPOSAL
for a Silicon Vertex Tracker
(VTX)
for the PHENIX Experiment

Proposal for a Silicon Vertex Tracker (VTX) for the PHENIX Experiment

M. Baker, R. Nouicer, R. Pak, A. Sukhanov, P. Steinberg
Brookhaven National Laboratory, Chemistry Department, Upton, NY 11973-5000, USA

Z. Li
Brookhaven National Laboratory, Instrumentation Division, Upton, NY 11973-5000, USA

J.S. Haggerty, J.T. Mitchell, C.L. Woody
Brookhaven National Laboratory, Physics Department, Upton, NY 11973-5000, USA

M. Finger
Charles University, Ke Karlovu 3, 12116 Prague, Czech Republic

E.J. Mannel
Columbia University, Nevis Laboratories, Irvington, New York 10533, USA

A.D. Frawley
Florida State University, Tallahassee, FL 32306, USA

T. Kempel, J.G. Lajoie, A. Lebedev, C.A. Ogilvie, H. Pei, A. Semenov, F. Wei
Iowa State University, Ames, IA 56011, USA

L. Tomasek, V. Vrba
Institute of Physics, Academy of Sciences,Na Slovance 2, 182 21 Prague, Czech Republic

M. Tanaka, M. Sekimoto
High Energy Accelerator Research Organization (KEK), Tsukuba, Ibaraki 305-0801, Japan.

N. Saito, M. Togawa
Kyoto University, Kyoto 606, Japan

E.T. Atomssa, S. Chollet, A. Debraine, O. Drapier, F. Fleuret, F. Gastaldi,
R. Granier de Cassagnac, M. Gonin, A. Karar
Laboratoire Leprince-Ringuet, Ecole Polytechnique, CNRS-IN2P3, Route de Saclay, F-91128, Palaiseau, France

H.W. van Hecke, G.J. Kunde, D.M. Lee, M. J. Leitch, P.L. McGaughey, W.E. Sondheim
Los Alamos National Laboratory, Los Alamos, NM 87545, USA

T. Kawasaki, K. Fujiwara

Niigata University, Niigata 950-2181, Japan

T.C. Awes, M. Bobrek, S. Batosouli, C.L. Britton, W.L. Bryan, V. Cianciolo, Y.V. Efremenko, K.F. Read, D.O. Silvermyr, P.W. Stankus, G.R. Young
Oak Ridge National Laboratory, Oak Ridge, TN 37831, USA

Y. Akiba, J. Asai, H. En'yo, Y. Goto, J.M. Heuser, R. Ichimiya, H. Kano, M. Kurosawa, H. Ohnishi, V. Rykov, A. Taketani, K. Tanida, J. Tojo
RIKEN (The Institute of Physical and Chemical Research,) Wako, Saitama 351-0198, Japan

P. Liebing
RIKEN BNL Research Center, Brookhaven National Laboratory, Upton, NY11973-5000, USA

Y. Inoue, M. Kawashima, K. Kurita
Rikkyo University, Toshima, Tokyo 171-8501, Japan

S. Abeytunge, R. Averbeck, R. Bennett, K. Boyle, A. Deshpande , A. Dion, A. Drees, T.K. Hemmick, B.V. Jacak, M. Nguyen, C. Pancake, V.S. Pantuev, H.W. Themann
Stony Brook University, Department of Physics and Astronomy, Stony Brook, NY 11794, USA

T.-A. Shibata, K. Sakashita
Tokyo Institute of Technology, Meguro, Tokyo 152-8551, Japan

B. Bassalleck, D.E. Fields, C. Haegemann, M. Hoeferkamp, M. D. Malik, J. Turner, A. Zimmerman
University of New Mexico, Albuquerque, NM 87131, USA

List of Figures

List of Tables

1. Executive Summary

We propose the construction of a Silicon Vertex Tracker (VTX) for the PHENIX experiment at RHIC. The VTX will substantially enhance the physics capabilities of the PHENIX central arm spectrometers. Our prime motivation is to provide precision measurements of heavy-quark production (charm and beauty) in *A+A*, *p(d)+A*, and polarized *p+p* collisions. These are key measurements for the future RHIC program, both for the heavy ion program as it moves from the discovery phase towards detailed investigation of the properties of the dense nuclear medium created in heavy ion collisions, and for the exploration of the nucleon spin-structure functions. In addition, the VTX will also considerably improve other measurements with PHENIX. The main physics topics addressed by the VTX are:

- Hot and dense strongly interacting matter
  - Flavor dependence of jet quenching and QCD energy loss
  - Flavor dependence of elliptic flow
  - Open beauty production
  - Accurate charm reference for quarkonium
  - Potential enhancement of charm production
  - Thermal dilepton radiation
  - High p_T phenomena with light flavors above 10-15 GeV/c in p_T
  - Di-jet hadron correlation
  - Upsilon spectroscopy in the e^+e^- decay channel

- Gluon spin structure of the nucleon
  - $\Delta G/G$ with charm
  - $\Delta G/G$ with beauty
  - x dependence of $\Delta G/G$ with γ-jet correlations

- Nucleon structure in nuclei
  - Gluon shadowing over broad x-range

With the present PHENIX detector, heavy-quark production has been measured indirectly through the observation of single electrons. These measurements are limited in accuracy by systematic uncertainties resulting from the large electron background from Dalitz decays and photon conversions. In particular, the statistical nature of the analysis does not allow for a model-independent separation of the charm and beauty contributions.

The VTX detector will provide vertex tracking with a resolution of <50 μm over a large coverage both in rapidity ($|\eta| < 1.2$) and in azimuthal angle ($\Delta\phi \sim 2\pi$). With this device, significantly enhanced and qualitatively new data can be obtained. A more robust and accurate measurement of heavy-quark production over a wide kinematics range will be possible.

The main benefits are in three areas. Firstly, by selecting electrons with a distance of closest approach (DCA) to the primary vertex larger than ~100 μm, the background will be suppressed by several orders of magnitude and thereby a clean and robust measurement of heavy flavor production in the single electron channel will become available. Secondly, because the lifetime of mesons with beauty is significantly larger than that of mesons with charm, the VTX information will allow us to disentangle charm from beauty production over a broad p_T range. Thirdly, a DCA cut on hadrons will reduce the combinatorial background of $K\pi$ to an extent that a direct measurement of D mesons through this decay channel will become possible. In addition, the VTX detector will substantially extend our p_T coverage in high p_T charged particles, and it also will enable us to measure γ+jet correlations.

The proposed VTX detector has four tracking layers. To avoid cost intensive and time consuming R&D, we have investigated to what extent existing technology can meet our needs. For the inner two layers we will use a silicon pixel device with 50×425 μm pixels that has been developed for the ALICE experiment at the CERN LHC. Our technology choice for the outer layers is a silicon strip detector developed by the Instrumentation Division at BNL. With stereoscopic strips of 80 μm × 3 cm, these devices achieve an effective pixel size of 80 × 1000 μm. We will use the SVX4 readout chip developed at FNAL to readout the strip detectors.

With the help of institutional contributions PHENIX was able to maintain a well focused effort over the past three years to gain experience with these technologies and to launch the necessary R&D to adapt them to the PHENIX requirements. We are ready to start the detector construction at the beginning of FY07.

A collaboration of 97 members from 20 institutions has formed to carry out the project. The collaboration brings in expertise in all phase of the construction of a silicon vertex detector, design and commissioning of modern readout electronics, mechanical and integration issues, detailed knowledge of all aspects of the PHENIX experiment as well as expertise in data analysis and a broad interest in different physics aspects addressed by the VTX.

We anticipate that the project will be funded by two agencies, the DOE Office of Nuclear Physics and the RIKEN Institute of Japan. For a successful completion of the project we propose clear responsibilities and scope of deliverables for both agencies. A management plan of the VTX detector project, which also discusses the role and expected responsibilities of the participating institutions, accompanies this proposal.

We propose to construct the VTX detector over a period of FY07 to FY09. Parts of the detector will be ready and installed. The project will be completed in FY09. To carry out this project we seek funding of a total of $4.6M through DOE. These funds would be supplemented with deliverables equivalent to about $3M US dollar provided by the RIKEN from 2004.

The proposal has the following structure. The physics motivation for the upgrade and the proposed measurements are documented in section 2. The feasibility of these measurements and the required detector performance are discussed in section 3. Section 4 gives a detailed description of the vertex tracker and the technical aspects of the proposed project. A draft of our management plan, section 5, specifies deliverables and institutional responsibilities. Section 6 lays out the budget request and the proposed schedule.

2. Physics Overview

Heavy-flavor production provides a wide-ranging palette of key information in three broad areas of physics addressed by the relativistic heavy ion collider RHIC at Brookhaven National Laboratory. Current experiments at RHIC are inadequately equipped to fully exploit the opportunities heavy-flavor production provides. Many of the necessary measurements are either not possible or can be performed only with very limited accuracy. Precise vertex tracking is imperative for a robust measurement of heavy-flavor production. The proposed VTX detector adds tracking capabilities to the central arms of the PHENIX experiment. With this detector charged particles detected in the central arms can be identified as decay products from charm- or beauty-carrying particles by the displacement of their trajectories to the collision vertex. A broad p_T range for charm and beauty measurements is achieved by using different decay channels to reach different parts of phase space.

The addition of the VTX to PHENIX will significantly extend the physics program of PHENIX. In heavy ion collisions open charm and beauty production will provide essential new data on the high-density matter created early during the reaction. Specifically, these measurements will determine:

- mass dependence of the energy-loss of partons in the medium, which has already been observed for light partons.
- mass dependence of the elliptic flow of quarks
- if heavy-quarks are produced only in the initial parton-parton collisions or also during the later phases of the collision.
- a firm baseline to quantify the suppression or possible enhancement of J/ ψ.
- the rate of thermal dilepton emission quantitatively.
- quark confinement forces at larger binding energies via the yield of upsilon states.

Measurements of open beauty in polarized $p+p$ reactions add new channels in which the gluon spin structure function of protons can be measured. Robust charm measurement and jet reconstruction over large acceptance significantly extend the x-range of the currently possible measurements. In $p+A$ reactions shadowing of the gluon structure function in nuclei can be addressed both with open charm and beauty measurements.

2.1 Probes of Early, Highest Energy-Density Stage of Heavy-ion Reactions

From the wealth of data obtained from the first three years of RHIC operation, the four RHIC experiments have concluded that a high density partonic matter is formed at central Au+Au collisions at RHIC[1,2,3,4]. The research focus now shifts from the initial discovery phase to a detailed exploration of quark matter. Charm and beauty production, measured as yield and spectra of heavy flavor mesons, provide information about the earliest stages of heavy ion collision. Several key measurements discussed in these sub-sections can be made with the addition of the proposed VTX detector to PHENIX. Of particular importance is the broad reach in transverse momentum, which extends PHENIX's existing capability to measure low-p_T open charm.

PHENIX has extracted the cross-section for open charm via inclusive electron spectra[5,6,7]. This method relies on the fact that a fraction of the electrons originates from decays of heavy-flavor mesons (charm or beauty) and on the ability to subtract the large background from light-meson decays. This procedure suffers from uncertainties due to the limited knowledge of the background sources that are subtracted. In addition, one can not distinguish electrons from charm and beauty at high p_T where the contributions from the two sources become comparable.

The addition of a silicon vertex detector to PHENIX will allow more accurate determination of the heavy-quark component in electron spectra. Requiring the leptons to be displaced from the collision will substantially reduce the background and thus extend the range of the charm measurement to smaller p_T. At moderate and high p_T decays of beauty-flavor mesons also contribute to the single-electron spectrum. The present PHENIX detector cannot distinguish the charm from the beauty contribution and thus our ability to measure charm is limited to $p^e_T < 2.5$ GeV/c, i.e. the range where charm is the dominant source of single electrons after background subtraction. The proposed upgrade adds the capability to detect charm and beauty production separately with high accuracy, which will enable us to measure not only the yield of open beauty production but also to extend the charm measurement to higher p_T. Complementary to the measurement of inclusive electrons with displaced vertex, at high p_T we can also measure exclusive decays such as $D \to K\pi$.

With the extended capability of heavy quark measurement with the VTX detector, we can address the following critical questions.

Energy-loss of heavy-quarks

Colored high-p_T partons are predicted to lose energy as they propagate through the dense nuclear medium [8]. The dominant mechanism is likely medium-induced gluon radiation [9,10] with a smaller contribution from elastic collisions with lower-energy partons. This predicted parton energy loss has been observed at RHIC as strong suppression of high p_T hadrons in central Au+Au collisions [11,12]. The absence of such suppression in d+Au collisions [13] or in direct photon production [14] has confirmed that it is a medium effect. Figure 1 shows nuclear modification factor data for π^0, η, and direct photon measured by PHENIX [15]. For light hadrons, strong suppression of a factor of ~5 is observed, while direct photon is not suppressed. This "jet quenching" effect is the key evidence of formation of dense partonic matter at RHIC.

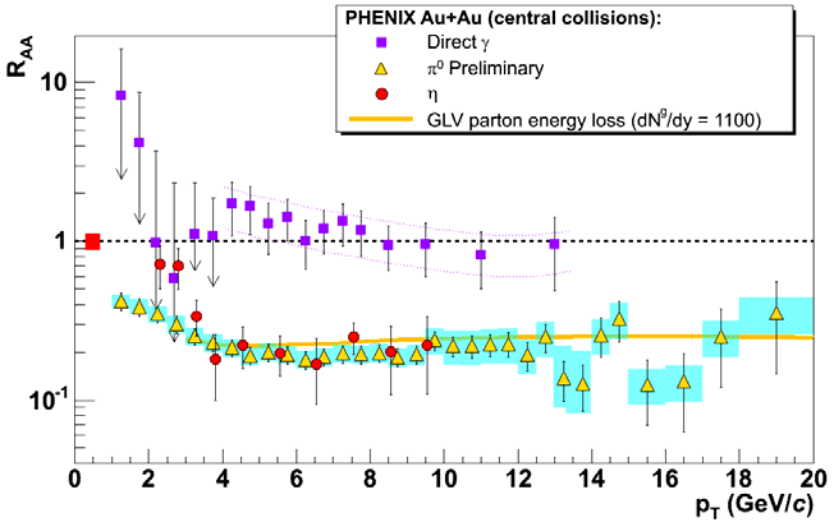

Figure 1 Nuclear modification factor of π^0, η, and direct photon in central Au+Au collisions.

Gluon radiation and energy-loss are exquisitely sensitive to interference effects, since the gluon formation time is comparable to the time between successive collisions. Hence before we can quantitatively use the measured energy-loss as a probe of the dense medium, we need to be confident that the interference effects in the model calculations are well tested by data. One powerful strategy is to change the amount of gluon-interference by using heavy-quarks instead of light quarks.

Heavy-quarks are predicted [16] to lose less energy in the plasma because of the "dead-cone effect". Qualitatively the large quark mass eliminates the favored collinear gluon Bremsstrahlung. It also shortens the gluon formation time and leads to a distinctly different destructive interference around the heavy-quark's trajectory. Figure 2 shows the ratio of jet quenching factor Q_H/Q_L for heavy quarks (Q_H) and light quarks (Q_L) as function of the p_T of the quark calculated

in reference [16]. The smaller energy loss due to the "dead cone" effect leads to a factor of 2 less suppression of high p_T charm quarks compared to light quarks.

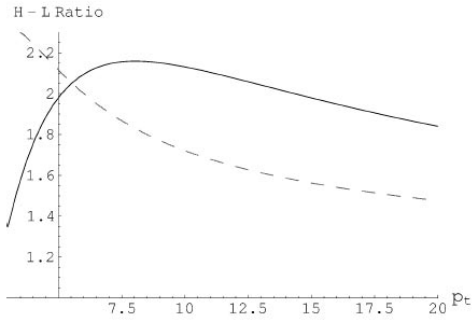

Figure 2 Ratio of Jet Quenching factor QH/QL of heavy quark (QH) and light quark (QL) in high density QCD medium as function of pT of the quark, from ref. [16]. The solid line is with no energy cut-off for gluon and the dashed line is with cut off of 0.5 GeV.

More recent theoretical studies suggest that the magnitude of the dead-cone[17,18,19] may be smaller than anticipated in reference [16], which would lead to an energy-loss for heavy quarks closer to that for light quarks. Djordjevic and Gyulassy[17,18] have proposed that the energy-loss for heavy-quarks is further reduced due to a plasmon frequency cut-off effect in a thermalized medium. As a result precise measurement of heavy-quark energy loss through open charm may enable a measurement of partonic effective thermal masses in the medium.

Recently, suppression of high p_T electrons from heavy quark decay in central Au+Au collision has been observed[20,21]. The PHENIX data of nuclear modification factor of high-p_T single electrons are shown in Figure 3. The observed suppression is surprisingly strong, and it is comparable to that of light hadrons. The data provide strong constraints on the energy loss models. It is particularly remarkable that the suppression is strong at high p_T (> 3 GeV/c) where the contribution from beauty decay is expected to be dominant, since in most energy loss models little or no energy loss of beauty is expected in the dense matter created at RHIC.

The present PHENIX can not distinguish single electrons from charm decay and from beauty decay in Au+Au collisions. Thus we can not determine the suppression factor of charm accurately, nor we can determine if beauty also suffer significant energy loss or not. The VTX detector allows us to measure the single electrons from charm and beauty separately. Since beauty has a larger $c\tau$ (B^0: 462 μm, B^+: 502 μm) than charm (D^0: 123 μm, D^+: 317 μm), we can accurately split the beauty component of single electron from the charm component using a precise displaced vertex measurement from the VTX. The

VTX detector will also allow us to measure to measure the high-p_T spectra of charm directly via the hadronic decay channels, e.g. $D \rightarrow K+\pi$. From these measurements, we will be able to determine the energy loss of charm and beauty in the medium. This will be a decisive measurement to understand the energy loss mechanism in the dense matter at RHIC.

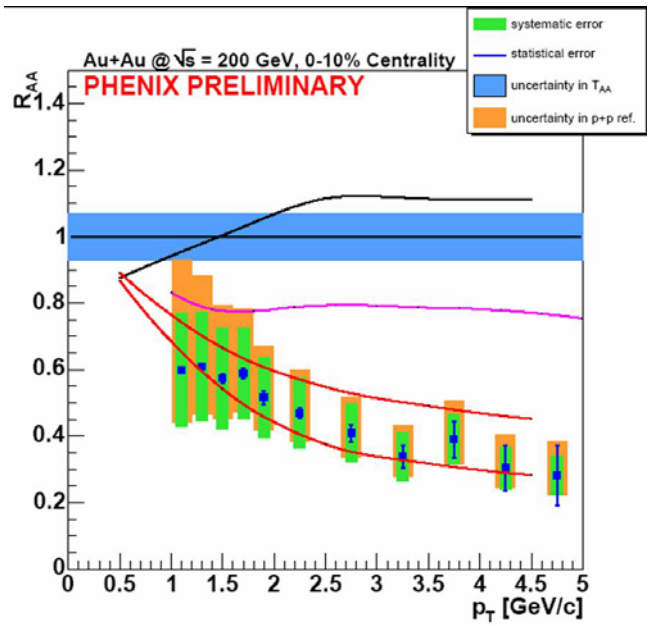

Figure 3 Nuclear modification factor of single electrons measured by PHENIX is compared with the theoretical predictions. The black curve is the theoretical prediction with no charm energy loss. The two red curves are prediction by N. Armestro[22], and the magenda curve is prediction by M. Djordjevic[23]. The latter includes the contribution from beauty, which reduces the suppression at high p_T.

Elliptic flow of heavy quarks and its mass dependence

Event anisotropy is one of the most important observables in nucleus-nucleus collisions at RHIC. The large anisotropy amplitude, v_2, provides key evidence of the formation of a hot and dense partonic matter in Au+Au collisions at RHIC. Along with the discovery of jet quenching, the observation of large v_2 in Au+Au collisions is the basis of the conclusion in the RHIC white papers that a high density partonic medium is formed.

In early RHIC runs, the measurements of v_2 were mainly focused on that of light hadrons in low p_T (p_T < 2-3 GeV/c). Here the anisotropy is produced by the elliptic flow, and hydro-dynamical models can describe

the data very well. Precise measurements of the v_2 as a function of p_T and particle species provide rich information on the properties of the fluid. Good agreement between the data and theory predictions of ideal hydrodynamic models indicate that the produced dense matter thermalizes very rapidly, and that the produced matter behaves almost as an ideal fluid.

Recently, we have observed that event anisotropy is not limited to light hadrons. We observed a large v_2 of single electrons from heavy quark decay. Figure 4 shows the preliminary data of the v_2 of single electrons from heavy quark decay (mixture of charm and beauty) presented at Quark Matter 2005. The data at low p_T favor the models that include quark level elliptic flow of charm. The large v_2 of charm decay electrons is a surprising discovery, and it shows that even heavy quarks participate in the collective motion of the produced matter. The data pose a challenge to the theories of energy loss and thermalization mechanism of heavy quarks in the dense matter.

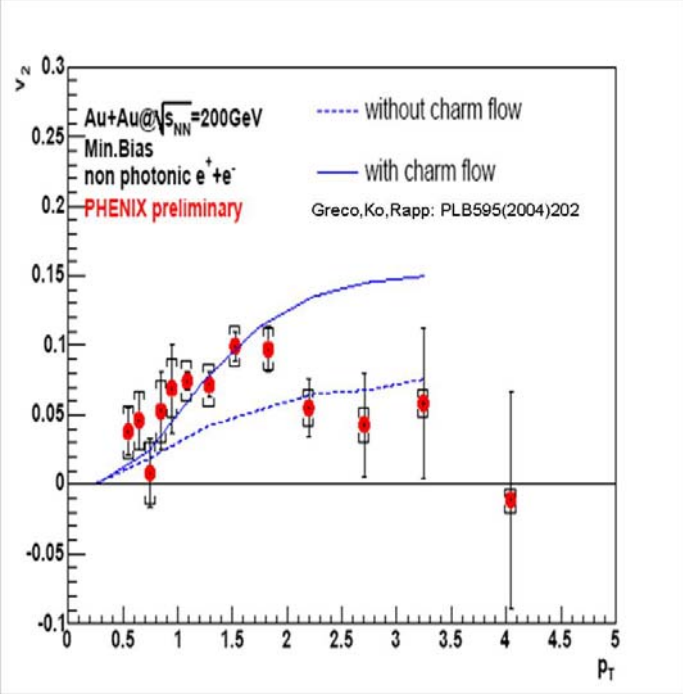

Figure 4 Elliptic flow strength, v2, of single electrons from heavy flavor decay measured by PHENIX. A strong elliptic flow is evidence for strong coupling QGP.

As it is written previously, the present PHENIX detector can not distinguish single electrons from charm and beauty. Therefore, we can not determine v_2 of charm and beauty separately. In the data shown in Figure 4, it is very intriguing that the v_2 strength seems to be reduced at high p_T (p_T > 2.5 GeV/c) where significant B decay contribution is expected. The v_2 of the beauty quark is expected to be small due to its large mass. Separation of charm and beauty components by the VTX detector will enable us to measure v_2 of charm and beauty separately. Together with the v2 data of light mesons, we will be able to complete quark mass dependence of the elliptic flow. Such measurements will be the key to understand the interaction between the medium and the partons in the medium.

<u>Open Beauty Production</u>

Beauty quarks are predominantly produced by the initial parton-parton collision. Because of the large mass almost no additional production is expected from the pre-equilibrium stage or thermalized phase. As a consequence, the measurement of open beauty is ideally suited to probe the parton density in the coming nucleus and thus the initial parton luminosity.

The open beauty yield can be measured via inclusive electron production, or more directly through its decay $B \rightarrow J/\psi + X$ (B.R. 1.14%). The VTX detector is essential for the detection of both channels. In the single electron measurement, we cannot distinguish single electrons from open charm and open beauty with the present PHENIX detector. Below p_T ~ 2.5 GeV/c the open charm contribution to the non-photonic electron spectrum, which is the inclusive electron spectrum after subtraction of the light meson decay background, is much larger than that of beauty. Thus, it is not possible to determine the open beauty component in this low p_T range. This is the p_T range that contains about 90% of the electrons from beauty decays. Even in the high p_T region (p_T>3 GeV/c), where beauty is expected to be the leading source of non-photonic electrons, there is a large uncertainty due to the unknown charm contribution. Again, precise vertex measurement by the VTX detector will enable us to clearly separate charm and beauty.

The VTX also enables us to measure the $B \rightarrow J/\psi + X$ decay by tagging J/ψ's with a vertex detached from the collision point. Although this mode has a small cross section, it gives a clean signal of B in wide momentum range, down to p_T = 0.

Open charm reference to J/ψ suppression and enhancement

In the J/ψ studies done at CERN by NA38/50[24] the J/ψ yields were usually determined relative to the Drell-Yan di-muon yields with the argument that the latter should have little final-state nuclear dependence. But it is not clear how reliable this comparison really is since the Drell-Yan process involves quarks ($q\bar{q}$ annihilation) while J/ψ production involves gluons (gluon fusion). It is likely that the nuclear effects on the initial parton distributions for quarks and gluons as well as their energy loss in the initial state before the hard interaction are different. Additionally, the yield of Drell-Yan dimuon pairs is quite small and thus limits the statistical accuracy of the measurement. It seems much more natural to compare J/ψ production to open-charm production, where the initial-state effects are probably the same. Therefore a robust measurement of open-charm is quite important for the physics of the J/ψ. At CERN this is now provided by the NA60 experiment. It has also been suggested by some theoretical groups[25] that the effective gluon distributions are process dependent, and different for e.g. open- and closed-charm production. These models suggest that comparisons of open and closed charm are important to establish the extent of higher-twist contributions to closed charm production.

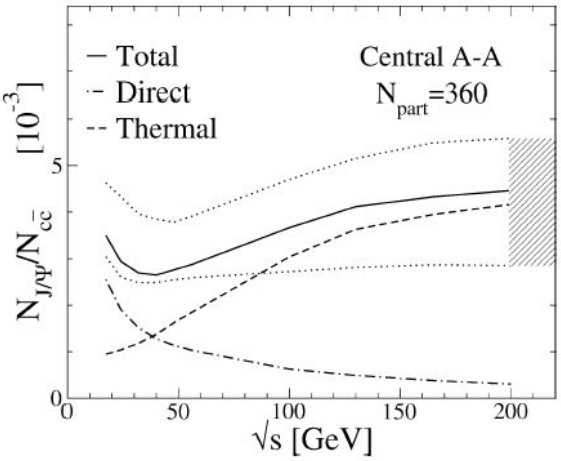

Figure 5 The ratio of J/Ψ yield and open charm yield predicted in ref. [26]

Recently, a new mechanism for charmonium production in high-energy nucleus-nucleus collisions has been proposed[26,27,28]. The basic idea is that charmonium can be formed by re-combination of c and $\bar{c}$ quarks when the bulk of the hadrons are formed. Since about 10 to 20 $c\bar{c}$ pairs are produced in a single event in central Au+Au collisions at RHIC, this contribution can be very significant. It has been predicted that the charmonium yield increases with the square of the open charm yield. Figure 5 shows a prediction of reference [26], one of the recombination models. In this model, the ratio of J/ψ yield over open

charm yield has a minimum at $\sqrt{s}$ ~ 40 GeV due to interplay between J/ψ suppression in QGP and J/ψ formation via recombination mechanism. An accurate measurement of charmonium to open charm ratio over a broad range of impact parameters and collision energies is essential to test these models.

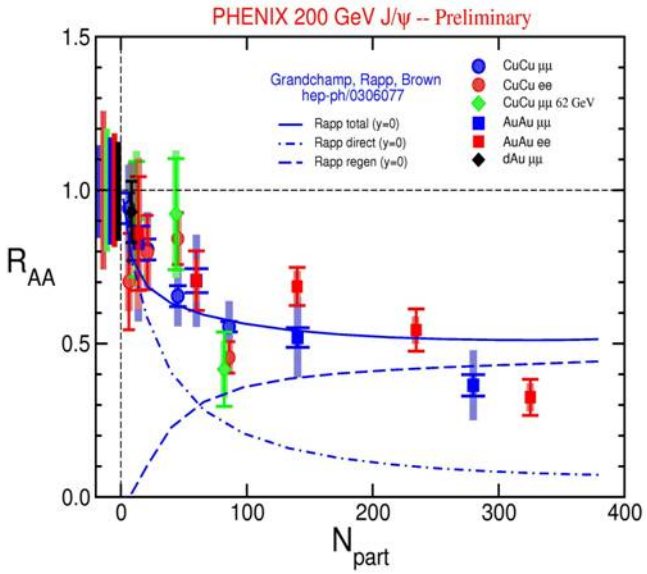

Figure 6 PHENIX data of J/ψ suppression at RHIC as function of participants nucleon (Npart) are compared with a theoretical prediction by Rapp et al.

Figure 6 shows preliminary data of J/ψ suppression in Au+Au and Cu+Cu collisions at RHIC. The data are compared with the model predictions by R. Rapp. The model includes the strong suppression due to QGP formation as well as re-generation of J/ψ by recombination of charm pairs. The strong suppression due to QGP formation is compensated by the recombination mechanism, and the model qualitatively explain the data. However, it should be noted that the charm yield from the recombination is sensitive to the total charm yield. Therefore, a precise measurement of open charm is imperative to understand the J/ψ suppression and formation at RHIC.

Open beauty and J/ψ suppression

Another important area, especially for J/ψ measurements, is the production of beauty quarks. The decay of B mesons will produce J/ψ's (BR ~ 1.14%) that tend to have somewhat higher p_T than prompt J/ψ production. In a scenario where color-screening in a QGP destroys most of the primary J/ψ's, it is conceivable that a large fraction of the observed J/ψ's comes from B decays. An estimate by Lourenco[29] several years ago indicated that for central collisions the fraction of J/ψ's from B decays might be as large as 20% overall, with even

larger fractions at high p_T. Clearly one would like to measure the B cross sections at RHIC energies so that a more reliable estimate of their contribution to the J/ψ production can be made, an issue which would be particularly important should a large suppression of J/ψ's be seen in central Au-Au collisions at RHIC. How strong the suppression actually is will be difficult to quantify without establishing how many of the remaining J/ψ's do come from B decays.

Potential enhancement of open charm production

It has been predicted that open charm production could be enhanced in high-energy nucleus-nucleus collisions relative to the expectation from elementary collisions[30,31,32]. Heavy quarks are produced in different stages of a heavy ion reaction. In the early stage charm and beauty are formed in collisions of the incoming partons. The yield of this component is proportional to the product of parton density distribution in the incoming nuclei (binary scaling). If the gluon density is high enough a considerable amount of charm can be produced via fusion of energetic gluons in the pre-equilibrium stage before they are thermalized. Finally, if the initial temperature is above 500 MeV, thermal production of charm can be significant. The last two mechanisms (pre-equilibrium and thermal production) can enhance charm production relative to binary scaling of the initial parton-parton collisions. These are the same mechanisms originally proposed for strangeness enhancement, but in the case of charm may reveal more about the critical, early partonic-matter stage of the reaction since the rate of heavy-quark production is expected to be negligible later in the reaction when the energy density has decreased. In comparison, strangeness production is expected to continue even in the later hadronic stages of the reaction.

At RHIC energies the anticipated enhancement is small effect[31,32]. The contributions to charm production from various stages of an Au+Au collision are shown in Figure 7 (taken from reference 31). From the left panel of the figure it is evident that for an initial energy density of 3.2 GeV/fm^3 the pre-thermal or pre-equilibrium production contributes about 10% of total charm production, while the thermal contribution is negligible. However, the yield is very sensitive to the initial density, and with 4 times the energy density the pre-equilibrium contribution can be as large as the initial fusion. This is illustrated in the right panel of the figure. Present single electron measurements of PHENIX indicate that within ~25% systematic uncertainty charm production approximately scales with the number of binary collisions. Thus, charm enhancement, if it exists, cannot be a large effect. A measurement

of the charm yield with substantially higher accuracy and precision is therefore required to establish a potential charm enhancement.

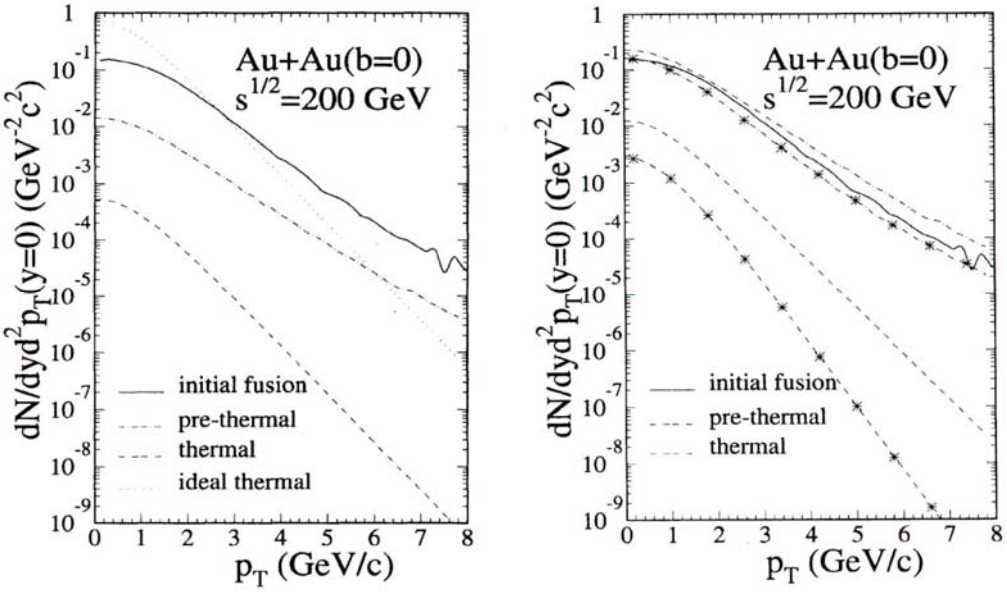

Figure 7 Charm enhancement expected at RHIC energy from ref. 3 1 . In both panels, contribution from the initial gluon fusion (solid), pre-thermal production (dot-dashed), and thermal production (dashed, lowest) are shown. The left panel is the calculation with energy density of 3.2 GeV/fm^3, while the right panel shows the case with energy density 4 times higher.

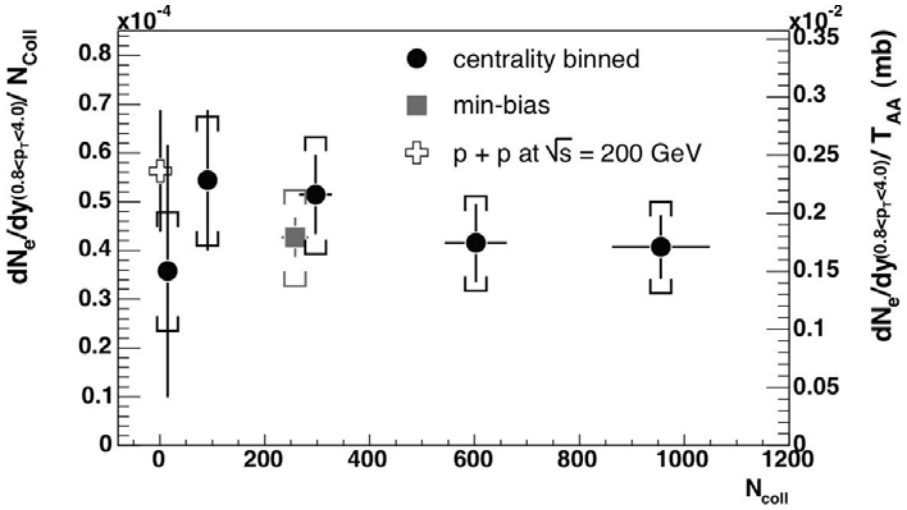

Figure 8 Yield of single electrons from heavy flavor decay per binary N+N collision measured by PHENIX. Within systematic uncertainties of ~25%, the heavy flavor production (mainly charm at his low pT) is consistent with the binary collision scaling.

The VTX detector will improve the accuracy of charm measurement through single electrons by significantly reducing the background from Dalitz and photon conversions. This will extend the single electron measurement to the p_T region below 0.5 GeV/c, which is essential for an accurate determination of the total charm yield since more than half of the single electron yield from charm decay is in this p_T region.

Ratio of charm and beauty production and its centrality dependence

One of the interesting opportunities opened by a beauty measurement using the VTX is the extraction of the $(c \rightarrow e)/(b \rightarrow e)$ ratio as function of the collision centrality. In this ratio, most of the systematic uncertainties including acceptance, reconstruction efficiency, luminosity, and number of collisions per event cancel. In addition, since little or no enhancement of beauty relative to binary scaling is expected at RHIC energy, the denominator $(b \rightarrow e)$ may serve as a precise monitor of the initial parton luminosity, a role similar to that of Drell-Yan production of muon pairs for J/ψ suppression measurement by NA50. This ratio could provide a very sensitive method to observe a small charm enhancement like it was discussed in the previous section. As discussed in section 3.6, we could obtain an accuracy of the centrality dependence of this ratio close to ~1 % in statistical precision.

Thermal di-lepton and open charm

The hot and dense system that is created at RHIC should emit electro-magnetic radiation during its time evolution, either in the form of real photons, or in the form of virtual photons, which materialize as lepton pairs. This thermal electro-magnetic radiation directly probes the dense medium. The production rate of the thermal di-leptons is a steep function of temperature, and thus an accurate measurement may enable us to determine the initial temperature of the system.

There are several processes that contribute to the di-lepton continuum. Qualitatively, the Drell-Yan process dominates the high-mass region, while thermal pairs from the hadron gas dominate the low-mass region. At RHIC energies, thermal radiation from the quark-gluon plasma is predicted to be the major source of di-leptons in the intermediate mass region of $1<M_{ee}<3$ GeV. In this mass range thermal radiation competes with a large background from semi-leptonic decays of correlated $D\overline{D}$ pairs. Figure 9[33] compares predictions for the thermal di-electron continuum above the ϕ resonance to di-leptons from open charm. The di-electron yield from open charm is comparable to the thermal di-lepton signal at M_{ee}=1 GeV, and is two to three times as large in the mass range of 1.5 to 2.5 GeV.

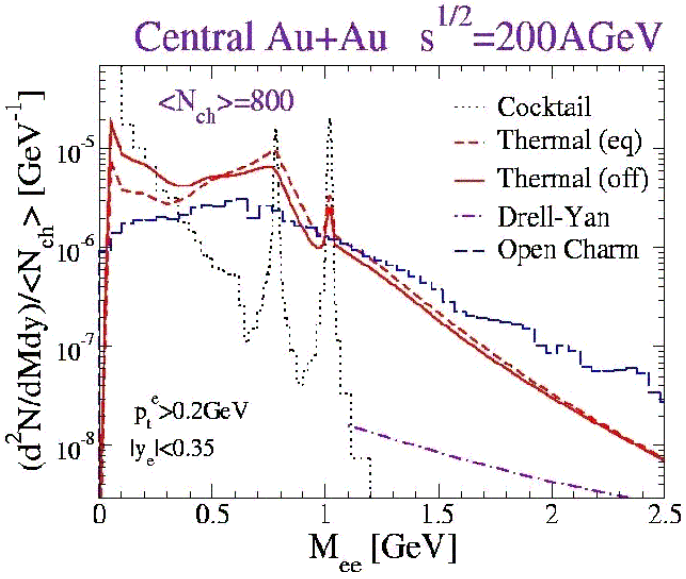

Figure 9 The di-electron effective mass distribution in PHENIX central arm acceptance in central Au+Au collision at $\sqrt{s_{NN}}$ = 200 GeV predicted by Rapp[3] [3]. In the intermediate mass region (1 < Mee < 2.5 GeV), the dominant sources of electron pairs are open charm and thermal radiation from the QGP and hot hadronic gas.

Figure 10 show the preliminary PHENIX data of di-electron continuum. The data demonstrates that the PHENIX can measure di-lepton continuum in low to intermediate mass range, although the present data is limited by systematic and statistical uncertainties due to subtraction of large combinatorial background. Remarkably, the data shows that the continuum yield in intermediate mass (1 < M < 3 GeV) is consistent with that expected from correlated charm pair decay. Significant improvement in continuum measurement is expected in near future when Hadron Blind Detector, another PHENIX upgrade under construction, is installed. However, improvement of the continuum measurement alone is not sufficient. From the expected relative strength of charm and thermal signal shown in Figure 9, it is clear that one cannot extract the thermal dilepton yield without knowledge of open charm contribution. Knowledge of single electron production from open charm is insufficient to subtract this contributions, since the mass of the di-lepton also depends on the correlation between the D and $\overline{D}$ mesons. Thus it is imperative to directly measure the di-lepton spectrum from correlated charm pairs in order to observe and to accurately determine the thermal di-leptons from the quark-gluon plasma. This measurement will only be possible with the VTX upgrade.

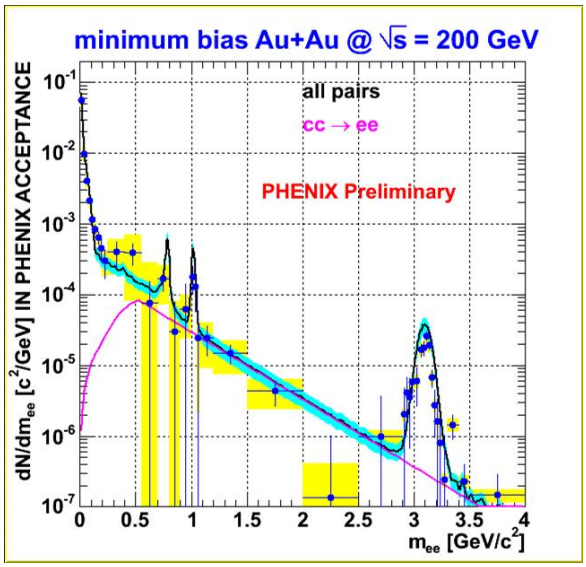

Figure 10 Preliminary PHENIX data of di-electron continuum.

High p_T phenomena with light flavor in 10 – 15 GeV/c in p_T

The suppression of the high p_T particle production is probably the most direct evidence of formation of very dense matter in high-energy nucleus-nucleus collisions at RHIC so far. The creation of dense matter is now firmly established from the high p_T data in Au+Au collision and the comparison data in d+Au collisions. The natural next step is to extend the data, now in p_T range of up to 10 GeV/c, to reach much higher p_T to study the nature of the high p_T suppression.

In the present PHENIX detector, the p_T range of the charged particle measurement is limited to 10 GeV/c in p_T due to a large background from photon conversion and decay in flight of light mesons. The present central arm spectrometer suffers from these backgrounds since it measures particle tracks only outside of the magnetic field. Thus, it cannot distinguish a real high p_T track that originates from the event vertex from a background track that is produced far from the vertex either by photon conversion or by decay-in-flight. The VTX detector will eliminate these backgrounds by providing additional tracking near the event vertex. In addition, the VTX measurement will improve the p_T resolution by about a factor of three (see 3.4) by measuring the initial emission angle of the track in a slightly increased magnetic field. Combined, the p_T range of the charged particle measurement in PHENIX will be extended to beyond 15 GeV/c or more, and will be limited only by the statistics.

Di-jet correlation and gamma-jet correlation

Another benefit of the VTX detector is measurement of di-jet correlation of two high-p_T particles, and direct photon-hadron correlation. Recently, a strong modification of di-jet correlations of two high p_T particles is observed[15,34], as shown in Figure 11. The cause of the modification is not well understood. It could be exotic effect like Mach none[35] or Cereknov like radiation[36], or some more conventional effect.

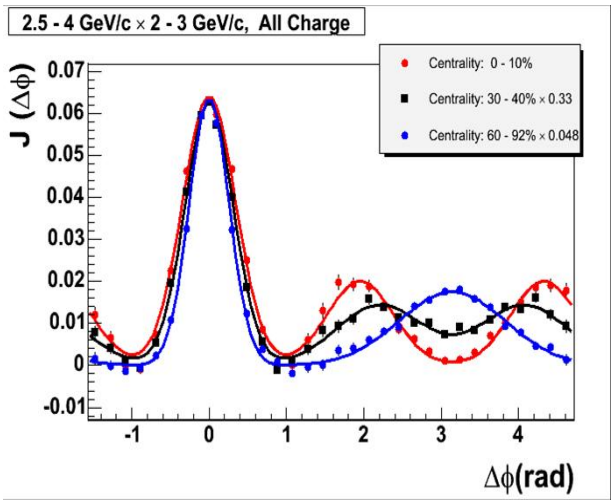

Figure 11 Modification of two particle angular correlation in Au+Au collisions with different centralities.

The VTX detector provides a large solid angle coverage that is ideal for di-jet hadron correlation measurement. Although the momentum resolution by the VTX detector alone is rather limited (about 20 % in δp/p), the resolution is sufficient for selecting high p_T hadrons from the recoil jets. The large η coverage ($|\eta| < 1.2$) of the VTX is in particular essential for the measurement. Similarly, we will be able to utilize the VTX detector in direct photon-hadron correlation measurement in heavy ion collision. This measurement is very important, since one can directly measure the modification of parton fragmentation by the dense medium.

Measurement of Upsilon states

Given sufficient RHIC luminosity, we will be able to measure the ϒ-states ($b\bar{b}$ bound states), and to compare closed and open-beauty production. It is particularly interesting to measure the relative yield of the three ϒ states, as we can study the suppression of heavy quarkonia as function of the binding energy in a region of large binding energy that is not accessible by charmonium production. In addition, unlike charmonium, the contribution to ϒ production

due to quark recombination must be negligible since the number of $b\bar{b}$ pairs produced in an event is very small. Thus in the ϒ production we can directly access the de-confinement effect in dense matter. As mentioned previously with the VTX detector, the momentum resolution will be improved by about factor three, which reduces the mass resolution to ~ 60 MeV so that a clean separation of the 1S, 2S and 3S ϒ states becomes possible. However, this measurement will only be possible if luminosities significantly above the RHIC design value of 2×10^{26} cm^{-2} are reached.

2.2 Determination of spin structure of nucleon.

Exploring the spin structure of the nucleon: The past

Most of what we know about the origin of the nucleon spin comes from Deep Inelastic Scattering (DIS) experiments performed over the last three and half decades. These experiments used polarized electron or muon beams in the momentum range 20-200 GeV/c to impinge on stationary polarized gaseous or solid-state targets. The partonic interaction that occurs in such experiments is between the virtual photons (coming from the polarized lepton beams) and the quarks inside the nucleons of the stationary targets. Naturally, DIS is an excellent probe of the quark polarization in the nucleons. In the late 1980s, measurements were made for the first time at higher energies and a significant deficit in the quark contribution to the nucleon spin was discovered. Often called in the literature "Spin Crisis", the quest to understand this deficiency has driven the experimental and theoretical work in the field of nucleon spin since then. Where is the rest of the nucleon spin? The obvious place to look is the gluons and to measure their contribution. The virtual photons in the DIS only interact weakly with the gluons, as such, one can access the gluon spin dynamics in DIS only through scaling violations of spin structure functions which requires their measurement over a large range of x and Q^2. As of today, such an experimental facility is unavailable and so one has to consider other techniques and tools to access the gluon spin.

Gluon polarization measurement at RHIC:

The new tool that we have been waiting for is the Relativistic Heavy Ion Collider (RHIC). It enables collisions between polarized proton beams at high energy (up to 250 GeV/c). The expected luminosities at these top beam energies are $2\text{x}10^{32}$ cm^{-2} sec^{-1}. As of now, 100 GeV/c polarized protons have been collided

with a few x 10^{30} cm^{-2} sec^{-1} luminosity. Since protons are abundant sources of gluons, polarized proton-proton collisions allows a direct exploration of the gluon spin dynamics at the partonic level. The differences in the hadronic final states originating from gluon-gluon and quark-gluon interactions in the polarized proton collisions measured by the detectors when the proton spins in the two colliding beams are aligned vs. anti-aligned gives us access to the gluon spin contribution to the proton. For a partonic interaction of the kind ($a+b\rightarrow c+d$) occurring in polarized $p+p$ collisions, assuming factorization one can write:

$$A_{LL} = \frac{\Delta a}{a}\frac{\Delta b}{b} a_{LL}(a+b \rightarrow c+d) \qquad (1)$$

Here $\Delta a/a$ and $\Delta b/b$ are the ratios of polarized to unpolarized distributions for parton distributions of a and b respectively, and a_{LL} is partonic analyzing power calculable in pQCD. A_{LL} is the double spin asymmetry measured in the experiment as a result of the polarized proton proton scattering for the final state in which c and d are created and measured in the detector. In this particular example, either a or b or both could be gluon distributions in the colliding protons.

In the PHENIX experiment we will measure gluon spin polarization $\Delta G/G$ using many different processes. A partial list includes gg, gq in the partonic initial state resulting in different final states:

1) inclusive neutral and charged pions
   $a_{LL}(gg, gq \rightarrow \pi^{0,\pm} + X)$
2) inclusive photon production (direct or prompt photon production)
   $a_{LL}(gg, gq \rightarrow \gamma + X)$
3) charm & anti-charm and beauty-anti-beauty pair production
   $a_{LL}(gg, gq \rightarrow \bar{c}c, \bar{b}b + X)$
4) direct photon production along with jet
   $a_{LL}(gg, gq \rightarrow \gamma + jet + X)$

For different final states, experimentally we measure the following double spin asymmetry (a counting rate asymmetry):

$$A_{LL} = \frac{1}{P_B P_Y} * \frac{N_{++} - R * N_{+-}}{N_{++} + R * N_{+-}} \qquad (2)$$

Where $P_{B/Y}$ are the blue and yellow beam polarizations, $N_{++/+-}$ the counting rates measured with the ++(parallel) and +-(anti-parallel) orientations of the proton beam spin vectors and R is the ratio of luminosities for ++ and +- spin orientation collisions. (Ideally, R=1).

The role of VTX Detector:

The different channels with which PHENIX can make measurements of the gluon polarization cover different kinematical regions in x and Q^2. Figure 12 shows the x coverage possible with RHIC $p+p$ running at 200 GeV center of mass, ~70% beam polarization and ~300 pb^{-1} luminosity (delivered) with the PHENIX detector for the above mentioned physical processes under two different scenarios. Here x is the gluon momentum fraction of the proton momentum, and "coverage" implies we measure the ratio $\Delta G/G$ with ~20% relative uncertainty of its expected value at that x. The baseline PHENIX detector is capable of covering a range: $0.02 < x < 0.3$ (shown in blue). We note that although the coverage extends over one decade in x, between the different channels there is little overlap. The coverage extended by the VTX detector is shown in the same figure (in red).

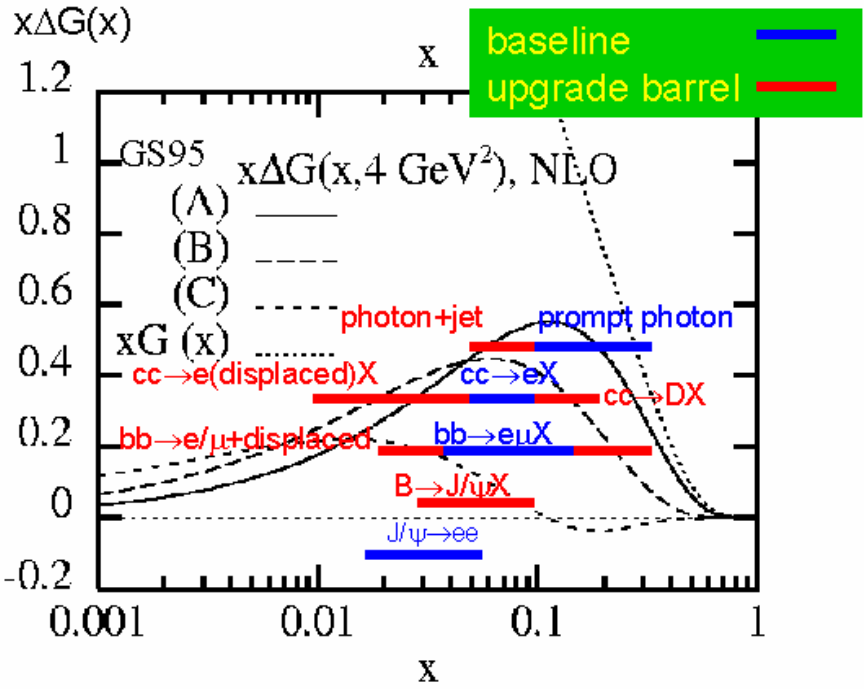

Figure 12 Expected x-ranges for polarized and un-polarized gluon distribution measurements in PHENIX using different channels. The blue bars indicate the PHENIX detector's existing capability while the red bars indicate the enhanced coverage provided by the proposed silicon vertex detector upgrade to PHENIX.

The proposed silicon vertex detector will be crucial in the determination of gluon distribution in two significant ways:

1) Different measurements will cover the same kinematic regions: this would enable the much-needed cross-checks within PHENIX for accessing the polarized gluon distribution. The vertex detector extends the reach in x for many of the measurements and hence adds a significant amount of overlap in x-range coverage.
2) By being able to observe displaced vertices at low-pt for semi-leptonic decays of charm and beauty, the VTX detector enables a larger x-range over which we will make gluon polarization measurements. It is estimated that the x reach of the silicon-vertex upgraded PHENIX will be $0.01 < x < 0.3$.

Since the two measurements of open charm and beauty and of γ+jet crucially depend on the silicon vertex detector more details are provided on these two channels below.

<u>The heavy quark physics (open charm and beauty production)</u>

By requiring an additional cut on displaced vertex information coming from the vertex detector, we gain significantly in the robustness of the heavy-quark results by improving the purity of the event sample.

We plan to observe charm production through its semi-leptonic decay to $e^{\pm}$. We will need a good vertex resolution to identify the displaced vertices in such events. The main backgrounds expected for this physics include Dalitz decays and photon conversions. This has been studied (Section 3.2) using a GEANT detector simulation. We estimate that the SVTX could achieve ~50 μm DCA resoluiton. Using a DCA cut value ~200 μm for tracks with $p_T > 1$ GeV/c, we should be able to achieve a significant background reduction. As a result of the DCA cut the purity of the event sample increases from ~50% to ~90% (see Figure 24 in section 3.2).

Another possible channel to access gluon distributions is open beauty production. Beauty production measured at the Tevatron at 1.8 TeV, and the next-to-leading order pQCD calculation missed the data by factor of 2 or greater. The discrepancy between the experimental data and the theory has sparked much debate and excitement recently. New data on beauty production would be crucial, especially at RHIC, since they would be obtained at different values of $\sqrt{s}$ (200 and 500 GeV).

Measurements of beauty production can be performed in the present PHENIX detector using electron-muon coincidence using the central and forward muon arms. With the limited acceptance for the detector subsystems, this results in a

narrow kinematics coverage and small detection cross section. With the VTX detector, we have two additional channels to measure beauty production at RHIC: the single electron in the central arm and $B \rightarrow J/\psi + X$. The single electron channel provides us much higher statistics compared with the μ-e channel.

The main background in the b physics measurements is expected from the charm semi-leptonic decay, Dalitz decays, and photon conversions. Information provided by the VTX detector will enable a cut on the DCA to produce a highly pure sample of events involving beauty quarks with less than ~10% impurity from charm quark events in the low p_T range (< 3 GeV) and even purer b-sample at higher p_T. Without the VTX this impurity is expected to be more than 75% (see Figure 31, section 3.2). The VTX and the DCA analysis of data it will thus produce a reliable data set highly devoid of charm events and other impurities for the comparison with theory for beauty production cross section.

The displaced vertex resolution possible with the VTX detector enables additionally one more measurement: $B \rightarrow J/\psi + X$. B mesons could be identified with J/ψ decays detected as displaced electron-pair vertices. This process identifies open beauty production with no charm contribution and will be a clean probe of the polarized and the un-polarized gluon distributions.

Finally, a recent theoretical study (I. Bojak, Ph.D. Thesis, April 2000, Univ. Dartmund) of the expected values of the open charm and open beauty asymmetries at high energy concluded that they would be of the order of a few times 10^{-3} at RHIC energies. The open beauty asymmetries are expected to be slightly larger (private discussions with W. Vogelsang). False asymmetries related to bunch-to-bunch variation of luminosity in a collider are potentially a show-stopper for any spin measurement if they are comparable in magnitude to the asymmetry one is interested in. However, from the RUN 3 data analysis we already know at RHIC these false asymmetries can be controlled to be smaller than a few times 10^{-4}. Although this situation could potentially get worse with the RHIC luminosity increase (due to difficulties associated with handling higher beam currents), additional tools are being discussed at RHIC that are expected to reduce uncertainties due to such effects by a factor of ~10 using techniques such as simultaneous spin flips in both RHIC beams using a spin flipper magnet and beam re-cogging. With such anticipated developments we will be able to pursue the open charm and open beauty *spin physics* measurements at PHENIX with the proposed Silicon Vertex detector.

Direct photon + Jet measurement:

One of the limitations of the direct photon measurement that is possible with existing PHENIX detector, is an imperfect determination of the partonic kinematics in the event. The uncertainty in the determination of the x of the gluon exists because we observe only a single photon in the final state. Event-by-event reconstruction of the event kinematics is impossible, and one has to rely on the Monte Carlo simulations to understand the event kinematics coupled to the detector acceptance. This has been studied (see section 3.3) using a PYTHIA simulation. The proposed VTX detector enables the tagging of the hadronic activity (originating from a single quark/jet), hence determination of the jet axis (Figure 33), and will significantly reduce the uncertainties stemming from the reconstruction of the parton kinematics (Figure 34). Our dependence on Monte Carlos is factored out. Additional uncertainties related to the determination the total jet energy, remain, however one does better by tagging the jet with the proposed VTX.

PHENIX's limited acceptance in rapidity as well as azimuth has been a significant hurdle in our measurement of any jet related physics. The VTX detector with its good hit resolution and large acceptance will serve as a high-resolution tracker and provide the much needed jet axis measurement in co-incidence with the direct photon measurement. Monte Carlo studies indicate a significantly improved determination of x-gluon (20% relative compared to ~40% without the VTX). The VTX detector can also be used to detect charged tracks around the direct photon candidate. This may allow an improved isolation selection for the direct photon in the event.

The VTX detector is hence crucial in determining the polarized gluon distribution using the direct photon channel. For this particular measurement it converts the PHENIX detector in to a high resolution - large acceptance detector.

Other advantages of the VTX Detector:

There are other advantages of the silicon vertex detector, which we mention briefly in this section.

Background suppression for W physics event sample

W physics at PHENIX allows a unique possibility to distinguish the flavor (u and d) dependence of quark structure function and its polarization: W^+ is produced by collision of $u + \bar{d}$, while W^- is produced by $d + \bar{u}$. However, if one wants to explore W physics with electron final states in the central arm,

backgrounds from hadrons can be a significant problem. Improved momentum resolution and (hence) background suppression is the way to reduce the background. Using information from the silicon vertex detector in the momentum reconstruction, the moment resolution is improved by a factor 2 or 3. In addition, the large solid angle coverage of VTX will allow us to apply an isolation cuts for the single electron candidate and thereby to improve S/B ratio of the W decay electron. In general, an electron from W decay is isolated from a jet activity, while the backgrounds (very high p_T charged particle decays and high p_T electrons from heavy quark decay) have associated jet activity around it.

Improved correlation measurements between particles

It is expected that the large acceptance of the silicon vertex detector in rapidity and azimuthal coverage, will enable us understand correlations between particles produced in the hadron-hadron collisions. One important measurement is related to the transversity distribution: transversity structure function is as fundamental as any other (un-polarized and polarized structure function of the nucleon), but it is yet to be measured. It is a helicity odd object, and it needs to be measured in experiments as a product of another helicity odd object so that the product is helicity even. Measurements of this kind involve measuring many particles and their angular correlations in the final state in addition to possible hadronic jet activity in the primary interaction. One example of this is the Collins fragmentation function, which refers to a correlation between hadron distributions around the jet axis. The orientation of $\pi^+ \pi^-$ (hadron-) pair is also expected to show correlation with the transverse fragmentation function in single transverse spin $p+p$ scattering at RHIC. The Silicon vertex detector is expected to improve determination of this orientation in spite of the fact that lack of particle-ID associated with such an event will dilute the correlation. Through these correlation functions we plan to measure the transversity distribution. Needless to say, enhanced acceptance, resolution provided by the silicon vertex detector would be crucial for such a measurement.

2.3 Exploration of the nucleon structure in nuclei

Proton-nucleus collisions not only provide important baseline information for the study of QCD at high temperatures, they also address the fundamental issues of the parton structure of nuclei. Since the discovery of the EMC effect in the 1980's, it is clear that the parton-level processes and structure of a nucleon are modified when embedded in nuclear matter[37]. These modifications reflect fundamental issues in the QCD description of the parton distributions, their modifications by the crowded nuclear environment of nucleons, gluons and

quarks, and the effect of these constituents of the nucleus on the propagation and reactions of energetic partons that pass through them.

Of particular interest is the depletion of low momentum partons (gluons or quarks), called shadowing, which results from the large density of very low momentum partons. For gluons at very low momentum fraction, $x < 10^{-2}$, one can associate with them, following the uncertainty principle, a large distance scale. These high-density gluons then will interact strongly with many of their neighbors and by gluon recombination or fusion are thought to promote themselves to larger momentum fraction, thus depleting small values of x. In most pictures the overall momentum is conserved in this process and so the small x region gluon density is depleted while the moderate x region above that is enhanced. In recent years a specific model for these processes, called gluon saturation, has been discussed extensively by McLerran and collaborators[38]. Gluon saturation affects both the asymptotic behavior of the nucleon gluon distributions as x approaches zero and the modification of this behavior in nuclei, i.e. shadowing.

At RHIC energies many of the observables are affected by parton distributions at small x where nuclear shadowing is thought to be quite strong. However, theoretical predictions of the amount of shadowing differ by factors as large as three. For example, in the production of J/ψ in the large rapidity region covered by the PHENIX muon arms, models from Eskola et al (Figure 13) predict only a 30% reduction due to gluon shadowing, while those of Frankfurt & Strikman[39] (Figure 14) or Kopeliovich[40] predict up to a factor of three reduction. Results from the measurements of the d+Au run should help to clarify how much shadowing we have, but increased statistics from higher luminosity runs and more definitive measurements via observables that are sensitive to gluon structure functions over several channels will be necessary to test the theory with sufficient power to constrain the underlying QCD processes.

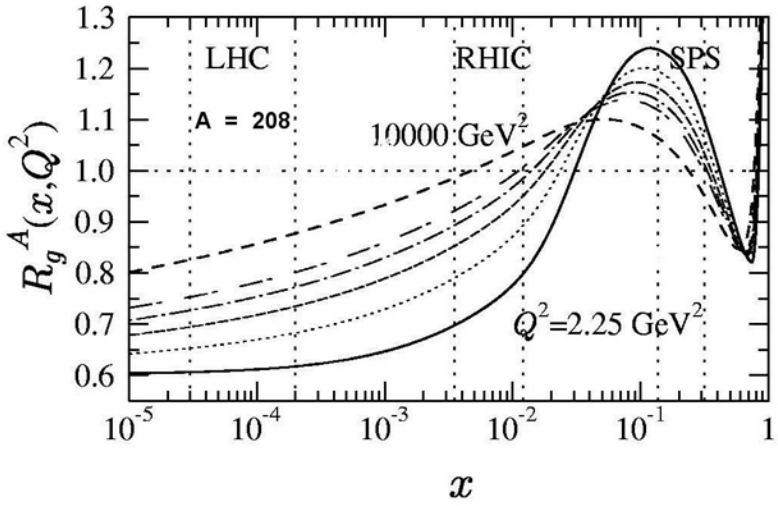

Figure 13 Gluon shadowing from Eskola[41] as a function of x for different Q^2 values: 2.25 GeV² (solid), 5.39 GeV² (dotted), 14.7 GeV² (dashed), 39.9 GeV² (dotted-dashed), 108 GeV² (double-dashed) and 10000 GeV² (dashed). The regions between the vertical dashed lines show the dominant values of x_2 probed by muon pair production from $D\bar{D}$ at SPS, RHIC and LHC energies.

In particular, it is clear that a precise knowledge of the shadowed gluon structure functions in nuclei is essential towards understanding several of the important signatures for QGP in heavy-ion collisions at RHIC, including open and closed heavy-quark production. Recombination models for J/ψ production, which might cause an enhancement of that production in heavy-ion collisions due to the large density of charm quarks created in a collision, must be constrained by an accurate measurement of the amount of charm produced given the shadowing of the gluon densities in the colliding nuclei.

A number of other physics issues besides shadowing also need to be understood. Energy loss of partons in the initial state is thought to have a small effect at RHIC since the energy loss per fm, in most models, is thought to be approximately constant and small compared to the initial-state parton energies at RHIC. On the other hand, partons in the final state could show some effects of energy loss since their momentum is lower, while heavy-quarks are expected to lose less energy than light partons due to the dead-cone effect[42]. These issues are very important in the high-density regions created in heavy-ion collisions, but need a baseline for normal nuclear densities from proton-nucleus collisions. Another general feature of most produced particles comes from the multiple scattering of initial-state partons, which causes a broadening of the transverse momentum (Cronin effect) of the produced particles.

In general, all processes suitable for the measurement of gluon spin structure in nucleons are also ideal for probing the gluon distributions in nuclei. The reach in Bjorken x is indicated in Figure 14, superimposed on calculations of the ratio of nuclear to nucleon gluon structure functions.

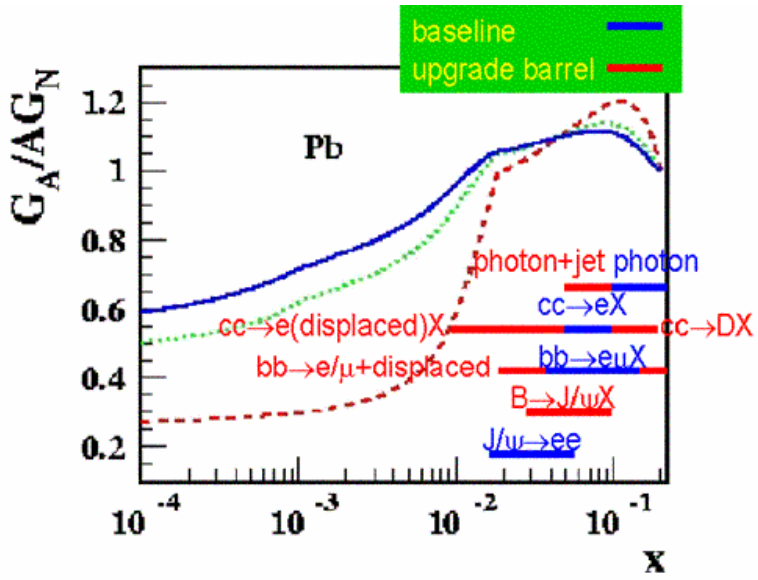

Figure 14 Gluon shadowing predictions along with PHENIX coverage. The red bars indicate the additional range provided by the vertex upgrade, while the blue bars cover the PHENIX baseline. The three theoretical predictions are for different Q transferred, blue, green and red lines are Q = 10, 5 and 2 GeV/c respectively, from Frankfurt and Strikman[43].

The red bars indicate the additional coverage provided by the vertex upgrade compared to the baseline of PHENIX. The vertex upgrade extends the x-range from the anti-shadowing region into the shadowing domain and therefore will provide a measurement of shadowing and establish the shape of the shadowed structure functions versus x.

Drell-Yan measurements, which provide a direct measure of the anti-quark distributions in nucleons or nuclei, have always been limited in the past in their reach to low x by the inability to separate the Drell-Yan muon pairs below the J/ψ in mass from copious pairs from open-charm decays in that mass region. For example, in FNAL E866/NuSea, information extracted from the Drell-Yan process was limited to masses above 4 GeV.

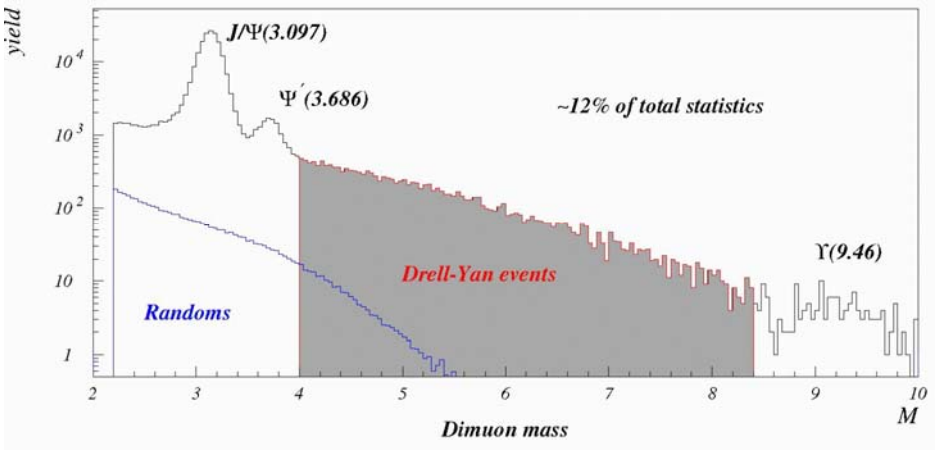

Figure 15 Dimuon mass spectrum from E866/NuSea[44] showing the mass region used in their analysis which excludes masses below 4 GeV. Lower masses were excluded because of the large backgrounds from open charm in that region.

On the other hand, PHENIX, with the addition of a vertex detector, should be able to identify and quantify the portion of the lower mass dimuon continuum from charm decays and therefore isolate the Drell-Yan process at these lower mass and lower x values. In the central-rapidity barrel region values as low as $x_2 \sim 0.7\times10^{-2}$ could be accessed. This will still be a challenge because of the small cross sections and yields for Drell-Yan at RHIC, but has the potential of providing information on the anti-quark distributions at much smaller values of x. At the same time one would also learn more about charm production and the correlation of the charm pairs through the charm pairs found in the continuum.

In summary, the silicon vertex barrel, which covers the PHENIX central arm mid-rapidity range ($|y| < 0.35$), addresses the following physics in dA reactions：

- Charm and beauty at high p_T and mid-rapidity via high-p_T electrons and also exclusive decays such as $D \to K\pi$ and $D \to K\pi\pi$.
- A gluon structure measurement in the anti-shadowing region as a baseline for shadowing measurements at small x.
- Charm measurements at mid-rapidity as a baseline for J/ψ production, i.e. for comparisons of open and closed charm which should share the same initial-state effects in nuclei.
- Accurate measurement of nuclear dependence of charm cross section
- Beauty cross sections at mid-rapidity as a constraint on the contributions of $B \to J/\psi$ to J/ψ production.
- Comparison of light and heavy-quark p_T distribution to determine differences in energy loss and Cronin effects.

- Better separation in high-luminosity measurements of Υ measurements of the three Υ states.
- Low-mass electron pairs and anti-quark shadowing at small x values.

3. Physics measurements with the VTX detector

The proposed VTX detector provides us the tool to measure new physics observables that are to date not accessible at RHIC or available only with very limited accuracy. These include a precise determination of the charm production cross section and transverse momentum spectra - particularly at high p_T, a measurement of beauty, and the detection of recoil jets in direct photon production. In this section, we discuss how the proposed VTX detector makes these measurements possible, or significantly improves our capability to address these observables.

Before discussing the simulation results and the expected performance of the VTX for each of the observables, we briefly explain the design of the proposed VTX detector and discuss the required performance. More technical details of the implementation of the VTX detector are presented in the section 4. In the last sub-section, we summarize the expected rate of physics signals and the physics reach that will become available with the VTX detector.

3.1 Design Considerations and the VTX detector geometry

Design Considerations

The design considerations for the detector are

- ability to match tracks reconstructed in the central arms to hits or track segments from the silicon vertex detector.
- sufficient position accuracy so that the displacement resolution of the track with respect to the collision point is less than the $c\tau$ of charm and beauty decays, i.e. a resolution less than 100μm, preferably at the level of 30-50 μm.
- high resolution predominantly in $r\phi$ direction, i.e. the main bend plane of the magnetic field, matched to the central arm resolution.

A variety of simulations and first principle calculations have shown that the displacement resolution is dominated by the position accuracy of the two inner most detector layers and by the amount of multiple-scattering between the collision point and the two position measurements. Assuming that the multiple scattering occurs at the location of the first layer, the Distance to the Closest Approach (DCA) of a trajectory to the beam axis in the main bend plane can be measured with a resolution given approximated by:

$$\sigma^2{}_{DCA} \approx \frac{\left(\sigma_1{}^2 r_2^2 + \sigma_2^2 r_1^2\right)}{(r_2 - r_1)^2} + \theta_{ms}{}^2 \frac{r_1^2}{\sin^2\theta}$$

Here σ_1, σ_2 and r_1, r_2 are the $r\phi$ resolution and radial position of the first and second layer, respectively. The average multiple-scattering angle, denoted by θ_{ms}, is given by the beam pipe thickness and the first detector layer. The first term quantifies the contribution due to the finite position resolutions, while the second term is the effect of the multiple scattering. Given standard silicon detector segmentation of 50 to 100 μm in $r\phi$ and a typical thickness of 1 to 2 % of a radiation length, both terms contribute to the final resolution. For our "strawman" layout of the VTX, which is discussed below, typical DCA resolution from this estimate is ~ 40 μm: a value confirmed by detailed simulations.

It is evident from the equation for the DCA resolution that in order to minimize the DCA resolution, the first layer should be as close to the collision point as is practical, which at RHIC is about 2 cm, and the first layer plus beam-pipe should be as thin as possible.

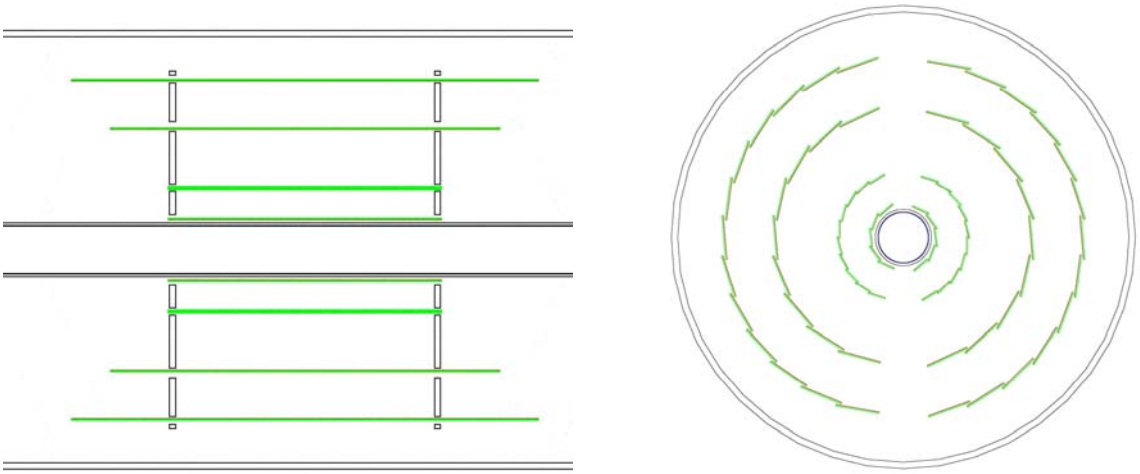

Figure 16 (left) Cross section of the silicon vertex tracker (VTX) along the beam axis. The inner pixel hybrid layers are located at a radial distance of 2.5 cm and 5 cm from the beam, and they extend over ~22cm in beam direction. The silicon strip outer layers are located at 10 and 14 cm. The length of the 3rd and 4th layer is ~32cm and ~38cm, respectively, in beam direction. The Be beam pipe with 2 cm radius is also shown. (right) Cut through the silicon vertex detector in the xy-plane transverse to the beam axis. The VTX is assembled in two half shells with small acceptance gaps at top and bottom. Each half shell has 5 and 10 pixel ladders and 9 and 13 strip ladders.

VTX detector geometry

After exploring different configurations, we decided to perform all feasibility studies with the detector layout depicted in Figure 16. The layout features four concentric barrels of silicon detectors with a length of approximately 38 cm along the beam axis. The outer two barrel layers are silicon strip detectors placed at radial positions of r_4=14 cm (barrel 4), r_3=10 cm (barrel 3). The inner barrel is composed of two layers of silicon pixel device that are located at r_2=5.0 cm (barrel 2) at r_1=2.5 cm (barrel 1). The beam-pipe has a design radius of 2.0 cm and is made of 500 μm thick Be.

The pixel detectors for the inner barrel layer have a segmentation of 50 μm by 425 μm. The outer layers are assumed to have 80 μm × 3 cm strips. This choice together with the radial location guarantees that the occupancy of the innermost strip layer (barrel 3) remains about 4.5% even in central Au-Au collisions. In the low occupancy environment of *p+p* collisions a stereoscopic readout of the strip layers reduces the effective channel size to 80μm × 1000μm.

These detectors have been implemented as our "strawman design" into the GEANT simulation of the PHENIX detector. At this point no details of cooling, mechanical support, cables etc. are put into the simulation, however these materials are approximated by an effective thickness of the detector layers. From a survey of existing silicon detectors we conclude that a thickness of 2% of a radiation length per layer should be achievable while 1% of a radiation length will be challenging. We have chosen these two values for this effective thickness, 1% and 2% of a radiation length, to bracket the potential range of thickness and performed simulations with both values.

Detector Occupancy

The occupancy of the each layer is calculated by using a GEANT model of the VTX detector integrated into the standard PHENIX simulation program, PISA. We use HIJING event generator to generate central Au+Au collision event, and feed the generated events into PISA with the VTX detector. In the simulation, we use a simplified model of the VTX signal generation. Charge sharing among the pixels and strips is accounted by the length of track segment projection onto the pixel or strip area. In this simplified simulation, no effect from charge diffusion in the sensor is taken into account. Since the size of charge diffusion (~ 10 μm) is much smaller than the strip width (80 μm), the dominant part of charge sharing effect is included in the simulation.

Table 1 Occupancy of the VTX layers for central Au+Au collisions at 200 GeV. HIJING event generator and a GEANT model of the VTX detector is used to calculate the occupancy.

Layer	radius	Detector	Occupancy	
Layer 1	2.5 cm	Pixel	0.53 %	
Layer 2	5.0 cm	Pixel	0.16%	
Layer 3	10.0 cm	Strip	4.5 % (x-strip)	4.7 % (u-strip)
Layer 4	14.0 cm	Strip	2.5 % (x-strip)	2.7 % (u-strip)

The result of the simulation is summarized in Table 1. The occupancy is lowest at about 0.16 % for the second pixel layers. The third layer, or the first strip layer, has the highest occupancy of about 4.5%. The calculated occupancy is about twice the value if there were no charge sharing effect.

The physics observables discussed in this proposal use hits from the VTX in two ways.

1. Tracks from the central-arm are projected to the VTX layers, and the hits in the VTX are associated with the track. The accurate VTX hit information is then used to refit the track and a DCA is calculated to the collision vertex.
2. In standalone tracking, hits from the four VTX layers are collected and used to form track segments.

The tools to associate hits with tracks and refit are reasonably well-developed and they are described below, while the stand-alone tracking is in early stages of development.

3.2 Central Track – VTX matching

Central Track – VTX matching criteria

In order to make full use of the VTX capabilities, tracks reconstructed in the central arms have to be matched to hits or track segments in the VTX. We use the known magnetic field to project central arm tracks to each of the layers in the VTX. Figure 17 shows the residual between the track projection of 2 GeV/c pions and the hit location in ϕ and z for the inner-most pixel layer. The hit positions in the VTX detector have not been used at this stage of the track and hit matching. The distributions are centered at zero and have a width of 5 mrad and 0.05 cm. Similar residual distributions are found for each of the four VTX layers.

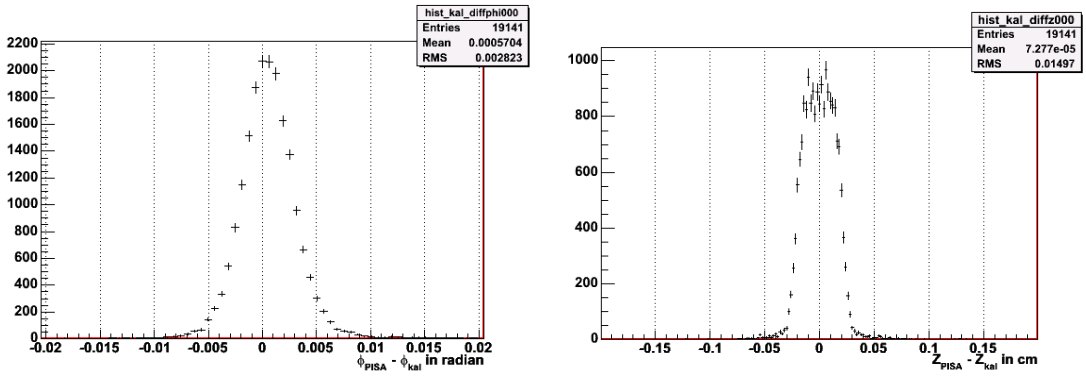

Figure 17 The residual between track projection and hit location in ϕ and z for the inner-most pixel layer. This simulation is for 2 GeV/c pions.

For tracks from $D \rightarrow K\pi$ decays the residual distribution is expected to be broader, since the central arm tracking assumes the track originated at the collision vertex. This is verified in Figure 18, which shows the residuals for tracks from $D \rightarrow K\pi$ decays, again the inner-most layer of the VTX. The residuals are significantly larger than for primary tracks. It is important to choose the matching criteria for hits to central arm tracks to be broad enough to include also the tracks from open charm and beauty decays.

For each VTX layer the hit-association assigns to each central arm track the hit closest to the track projection within a certain window. Currently the size of the window is taken to be 30 mrad in ϕ and 0.15 cm in z for the pixel layers, i.e. several times the widths of the residuals found in the $D \rightarrow K\pi$ decay shown in Figure 18. The window size is changed to 30 mrad in ϕ and 0.45 cm in z for the strip layers. A future improvement of the algorithm will be based on momentum dependent matching window.

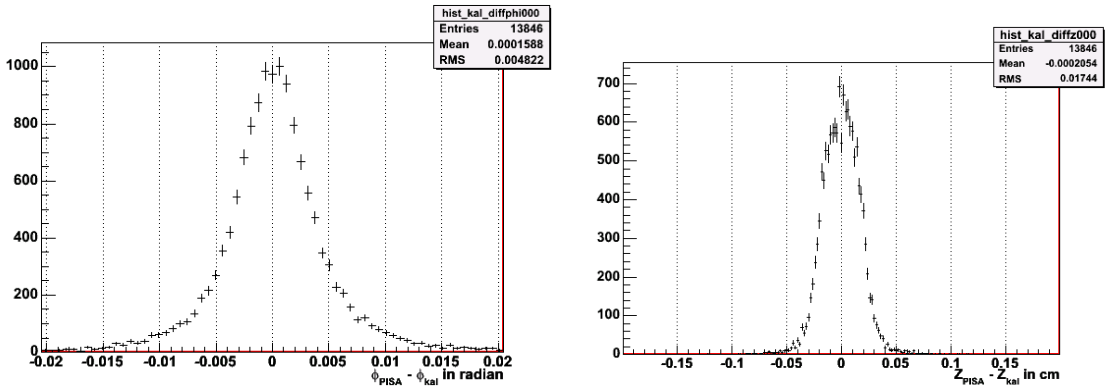

Figure 18 The residual between track projection and hit location in ϕ and z for the inner-most pixel layer. The VTX hits are not included in the fit. This simulation is for $D \rightarrow K\pi$ at p_T = 2 GeV/c.

The number of random charged particles inside of the initial matching window is about 0.1 for the most central Au+Au collisions. The matching window size can be further reduced after the track fitting using the hits in the VTX, eliminating most accidental matches. The residual distribution between the track fit and the VTX hit position in the inner-most pixel layer is shown in Figure 19 for prompt pion and in Figure 20 for particle from $D \rightarrow K\pi$ decay. The RMS width in ϕ and z are reduced to 1.6 mrad and 126 μm for prompt pion at 2 GeV/c. For tracks from $D \rightarrow K\pi$ decays, which have lower momentum in average, the RMS width of the residual is 2.2 mrad and 150 μm. The solid angle of the 3 σ matching window is then reduced to about 0.1 mstr and the occupancy in the window is about 1% for the most central collision.

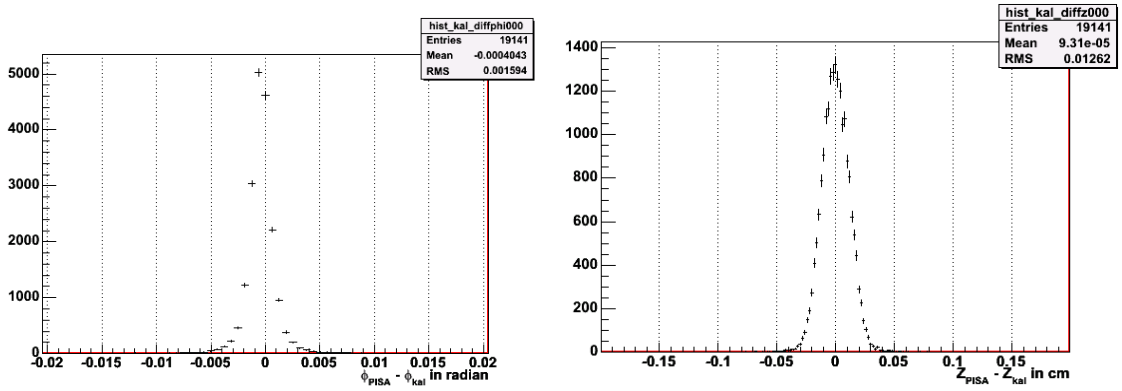

Figure 19 The residual between the track and the hit location in ϕ and z for the inner-most pixel layer after the hits in the VTX are included. This simulation is for 2 GeV/c pion.

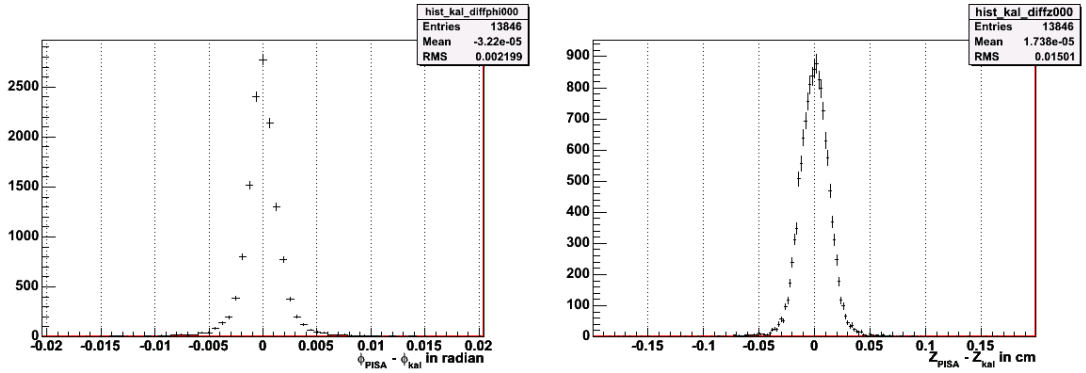

Figure 20 The residual between the track and the hit location in ϕ and z for the inner-most pixel layer after the hits in the VTX are included. This simulation is for $D \rightarrow K\pi$ at $p_T = 2$ GeV/c.

DCA measurement by the inner two layers

After the hits in the VTX detector are associated with the track, the distance of closest approach of the track to the primary event vertex (DCA) is calculated in the plane transverse to the beam. We base this calculation on the inner-most two pixel layers. Figure 21 shows the DCA distribution for pions at p_T = 2 GeV/c. A DCA resolution of 36 μm is achieved, which is consistent with the 50 μm pixel width of the detector.

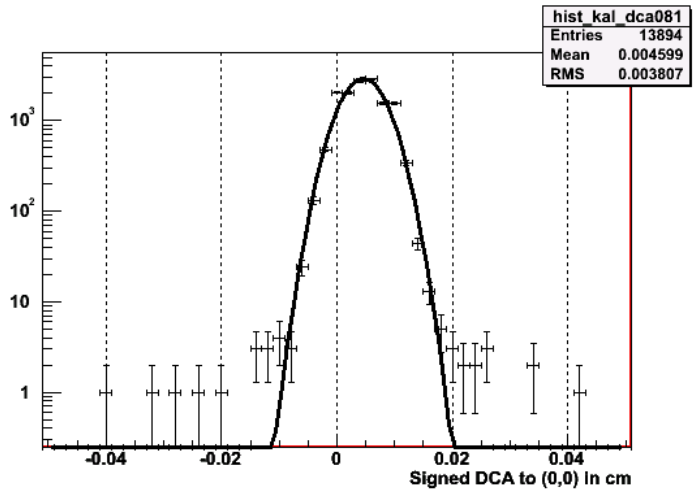

Figure 21 The DCA distribution for 2 GeV/c pions in the PISA simulation of the VTX detector. The DCA resolution of σ=36 μm was achieved using the two inner-most two pixel layers.

We have also evaluated the effect of the hit occupancy expected in central Au+Au collisions on the matching resolution. The statistics of this simulation is limited, but the result shows that the resolution only slightly deteriorates. For example, for the inner most pixel layer, the RMS of the residual in ϕ increases from 2.2 mrad to 2.5 mrad, and the RMS of the residual in z increase from 150 μm to 230 μm.

Central Au+Au simulation --- Kalman fitting

A track fitting code using a Kalman filter technique has been developed for the VTX detector by Iowa State University group. In this code, a track reconstructed from the PHENIX central arms is projected on the VTX detector and is associated with the hits on the silicon detector layers. Then the distance of the closest approach (DCA) of the track to the primary collision vertex is calculated. The new code performed a global fit of the hits

in VTX tracker and the track reconstructed in the PHENIX central arms. The effect of the multiple scattering is taken into account in the global fit.

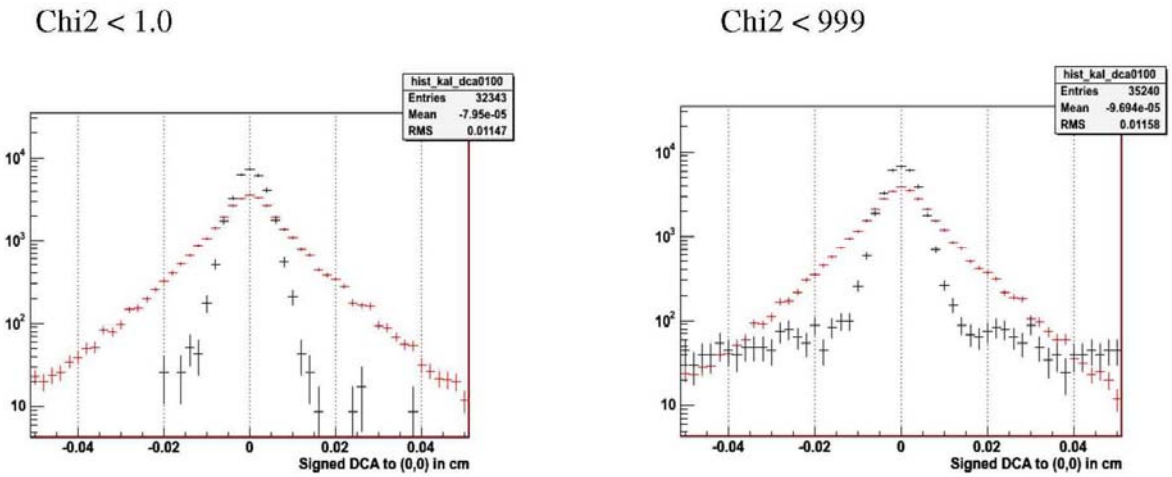

Figure 22 DCA distribuion of tracks from D^0 decays (red) and that from primary vertex (black) from simulation. In the right panel, a very loose chi-squares cut is applied, while a tight chi-squared cut is applied in the left.

The code is evaluated using the simulated events from a GEANT simulation of VTX detector in PHENIX. The simulated tracks are reconstructed by the standard PHENIX reconstruction program, and then they are connected with the VTX detector using the Kalman fit program. Results from the simulation are shown in Figure 22. In both panels of the figure, the black histograms show the DCA distribution of the tracks from the primary vertex in simulated central Au+Au collision events, and the red histograms show that of charged tracks from simulated $D^0 \rightarrow K\pi$ decays. In the right panel, very loose chi-squares cut ($\chi^2 < 999$) is applied, and the DCA distribution of the primary tracks has a very long tail caused by high multiplicity of the event. This long tail would prevent clear separation of charm decay tracks from background tracks. In the left panel, the tail is cleaned up by a tight chi-squares cut, and the primary vertex has a Gaussian DCA distribution. The simulation demonstrates that VTX detector can clearly separate charm decay tracks and background tracks.

3.3 Open Charm and Beauty Measurement

<u>Open Charm measurement from semi-leptonic decay</u>

Open charm and beauty spectra and yields are a sensitive probe of the early stages of heavy-ion collisions, and are keys for the physics goals of gluon spin

structure and for structure function studies in pA reactions. For heavy-ion collisions, the goal is to improve the accuracy and precision of the charm measurement, and to extend the reach to higher p_T to measure the energy-loss of open charm. The yield of beauty in heavy-ion collisions should be dominated by the initial hard collisions and hence will serve as a critical benchmark for the first stage of reaction.

For open charm our strategy is to use semi-leptonic decays to electrons in a wide p_T range and to complement this at high p_T with hadronic decay channels. The four layers of the central silicon barrel provide an accurate measurement of the trajectory and impact parameter of tracks near mid-rapidity. Single electrons at different momenta were simulated and tracked through the GEANT implementation of PHENIX including the straw-man vertex detector. The simulation was run with 9kG magnetic field. The hits from the electrons were tracked back to calculate the transverse distance-of-closest approach (DCA) to the known point-of-origin. For all cases the DCA resolution is better than or comparable to the $c\tau$ of charm and beauty decays.

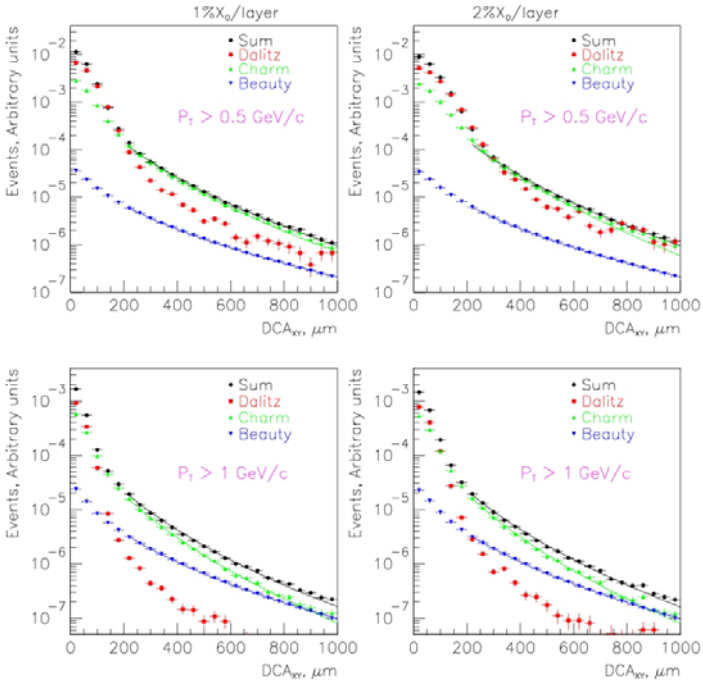

Figure 23 DCA distribution for electrons from Dalitz, charm and beauty decays simulated through four 1% Si layers on the left and four 2% layers on the right.

The power of this resolution is seen by comparing the distribution of DCA from charm, beauty and Dalitz decays of π^0 in Figure 23. The spectra were generated from p+p events (PYTHIA) passed through GEANT. The design thickness for the inner pixel layer is 1.2% of radiation length (X_0) and for the

outer barrel layers is 2.0 % X_0. For these simulations we bracket the range of possibilities by running simulations with either 1% or 2% X_0 per layer. In the bottom panels of Figure 23 are the DCA distributions for electrons above 1 GeV/c. A DCA cut of 200 μm removes the majority of Dalitz contribution from the electron yield. Note that this is the momentum of the electron and given the large *Q*-value of the *D* decay, these electrons predominantly come from low-momentum *D*'s. Since beauty decays have longer lifetimes, the electrons from *B* decays dominate at large DCA values. By fitting the full DCA distribution with the expected shapes from the different $c\tau$ we should be able to simultaneously extract integrated charm and beauty yields for electron momenta above 1 GeV/*c*.

Below 1 GeV/*c* the extraction is more difficult, but even down to 500 MeV/*c* charm dominates the DCA distribution above 200 μm for a thickness between 1 and 1.5 % of a radiation length. In particular, the vertex detector will provide a dramatic improvement over the previous measurement, which was limited to ~25 % systematic error resulting from the uncertainties in the background subtraction. Figure 24 shows the "signal to noise" for the optimistic (1 % X_0) and pessimistic (2 % X_0) cases compared to the measurement without the vertex detector available. This should allow a much cleaner extraction of the background-subtracted electron spectra for p_T>0.4 GeV/*c* than was previously available, including the charm-specific $d^2N_e/dydp_T$ for electrons up to about 2.5 GeV/*c*.

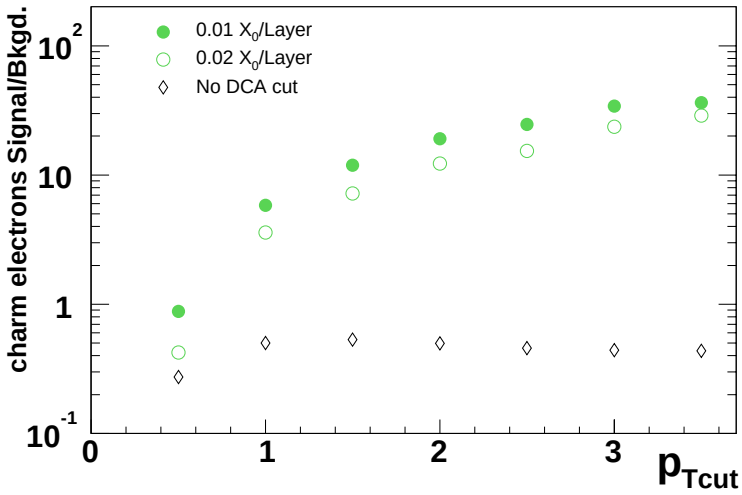

Figure 24 Signal to Background ratios as a function of minimum electron p_T cut. The signal corresponds to detached electrons from charm decays using a DCA cut of 200μm (circles) or no DCA cut (diamonds). The background corresponds to electrons from Dalitz decays and photon conversions which pass the corresponding DCA cuts, assuming four layers of Silicon with 1 or 2% of a radiation length per layer.

Figure 25 shows that there is a useful correlation between the p_T cut applied to the electrons and the p_T of the parent D meson. The points represent the most probable value of the parent p_T while the error bar represents the FWHM spread. Using the correlation, one can, for example, determine the p_T distribution of the parent D-meson from the decay electron spectrum.

.

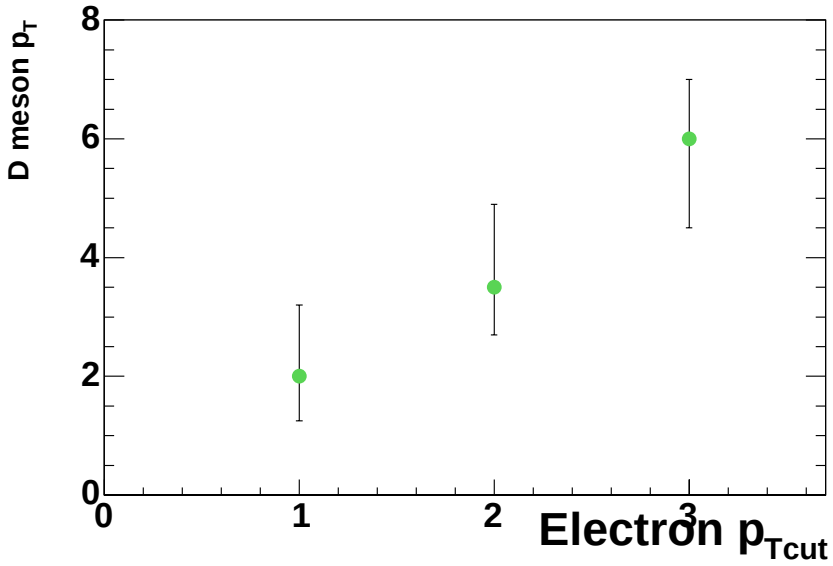

Figure 25 Correlation between the transverse momentum of the D mesons and the minimum p_T cut applied to the electrons (using a DCA cut of 120μm). The points represent the most probable value of the D meson p_T while the spread represents the (asymmetric) full width at half maximum.

Direct Measurement of $D^0 \rightarrow K^- \pi^+$ at high p_T

For higher values of the electron p_T, electrons from B decays dominate those from D decays and the extraction of the charm contribution becomes difficult. This can be overcome by a direct measurement via hadronic decay channels, which only becomes possible only at high p_T because of the small solid angle of the central arm spectrometers of PHENIX.

We have simulated D^0 production using $p+p$ PYTHIA events, and we tracked them through GEANT as described above. The decay pions and kaons where then compared to those directly produced in a central Au+Au background event. Figure 26 shows the DCA distribution for directly produced pions with a p_T cut of 1 GeV/c compared to the DCA distribution for pion daughter

particles from D^0 where the parent D^0 has p_T above 2 GeV/c. The pions from D^0 have a broader DCA distribution than directly produced pions. Clearly a DCA cut will remove a larger fraction of the direct pions than pions from D^0 decay.

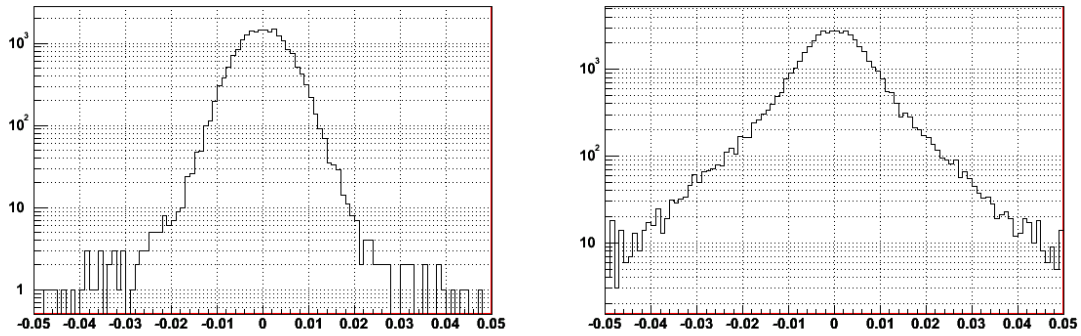

Figure 26 The DCA distributions in cm for pions with the inner pixel having 1%X_0 thickness. On the left is the DCA for direct pions with p_T >1 GeV/c and on the right is the DCA for pions from D^0 decay.

We have estimated the signal/background (*S/B*) for a D^0 analysis for central Au-Au collisions where the *S/B* is the smallest. In this study only D^0s with p_T above 2 GeV/c are were used to better match the opening angle of the daughters to the PHENIX acceptance. We require that both the pion and kaon from the decay fall into the acceptance and that they have not decayed before reaching the outer tracking detectors. We also assume that kaons are identified by one of the PHENIX PID detectors, an aerogel plus TOF detector covering the full acceptance of the west arm, and the existing TOF detector in the east arm. Lifting this requirement will deteriorate the signal/background by roughly a factor of 5, depending on the p_T of the kaon and the centrality of the event.

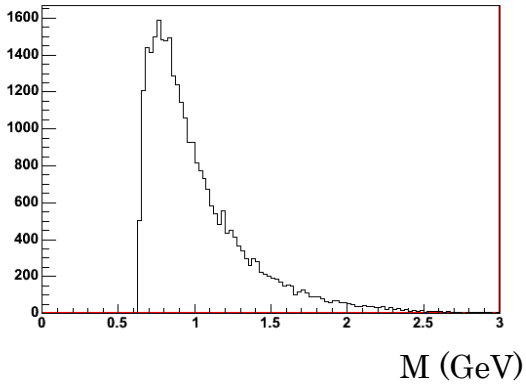

Figure 27 The invariant mass distribution for background pairs from central Au+Au events. Each pion+kaon pair has a pair p_T > 2 GeV/c.

Figure 27 shows the invariant mass for combinatorial background from pions kaons pairs that have a pair p_T > 2 GeV/c. Only a few percent of the combinatorial pairs have an invariant mass near the D^0 mass of 1.86 GeV. We count the background in a ±40 MeV window around 1.86 GeV. The window corresponds to ±2 times the rms mass resolution, which is 1% calculated from the known momentum resolution of the PHENIX tracking.

To count the signal we scale the number of reconstructed D^0's in the PYTHIA events by the number of binary collisions for a central Au+Au events. The signal/background (*S/B)* is then studied as a function of a simultaneous DCA cut on the pions and kaons. Figure 28 shows the *S/B* for different DCA cuts on pairs detected in the west-arm. The left- and right-hand panels are for simulations with 1% X_0 and 2% X_0 per layer. With no DCA cut the *S/B* is less than 0.1%, placing a DCA cut of 100 μm increases the *S/B* to a level of 2-3%. This *S/B* should be further improved by requiring that the parent particle point back to the collision vertex.

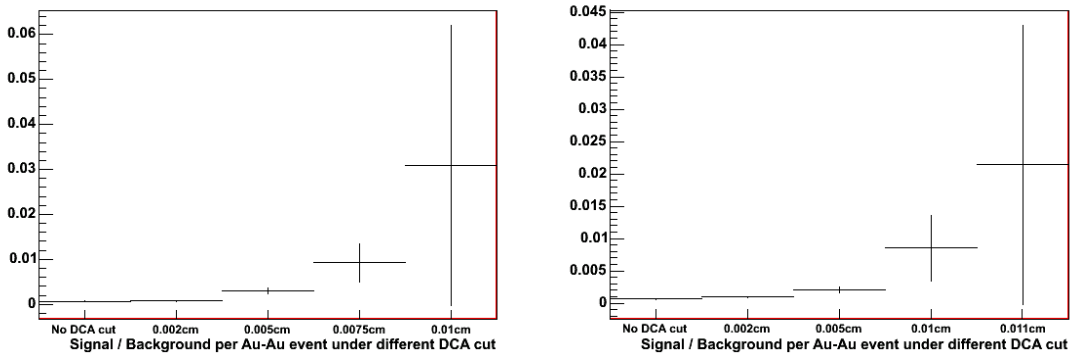

Figure 28 The *S/B* for $D^0 \rightarrow K\pi$ with a pt >2 GeV/c for central Au+Au events into the west-arm of PHENIX. On the left is the simulation for 1%X_0 thickness per layer. On the right is simulation for 2%X_0 thickness per layer.

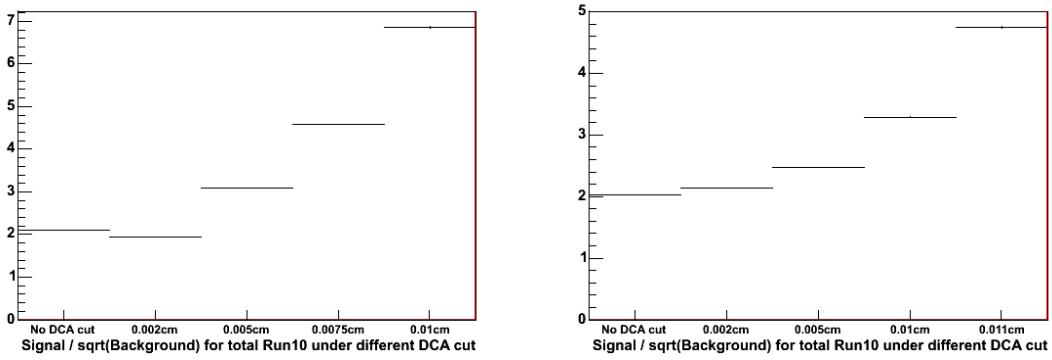

Figure 29 The S/√B for D^0+ $\bar{D}^0$->Kπ with a pt >2 GeV/c for central Au+Au events into the west-arm of PHENIX. On the left is the simulation for 1%X_0 thickness per layer. On the right is simulation for 2%X_0 thickness per layer.

The statistical significance of the signal can be estimated by $S/\sqrt{B}$. This ratio can be interpreted as the number of sigma of the extracted counts in the signal over the fluctuating background. It increases with the square root of the number of events. Using the run assumptions described in section 3.5, we will approximately collect 200M central Au+Au events within a ±10 cm collision window in a running period. Under these assumptions the combined (D^0+ $\bar{D}^0$) S/√B for different DCA cut strategies for pairs detected in the west-arm of PHENIX is shown in Figure 29.

From Figure 29, we can conclude that the D^0 peak for particles above p_T > 2 GeV/c can be extracted robustly. This is the worst case for the most central collisions where the combinatorial background is largest. Requiring the parent to point to the collision vertex can further reduce the background.

Simulations indicate that at higher-p_T the acceptance for D^0 increases since the opening angle between the daughters is smaller while the combinatorial background due to decreases. For D^0s above p_T > 3 GeV/c, even though the open charm yield is lower, the significance of the (D^0+ $\bar{D}^0$) peak maintains a level of 7 σ in central Au+Au collisions.

In the simulation in this section, we use PYTHIA to generate D mesons. Recent results in p+p and d+Au at RHIC indicate that PYTHIA underestimate the yield of high p_T D mesons more than a factor of 2. Therefore, the rate and the S/B estimate given this section should be considered as a lower limit.

Open Beauty Measurement

B meson production, while rarer than D production, is somewhat simpler to measure with the VTX detector because of the larger $c\tau$. The main challenge is the relatively low rate. We have at least two methods to measure B with the VTX detector:

- Semi-leptonic decays: Since beauty mesons have a larger lifetime than charm mesons, it is possible to extract the beauty yield at low transverse momentum from the distribution of decay distances. At large transverse momentum beauty decays dominate the DCA distribution.
- The decay channel $B \rightarrow$ J/ψ produces J/ψ that are displaced from the collision.

For momenta greater than 3 to 4 GeV/c electrons with displaced vertexes are dominated by beauty decays. This is clearly seen in Figure 30. By placing a DCA cut on the order of 150 μm we should be able to cleanly separate electrons from beauty from all other sources. Note however that this clean separation is only possible with the VTX detector even in this high p_T region. Although the high p_T region is dominated by beauty, there is a significant contribution from charm component, and the separation of these two components is possible only with the DCA measurement. With an accurate determination of the b component, the charm component will also accessible up to 6 GeV/c using a simultaneous fit of the DCA distribution. As discussed in the previous section, the high p_T charm component will also be measured directly in $D \rightarrow K\pi$ decay.

The signal to background ratio for beauty decays at high momentum is shown in Figure 31. The effect of the DCA cut is even more favorable than for charm.

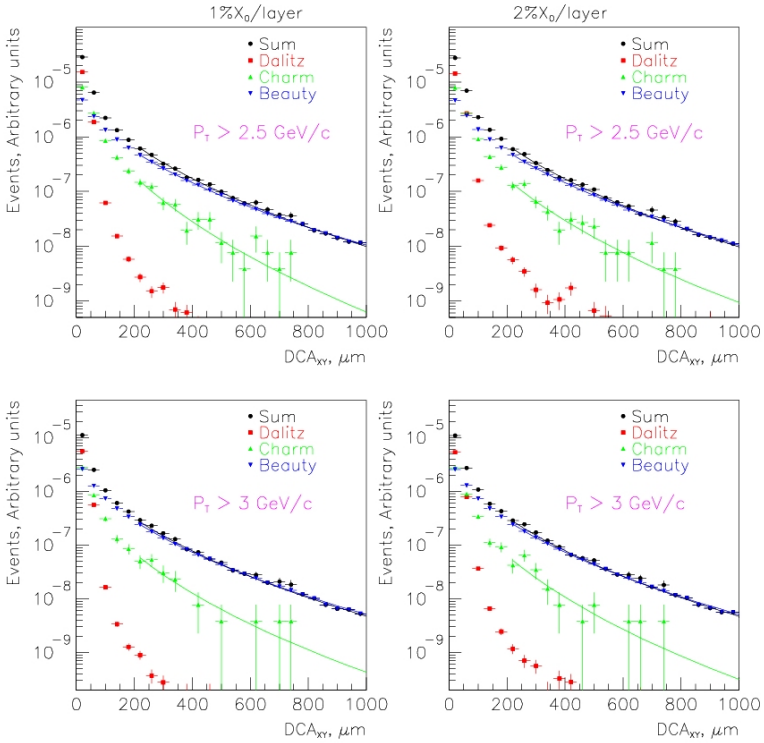

Figure 30 DCA distribution for electrons from Dalitz, charm and beauty decays simulated through four 1% or 2% Si layers

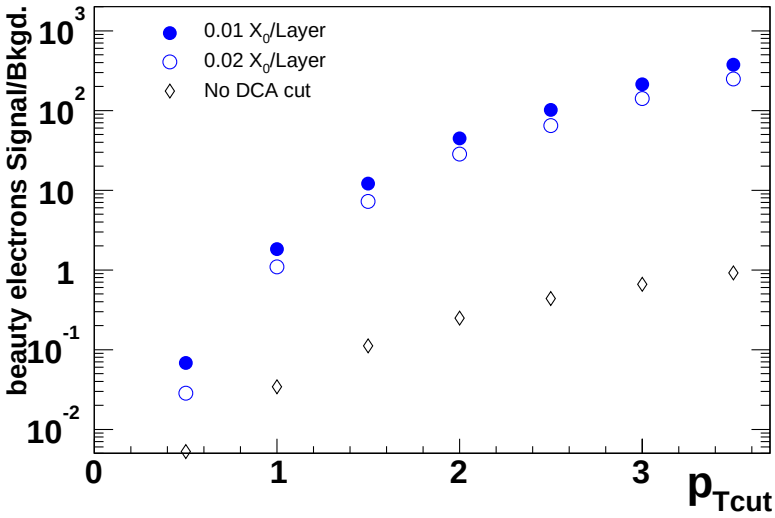

Figure 31 Signal to Background ratios as a function of the minimum electron p_T cut. The signal corresponds to detached electrons from beauty decays using a DCA cut of 200μm (circles) or no DCA cut (diamonds). The background corresponds to electrons from Dalitz decays and photon conversions which pass the corresponding DCA cuts, assuming four layers of Silicon with 1 or 2% of a radiation length per layer

3.4 Photon and jets measurement in polarized *p+p*

Direct photon emission is a key process to measure the gluon distribution in the nucleon and the polarization of the gluons. Because quark-gluon Compton scattering, $q+g \rightarrow q+\gamma$ is the dominant parton-level process of the production of high p_T direct photons in *p+p* collisions at RHIC energies, the cross section of this process is directly proportional to the quark and gluon densities multiplied by the pQCD cross section. Thus measuring the direct photon together with the recoil jet is a direct and a clean way to measure the gluon density and polarization as a function of the momentum fraction *x*. With the present PHENIX setup, direct photons are measured with the finely segmented electromagnetic calorimeters (EMCal) in the central arms. However, due to the limited coverage of the central arm tracker, most of the recoil jet cannot be detected or identified. Therefore we can only measure the inclusive direct photon averaged over the recoil jet kinematics. From data of other experiments, it has been found that there is discrepancy between experimental data of the inclusive direct photon spectra and pQCD calculations. Although the discrepancy can be explained by *e.g.* intrinsic k_T phenomenology, it is important to investigate the photon-jet correlation experimentally to understand it.

In *p+p*, *p+A*, and light ion collisions, the VTX detector works as a stand-alone, large solid angle charged particle tracker. The expected momentum resolution for tracks reconstructed solely by the VTX detector is about 10% for a 1 GeV/*c* track. This resolution is sufficient to reconstruct recoil jets in wide rapidity range ($|\eta|<1$). With the knowledge of the recoil jet we can constrain the initial kinematics (x_1 and x_2) of incoming partons and thus determine the gluon density and polarization as function of *x*.

We have studied the potential improvements due to the VTX detector in a Monte Carlo simulation. In the simulation, the direct photon events have been generated using the PYTHIA event generator at a fixed interaction point. The recoil jet is then reconstructed from the charged tracks within the VTX detector acceptance ($|\eta|<1.2$) but in the opposite azimuthal direction of the direct photon. In the first step of the algorithm, tracks with momentum greater than 1 GeV/*c* at an azimuth angle opposite to the direct photon ($|\phi - \phi_\gamma| > \pi/2$) are selected. Then, the direction of the jet is estimated as the momentum weighted average of the selected tracks, as:

$$\eta^{jet} = \frac{\sum \eta^i p_T^i}{\sum p_T^i}, \phi^{jet} = \frac{\sum \phi^i p_T^i}{\sum p_T^i}$$

Next, the tracks with momenta above 1.0 GeV/c and within the cone of radius $R = \sqrt{(\eta^{jet} - \eta^i)^2 + (\phi^{jet} - \phi^i)^2} < 0.5$ are selected. In a second iteration the recoil jet axis is corrected with the same algorithm, using the tracks within the cone. This procedure is iterated until the direction of the axis no longer changes.

Figure 32 illustrates how well the direction of the recoil jet is determined by this simple algorithm. In the figure, the pseudo-rapidity η_q of the scattered quark (obtained from the event generator) are plotted as green histograms. The blue histograms in the figure show the distributions of η_q for events in which the recoil jet is reconstructed within the VTX acceptance. The red histograms show the difference $\eta_q - \eta^{jet}$ between the true pseudo-rapidity of the recoil quark and that of the reconstructed jet. The large uncertainty of the recoil jet kinematics, as seen from the wide distribution of η_q, is much reduced by the reconstruction of the recoil jet direction.

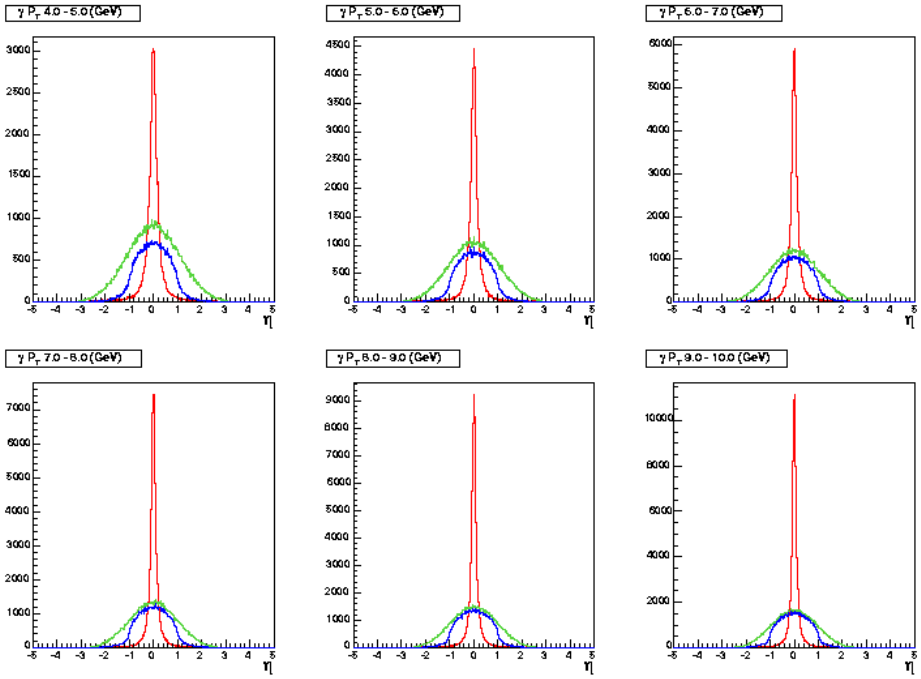

Figure 32 In each panel, the green histogram shows the pseudo-rapidity, η_q-distribution of the final hard scattered partons, which initiated the recoil jet; the blue histogram shows the η_q-distribution of recoil jets within the barrel VTX acceptance; and the red histogram show the $(\eta^{jet} - \eta_q)$-distribution, where η^{jet} is for the pseudo-rapidity reconstructed for the recoil jets. Different panels are for the event samples with direct photon of different transverse momenta, starting from 4-5 GeV/c in the upper left to 9-10 GeV/c in the lower right panel.

From the measurement of η^{jet} and the transverse momentum p_T of the direct photon, the kinematics of the initial partons can be determined. Under the assumption that the p_T of the direct photon and the recoil jet is the same, the fractional momentum of initial partons x_1 and x_2 are determined from the following relations:

$$x_1 + x_2 = \frac{2}{\sqrt{s}}(E^{jet} + E^{\gamma}) = \frac{2p_T}{\sqrt{s}}(\cosh(\eta^{jet}) + \cosh(\eta^{\gamma})),$$

$$x_1 - x_2 = \frac{2}{\sqrt{s}}(p_Z^{jet} + p_Z^{\gamma}) = \frac{2p_T}{\sqrt{s}}(\sinh(\eta^{jet}) + \sinh(\eta^{\gamma}))$$

Thus x_1 and x_2 are calculated as:

$$x_1 = \frac{p_T}{\sqrt{s}}(\exp(\eta^{jet}) + \exp(\eta^{\gamma})),$$

$$x_2 = \frac{p_T}{\sqrt{s}}(\exp(-\eta^{jet}) + \exp(-\eta^{\gamma}))$$

Because we cannot distinguish which of x_1 or x_2 corresponds to the gluon's x, we assume:

$$x_{gluon} = \min[x_1, x_2]$$

$$x_{quark} = \max[x_1, x_2]$$

This is because the gluon distributes in the lower x region than the quark.

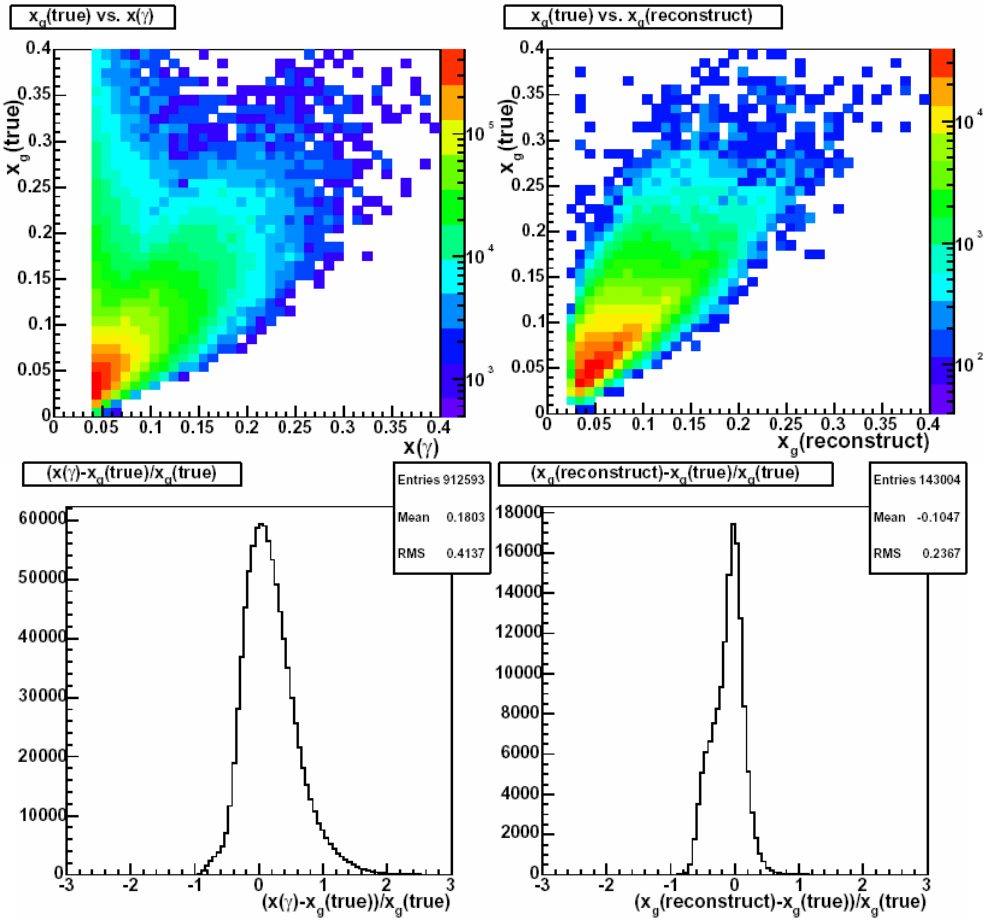

Figure 33 Top panels: correlation between x reconstructed and true x-value from PYTHIA. Bottom panels: (reconstructed-x – true-x) / true-x. In the plots on the left, $x(\gamma) = 2P_T^{\gamma}/\sqrt{S}$ and no jet information has been used. The plots in the right panel are obtained, using the reconstructed jet axes in the barrel VTX.

Figure 33 shows the correlation between the reconstructed x and its true value known from the event generator. If the recoil jet direction is unknown (left panels), the best estimate for x based on the photon p_T is only loosely correlated to the true x. On the other hand, with the recoil jet reconstruction (right panels), there is a narrow correlation between the reconstructed x and its true value.

How well initial gluon's x can be extracted is summarized by Figure 34. Here, the mean values and widths (RMS) of (x(reconstructed) – x(true)) / x(true) are

shown as a function of x_{gluon}. The x-values are determined with an accuracy of ~20%.

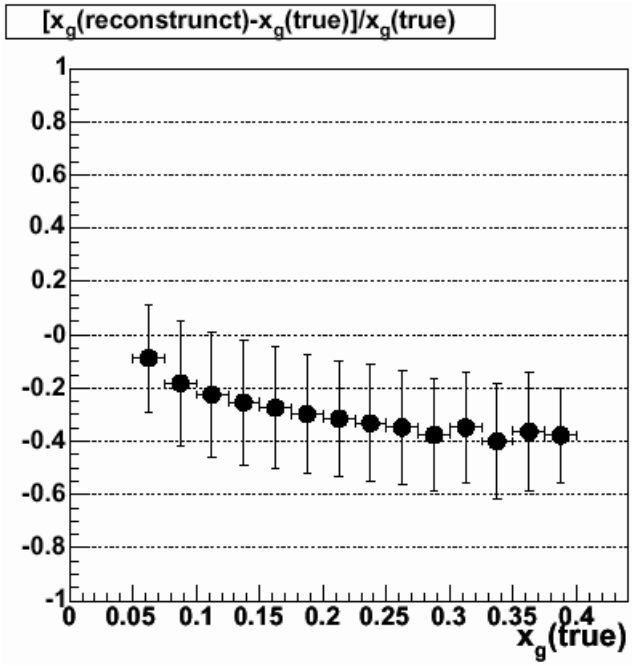

Figure 34 The relative widths (RMS) of the (x(true) – x(reconstruct))/x(true) distributions, using the reconstructed jet axes in the barrel

3.5 Improved momentum resolution and p_T resolution

In the present PHENIX detector, drift chambers that are located outside of the central magnet measure the momentum of the charged particles. Since there is little magnetic field at the location of the drift chambers, charged particles traverse them on almost straight trajectories. The momentum p of a particle is related to the bending angle α measured at the drift chamber approximately as $\delta p/p \sim 87$ mrad/p (p in GeV/c).

The momentum resolution of the central detector will be much improved with the VTX detector. This is because in the present PHENIX central arm spectrometers the effective field kick of 87 mrad GeV/c is only about 40% of the total angular deflection $\Delta\phi$ in the magnetic field. The field integral at the location of the drift chamber is about 0.7 Tm, which gives $\Delta\phi$ = 210 mrad /p. Since the VTX measures the initial direction of the particles the full value of $\Delta\phi$ is measured rather than the angle α at the edge of the magnetic field. In addition, a second field coil, which has been installed in 2003, allows increasing the field integral to roughly 1 Tm. With this field integral the total field-kick increases to 300 mrad GeV/c. The improvement in momentum

resolution is directly given by the ratio of the field kicks $\Delta\phi / \alpha \sim 300$ mrad / 87 mrad ~ 3.

The higher momentum resolution with the VTX detector will improve the high p_T measurements. At present, a momentum resolution of about 1%/p has been achieved. With the VTX detector, the resolution of a 30 GeV/c track can be reduced from 30% to about 10%. In addition, the track confirmation close to the vertex provided by the VTX will eliminate the decay and conversion background, which currently limits the p_T reach of the PHENIX charged particle tracking to $p_T < 10$ GeV/c.

The improvement of the momentum resolution may have a significant impact on the data quality in the higher e^+e^- mass region around the Υ states. With the better momentum resolution also the mass resolution decreases to a level that the members of the Υ family, the resonances Υ_{1S} (9.46 GeV), Υ_{2S} (10.02 GeV) and Υ_{3S} (10.36 GeV) can be clearly separated. This is shown schematically in Figure 35. The VTX together with the increased magnetic field reduces the resolution at the Υ states from ~170 MeV to ~60 MeV for the e^+e^- decay channel. Thus it allows separating the individual states. We note that this measurement will be a significant challenge and only possible if sufficiently high luminosities expected for RHIC II are available for extended running periods.

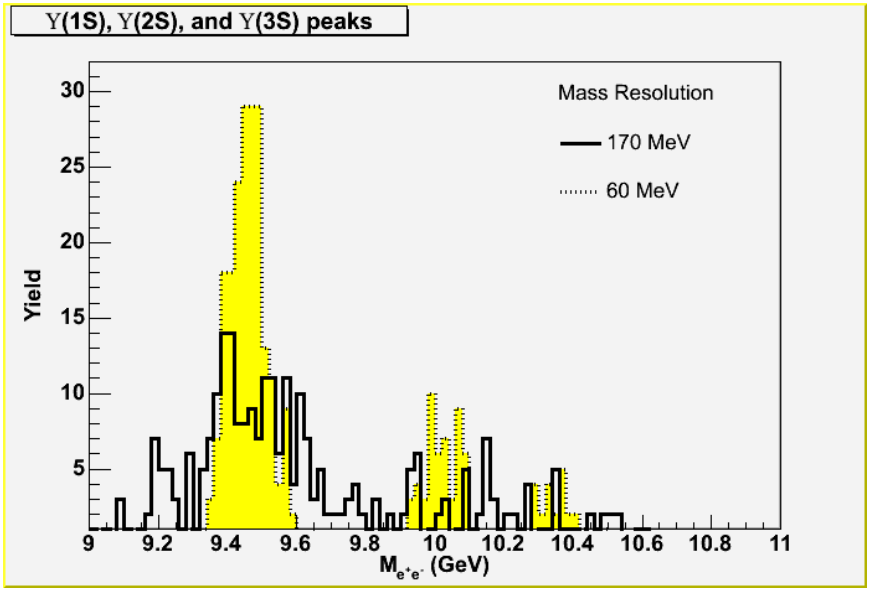

Figure 35 Separation of Upsilon states in the di-electron spectrum with a vertex detector (yellow) and without (black). The number of Υs in this plot represents our expectation for a Au-Au run with a recorded effective luminosity of ~1 nb^{-1} (see chapter 3.5).

3.6 First level trigger capabilities

In central and mid-central Au+Au collisions the present PHENIX minimum bias trigger is sufficient to trigger and select events within the VTX acceptance with high efficiency. However, in *p+p*, *p+A*, light ion, and peripheral Au+Au collisions the min. bias trigger based on the PHENIX beam-beam counters has insufficient efficiency and vertex reconstruction accuracy. The VTX detector will allow overcoming the shortcomings of the present system.

The inner most two layers of the VTX detector are made of Si pixel detector read-out by ALICE pixel chip (see section 4.2 for details). Each ALICE pixel chip provides a general OR of the 32×256 pixels every beam crossing. Thus 106 ns after the beam crossing tracking information about the event is available with a granularity of 160 channels, 10 slices in azimuthal angle φ and 16 slices in beam direction z, and 320 channel, 20 slices in φ and 16 in z, from the 1st and 2nd layer, respectively. The length of a chip along the beams axis is 1.36 cm. We have developed a trigger algorithm which analyzes this information in three steps:

1. Track segments in φ are generated by matching slices at the same φ location in the 1st and 2nd layer. Only events with 2 or more reconstructed φ track segments are processed further.
2. For each φ slice all hits in the 1st layer are combined with all hits in the 2nd layer. The z positions are extrapolated back to the beam axis to identify the possible vertex position. The result of the extrapolation (Figure 36) is histogramed with the same granularity as the z slices.
3. In the final step the maximum in the z histogram is found and required to be within 2 readout chip lengths of the VTX acceptance. Also, the size of the maximum is required to be greater than twice the number of possible tracks in the detector. This last requirement increases the rejection of events which would otherwise trigger due to noise and various physics processes.

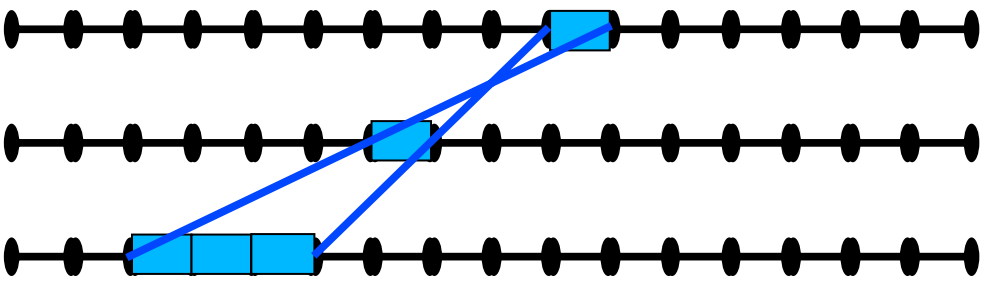

Figure 36 Schematic of step 2 of the algorithm. The upper line corresponds to the outer layer, the middle line to the inner layer, and the lower line to the histogramed beam axis.

The algorithm was tested with 10000 min. bias *p+p* events generated by PYTHIA, which were tracked through the PHENIX GEANT simulation including the VTX. Figure 37 compares the generated event vertex distribution, which has a width of σ = 20 cm, to the distribution of the accepted events. Within the VTX acceptance 90±1% of all events are triggered. This is a substantial improvement over the 50% trigger efficiency of the system currently used in PHENIX. At the same time 95 out of 100 events outside of the VTX acceptance are rejected. As shown in Figure 38the trigger algorithm reconstructs the vertex with an accuracy of σ ~ 1 cm.

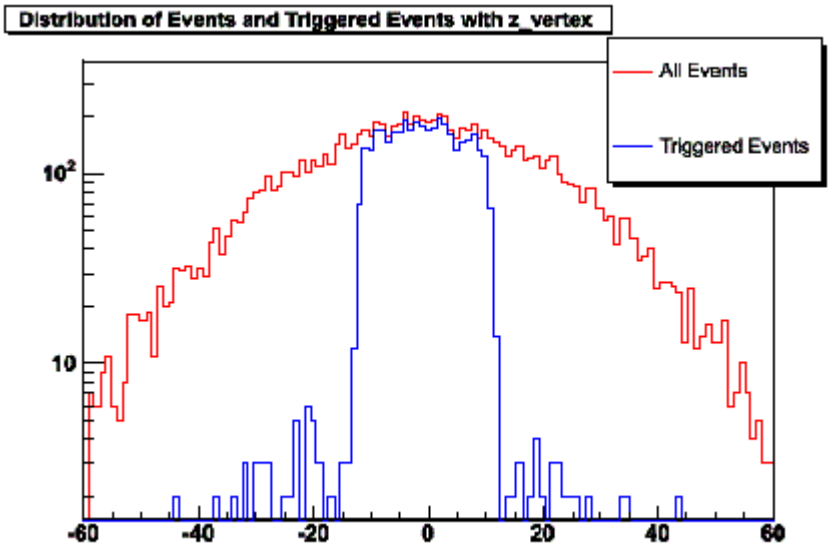

Figure 37 The red curve is shows the event vertex distribution, while the blue curve shows the accepted events. The vertical axis is plotted on a logarithmic scale.

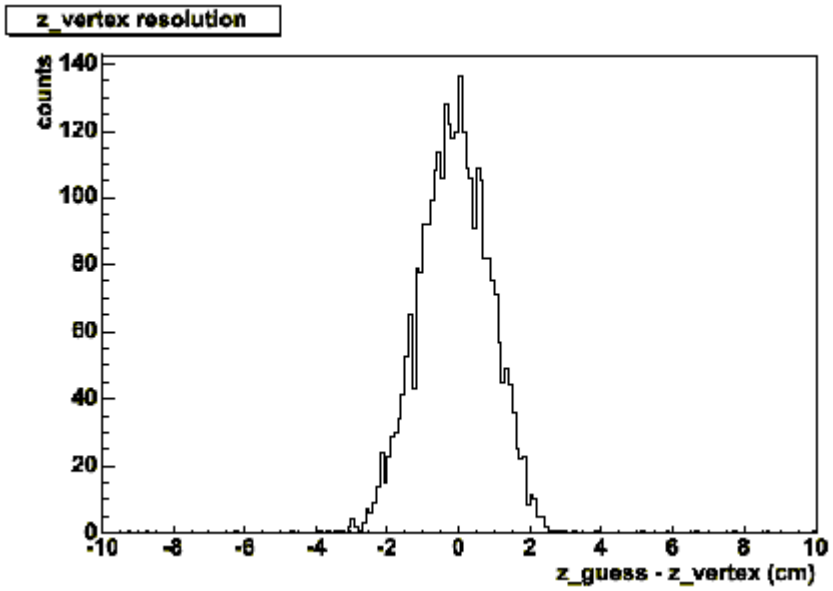

Figure 38 Reconstruction of the vertex. The horizontal axis is the difference between the actual vertex and the position guessed by the algorithm.

The algorithm has also proved to be robust against lateral beam position variations within ±5 mm and against noise at a level of a few %, a level a factor of >10 larger than the performance of these chips observed in the NA60 experiment and in ALICE test beams. In the worst case scenario the efficiency and the rejection both deteriorated by about 6%.

It is worth noting that for *p+p* collisions, the trigger efficiency improves with the multiplicity of the event. For hard processes, this algorithm is expected to have ~100% efficiency.

3.7 Event rate estimates

In this section we estimate the event rates of selected physics processes corresponding to the major goals of the VTX detector. First, we summarize the common assumptions that go into estimating yields for the physics signals that the VTX detector will make available. We start with integrated luminosity estimates, based on the luminosity evolution at RHIC expected by the BNL Collider Accelerator Division. Then we fold in estimates of all of the practical efficiency factors that reduce the yields measured by PHENIX. The obtained "effective luminosity" is then used to estimate the signal yields.

The efficiency factors are summarized in Table 2 for the *p+p*, d+Au and AuAu cases. The first three factors, (1) to (3), are the factors that reduce the CA-D delivered luminosity to the recorded luminosity that is written on data tape by PHENIX, and therefore they are common for all three beam species. These factors are based on the actual performance of RHIC and PHENIX during

RUN2 and RUN3, and to be conservative we assume no improvements of these factors in the future. The largest loss of the recorded luminosity comes from the vertex cuts, factors (1) and (2) in the table. Here we used longitudinal length of the collision diamond of σ=20 cm and a vertex cut of $|z|<10$ cm since the inner-most layer of the VTX detector covers $|z|<11$ cm. The combined reduction of these two factors is gives about 28%. With 60% PHENIX uptime, which was achieved in RUN3, the recorded luminosity is 17% of CA-D delivered luminosity.

The effective luminosity is further reduced by the fraction of "good data" that can be used for offline analysis (the factor (a)) and the offline reconstruction efficiency (the factors (b) and (c)). Again, these numbers are based on actual PHENIX performance and reconstruction efficiency (tracking plus electron identification) for single electrons in central arms in the RUN2 Au+Au data analysis. The reconstruction efficiency includes the loss due to the dead channels in the central arm detectors. The efficiency depends on the beam species, and it decreases from *p+p* to d+Au to Au+Au. This reduction is caused by occupancy dependent efficiency losses, which are also based on the actual performance in RUN2 data analysis. The reconstruction efficiency factors are shown for both single electron (factor (b)) and electron pairs (factor (c)).

We should emphasize that the reality factors given in Table 1 are all based on achieved performance of RHIC and PHENIX and we assume no improvement in the future. Therefore the effective luminosity presented here is a very conservative estimate and potential improvements will increase the effective luminosity usable by the VTX detector. In particular, improvement in diamond size of the beam and the efficiency of the storage RF would greatly increase the effective luminosity.

In Table 3 we list the delivered integrated luminosity, the recorded integrated luminosity with the VTX (delivered integrated luminosity times factor (4) in Table 2), and the effective integrated luminosity. For the delivered integrated luminosity, we used the CA-*D* projection of the RHIC luminosity in year 2008 RUN and assume constant effort, which means 19 weeks of physics data taking per year. Since there is a very large variation of the CA-D luminosity projection, we use the average of the most pessimistic estimate and the most optimistic estimate. This luminosity estimate is consistent with the five year extended beam use proposal presented by PHENIX to the Physics Advisory Committee (PAC) in the fall 2003. The most optimistic luminosity figure is about a factor of 2 larger than shown in the table.

Table 2 Table of efficiency factors that must be applied to delivered *p+p*, d+Au and Au+Au luminosities to calculate expected signal yields. The single and two track reconstruction efficiencies are for electrons in the central arm.

Quantity	*p+p* factor	d+Au factor	Au+Au factor
(1) Storage RF efficiency	75 %	75 %	75 %
(2) Event vertex cut (±10 cm)	38 %	38 %	38 %
(3) PHENIX uptime	60 %	60 %	60 %
(4) $L^{\text{recorded}}/L^{\text{delivered}}$ =(1)×(2)×(3)	17%	17%	17%
(a) Good run fraction	80 %	80 %	80 %
(b)Single track efficiency	85 %	80 %	50 %
(c) Two track efficiency	72 %	64 %	25 %
Total (single track)=(4)×(a)×(b)	12 %	11 %	6.8 %
Total (two track)=(4)×(a)×(c)	10 %	8.8 %	3.4 %

Table 3 Table of effective luminosities from a 19 week production run, after reality factors are taken into account. The delivered luminosities use the average of the most pessimistic and most optimistic C-AD estimates of how the luminosity will evolve by 2008-2009. The signal yield for a given process is found by multiplying the cross section for the process by the effective luminosity and by the detector acceptance. For d+Au and Au+Au collisions and the effective *Ldt* columns, the nucleon-nucleon luminosities are shown in the parenthesis).

beam species	$\sqrt{s_{NN}}$	delivered Ldt	recorded Ldt	Effective Ldt	
				Single track	Double track
p+p	200	160/pb	27/pb	18/pb	15/pb
d+Au	200	40/nb	6.8/nb	4.4/nb (1.7/pb)	3.5/nb (1.4/pb)
Au+Au	200	2.2/nb	370/μb	150/ub (5.8/pb)	74/μb (2.9/pb)
p+p	500	540/pb	93/pb	63/pb	54/pb

In Table 4, the estimated signal yields of selected physics processes are summarized. The "Yield" column of the table shows the raw signal yield calculated as the product of the cross section, the geometrical acceptance of the central arms, and the effective luminosity given in Table 3. However, most of these raw signal yields cannot be measured or cannot be separated from other competing process without the VTX detector. The column "no VTX" indicates which of the physics signals can be measured without the VTX detector (marked as "Yes") or not (marked as "No"). If the signal can be measured with limitations or with a large systematic uncertainty, the column is marked as "Limited". For example, in charm decay electron measurement ($c \rightarrow e$), the first row ($1 < p_T < 2$ GeV/c) is marked as "Yes" since charm is the dominant source of non-photonic electron in this p_T bin. The next row ($2 < p_T < 3$ GeV/c) is marked as "Limited" since there is a large uncertainty due to the beauty contribution. All other rows are marked as "No" since it is not possible to separate charm signal from the larger beauty signal for $p_T > 3$ GeV/c without the VTX detector. In these p_T bins, the measurement of beauty decay electron ($b \rightarrow e$) are marked as "Limited" since we cannot separate b and c

signal in a model independent way, but the beauty contribution is larger than the charm contribution.

For the yield estimate of single electron from open charm ($c \rightarrow e$), the momentum distribution of the charm decay electron is calculated using PYTHIA event generator. The generator is tuned to re-produce the low energy charm data from fixed target experiments and single electron data at the ISR. The electron spectrum predicted by the tuned PYTHIA simulation agrees well with PHENIX data at $\sqrt{s_{NN}}$ =130 GeV and 200 GeV. The corresponding total charm cross at $\sqrt{s_{NN}}$ =200 GeV is 650 μb per nucleon-nucleon collisions. The single electron spectrum is then scaled assuming the binary scaling, and then multiplied by the geometrical acceptance and the effective luminosity to give the expected yield (sum of e^+ and e^-) shown in the "Yield" column in the table. The expected yield in low p_T region ($p_T \leq 3$ GeV/c) is consistent with the observed charm decay electron yield in RUN2 Au+Au data. Since this estimate comes from a scaled *p+p* PYTHIA simulation, it corresponds to a scenario with no charm enhancement nor any energy loss. If there is a substantial energy loss of charm in high p_T, the actual yield of charm decay electron could be smaller than the value in the table. On the other hand, recent results from RHIC *p+p* and d+Au collision indicate that PYTHIA underestimate the yield of *D* and $D \rightarrow e$ in high p_T by at least a factor of 2. Thus the rate and yield estimate in the table should be considered as a lower limit if there is no suppression of high p_T charm in Au+Au.

The yield of single electron from open beauty is estimated in a similar way using PYTIA generator, assuming that total beauty cross section is $\sigma_{b\bar{b}}$ = 3.8 μb per N-N collisions. This cross section is estimated by tuning the PYTHIA calculation of *b* production with *b* production data from the Tevatron (1.8 TeV) and $Sp\bar{p}S$ collider (630 GeV) and then extrapolating down to lower energies at RHIC (200 GeV). Binary scaling of the cross section is assumed for the Au+Au estimates.

For both the charm and beauty decay electron measurements, the signal yields with DCA > 200μm are shown in the column labeled "with DCA cut". With the DCA cut, beauty is dominant over charm for p_T >2 GeV/*c*, and can be separated from the charm signal. In the lowest p_T bin ($1.0<p_T<2.0$ GeV/*c*), charm is still dominant over beauty by about factor 5 with this DCA cut. The *b/c* ratio is improved to ~1/2 with tighter DCA cuts (DCA>400μm), as shown in the table, and *b/c* ratio becomes about 1 with DCA>800μm (see Figure 30). Using the DCA distribution, we can statistically separate the *b*-decay signal from charm over the range $1<p_T<6$ GeV/c. The table shows that even with the pessimistic assumptions used in the estimate, we will have sufficient statistics for a *b/c* signal separation in this p_T range. Although the e/π

separation power of the RICH detector is reduced above its Cereknov threshold for pions (p_T>4.7 GeV/c), the RICH+EMCAL combination has a sufficient e/π separation up to this p_T range.

As discussed earlier, one of interesting measurement with the VTX is the ratio of $(c\rightarrow e)/(b\rightarrow e)$ and its centrality dependence. Since most of the systematic uncertainties cancelled in this ratio, the measurement is primarily limited by the *b/c* separation from the DCA measurement and the statistics of $b\rightarrow e$. The expected yield of *b* and *c* signal with and without the DCA cuts in Table 4 shows that we can reach ~1% statistical precision in the ratio measurement.

A summary the physics program addressed with the VTX detector and how it compares to the capabilities without the VTX is given in Table 5. For many of these physics topics, a measurement is not possible without the VTX detector or very marginal. For the processes that PHENIX can measure without the VTX detector, the VTX will substantially extend the kinematical range of the measurement. In addition, the accuracy and the precision of the measurements are improved.

Table 4 Event rate calculated for selected physics processes. The effective integrated luminosity used in the calculation is shown in Table 3. For the meaning of "no VTX" column, see the text. In both of Au+Au and *p+p*, the collision energy $\sqrt{s_{NN}}$ is 200 GeV per nucleon pair. The yields include the anti-particle channels. The DCA cut value for the single electron measurement is DCA>200 μm. For the lowest p_T bin, the number with DCA>400μm is shown in parenthesis. The number in $D \rightarrow K\pi$ is for 200M central collisions, while other numbers are for min. bias.

Process	no VTX	Yield	Yield with DCA cuts
AuAu→*c*→*e*			
1.0<p_T<2.0 GeV/c	Yes	3M	150K (40K)
2.0<p_T<3.0 GeV/c	Limited	130K	6K
3.0<p_T<4.0 GeV/c	No	5K	0.3K
4.0<p_T<5.0 GeV/c	No	1K	50
5.0<p_T<6.0 GeV/c	No	0.2K	10
AuAu→*b*→*e*			
1.0<p_T<2.0 GeV/c	No	200K	50K (20K)
2.0<p_T<3.0 GeV/c	No	70K	15K
3.0<p_T<4.0 GeV/c	Limited	17K	3K
4.0<p_T<5.0 GeV/c	Limited	4K	0.7K
5.0<p_T<6.0 GeV/c	Limited	1K	0.2K
Au+Au→*D*→*K*π (central)			
p_T >2 GeV/c	No	4900 (*S/B*~0.1%)	1000 (*S/B*~3%)
p_T >3 GeV/c	No	2900 (*S/B*~1%)	600 (*S/B* ~5%)
Au+Au→*B*→*J*/ψ→*e e*	No	100	50
p+p→*c*→*e*			
1<p_T<3 GeV/c	Yes	10M	0.5M
p_T>3 GeV/c	No	20 K	1K
p+p→*b*→*e*			
p_T>1 GeV/c	No	0.9M	0.2M
p+p→γ+jet			
4<p_T<5 GeV/c	No	300K	N.A.
5<p_T<6 GeV/c	No	150K	N.A.
6<p_T<7 GeV/c	No	70K	N.A.
7<p_T<8 GeV/c	No	40K	N.A.
8<p_T<9 GeV/c	No	20K	N.A.
9<p_T<10 GeV/c	No	12K	N.A.
p+p→*B*→*J*/ψ→*ee*	No	560	280

Table 5 Summary of physics measurement gained by the VTX detector. The column "without VTX" shows the present capability of PHENIX, while the measurement range with the VTX detector is shown in the column "with VTX". If the process is not measurable, it is marked as "No".

Process	Physics Objectives	Without VTX	With VTX
$c \rightarrow e$	Charm energy loss	$0.5 < p_T < 2.5$ GeV/c	$0.3 < p_T < 6$ GeV/c
$D \rightarrow K\pi$ (p_T>2 GeV/c)	Charm energy loss	No (2σ significance in central Au+Au)	> 7 σ significance in central Au+Au
Total charm yield	Charm production	~ 20 %	~ 10 %
$(c \rightarrow e)/(b \rightarrow e)$ ratio	Search for thermal charm produciton	No	~ 1 %
$b \rightarrow e$	Beauty production Beauty energy loss	p_T>3 GeV/c with model dependence	$1 < p_T < 6$ GeV/c
$B \rightarrow J/\psi$	Beauty production	No	$\Delta\sigma/\sigma$ ~ 10 - 15 %
Total beauty yield	Beauty production	No	~ 10 %
High p_T charged	Light quark energy loss	$p_T \leq 10$ GeV/c	$p_T < 15$ -20 GeV/c
$p+p \rightarrow c \rightarrow e$	$\Delta G(x)$	$0.03 < x < 0.08$	$0.01 < x < 0.15$
$p+p \rightarrow b \rightarrow e$	$\Delta G(x)$	No	$0.02 < x < 0.15$
$p+p \rightarrow \gamma$+jets	$\Delta G(x)$	No	$0.04 < x < 0.3$
$p+A$ (dA) $\rightarrow$ c/b	Nuclear shadowing of $G(x)$	$0.03 < x < 0.3$	$0.01 < x < 0.3$

4. VTX Detector system

4.1 Overview

The VTX detector system is composed of 4 layers of silicon detectors: two inner layers with silicon pixel hybrid detectors and two outer layers with silicon strip detectors. A 3-D view of the detectors is shown in Figure 39 and its cross sectional views are shown in Figure 16 in the previous chapter. The geometrical dimensions of the pixel layers and the strip layers are summarized in Table 6 and Table 7, respectively.

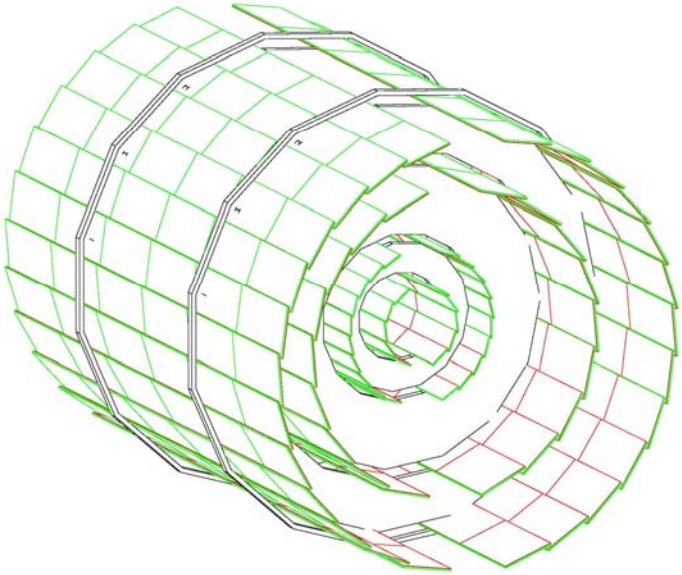

Figure 39 GEANT model of the VTX detector. It consisted of the inner-most pixel layer and three outer strip layers.

For the inner two layers we use silicon pixel detectors. The technology is the ALICE1LHCb sensor-readout hybrid, which was developed at CERN for the ALICE and LHCb experiment. The 200 μm thick silicon sensor holds 32×256×4 cells, or pixels, each with an active area of 50×425 μm^2. The sensor is bump bonded to four matching readout chips of 150 μm thickness, and each of the read-out chips has 32×256 individual amplifier discriminator channels. The readout chip also holds the electronics to pipeline the data flow.

We call a sensor chip bump-bonded to 4 readout chips a sensor module. Two sensor modules are wire-bonded on to a thin, high fine-pitch, multi-layered readout bus (pixel bus), which is connected to a bus extender. A unit of two sensor modules, a pixel bus, and a bus extender forms a basic read-out unit of the pixel system, which we call a half ladder. This sub-detector is read-out by an electronics module, Silicon Pixel Intermediate Read-Out (SPIRO) module. A SPIRO module provides all service voltages, control and timing signals, and reads out the pixel data. A SPIRO module transmits the data via optical fiber from the detector for further processing.

Table 6 Summary of main parameters of the inner 2 pixel layers.

VTX	Layer	R1	R2
Geometrical dimensions	R (cm)	2.5	5
	Δz (cm)	21.8	21.8
	Area (cm^2)	280	560
	Sensor maxtrix size	1.28 cm × 1.36 cm	
	Pixel size	50 × 425 μm^2	
Channel counts	Pixels per ROC	32 × 256 = 8192	
	ROCs per sensor module	4	
	Sensor modules per half-ladder	2	
	Half-ladders per ladder	2	
	Ladders	10	20
	Readout chips	160	320
	Readout channels	1,310,720	2,621,440
Radiation length (X/X0)	Sensor (200 μm)	0.22 %	
	ROC (150 μm)	0.16 %	
	Bus	0.28 %	
	Mechanical stave	0.70 %	
	coolant	0.08%	
	Total	1.44 %	

Mechanically, two half ladders are supported on a mechanical stave, which provides mechanical support as well as cooling of the system. Two half ladders mounted on a mechanical stave form a full ladder which spans approximately 22 cm in beam direction. Five such ladders on each side of the beam pipe result in almost full azimuthal coverage. A total of 10 ladders or 20 half ladders complete the inner-most layer. The second layer is composed of 20 ladders or 40 half ladders. The combined materials of silicon sensors, readout chips, readout

buses and mechanical structure including cooling add up to about 1.5 % per layer of a radiation length. Table 6 summarizes the main parameter of the two pixel layers. The pixel detector system is discussed in more detail in the following sub sections.

The two outer layers employ silicon strip sensors. The sensor, developed by the BNL Instrumentation Division, allows stereoscopic readout on a single sided sensor. Each sensor is about 3.43×6.36 cm^2, with 2×384 of X-strips of 80 μm width and 3.1 cm length in beam direction and the same number of U-strips at an angle of 4.6^0 to the beam direction. Due to the stereoscopic readout the effective pixel size is 80×1000 μm. Five (for layer 3) or six (for layer 4) sensors are mounted in a ladder. The full length of a ladder in the beam direction is 31.8 cm (for layer 3) or 38.2 cm (for layer 4). A total of 44 ladders are required to cover the azimuth acceptance as shown in Figure 39.

Table 7: Summary of main parameters of the 2 strip layers.

VTX	Layer	R3	R4
Geometrical dimensions	R (cm)	10	14
	Δz (cm)	31.8	38.2
	Area (cm^2)	1960	3400
	Sensor size	3.43 cm × 6.36 cm	
	Strip size	80 μm × 3 cm	
	Effective pixel size	80μm × 1000 μm	
Channel count	strips per sensor	384 × 2 strips × 2	
	# of channel per SVX4	128	
	SVX4 per sensor	12 (= 3 × 2 strips × 2)	
	Sensors per ladder	5	6
	# of Ladders	18	26
	# of Sensors	90	156
	SVX4	1080	1872
	Readout channels	138,240	239,616
Radiation length (X/X0)	Sensor (625 μm)	0.67 %	
	ROC	0.64 %	
	Mechanical stave	0.70 %	
	coolant	0.08%	
	Total	2.1 %	

Each strip sensor is wire-bonded to and read-out by twelve read-out SVX4 ASICs, six per orientation, and there are 128 channels on each SVX4 chip. FNAL and LBNL have developed these chips for other silicon vertex detectors. The twelve SVX4s servicing each sensor are mounted on a readout cards (ROC) and are readout by a custom, digital ASICs (RCC). These chips compress and parallelize the data sufficiently to meet PHENIX readout speed requirements. Power, serial control, timing and readout for a ladder are all carried on the ROC's, which are bussed together via wire-bonding at their edges (one bus per orientation). This bus runs the length of a ladder and out of the acceptance to a Front End Module (FEM), which transmits the data via an optical fiber for further processing. The present estimate is that the mechanical support, ROC's and sensor add up to about 2.1 % of a radiation length.

4.2 Pixel Detector

The inner two layers of the vertex tracker will be built based on silicon pixel devices designed for the ALICE experiment at CERN. The ALICE collaboration has developed and is now constructing a silicon pixel detector for its inner tracker. This detector system has to fulfill similar requirements as the inner layer of the vertex detector proposed for PHENIX. The pixel detector and the ALICE LHCb read-out chip were also successfully used in the silicon vertex spectrometer of NA60 experiment. The full telescope with 16 detector planes was installed and operational in the NA60 experiment during the physics run with high-energy Indium beams in Fall 2003, and the first physics results from the experiment have been reported in 2005. We therefore will develop and built the inner two layers for PHENIX in close collaboration with ALICE.

For PHENIX, 4 pixel read-out chip bump-bonded on a sensor chip forms a sensor module. Two sensor modules, a pixel bus and a bus extender form a half ladder, which is the basic read-out unit of the pixel detector. This basic detector unit is read-out by a SPRIO module. SPIRO modules are placed outside of the detector acceptance. They process the incoming control signals and transmit the outgoing data of a pixel half ladder. A SPRIO module carries analog Pilot chips for the power and reference voltage supplies of the pixel readout chips, digital Pilot chips for their controls and readout, and an optical link chips and transmitters for the data transfer. The SPIRO modules are then connected to pixel Front End Modules (FEMs) outside of the PHENIX IR. The FEMs work as interface to the PHENIX DAQ system. The read-out scheme of the pixel system is illustrated in Figure 40.

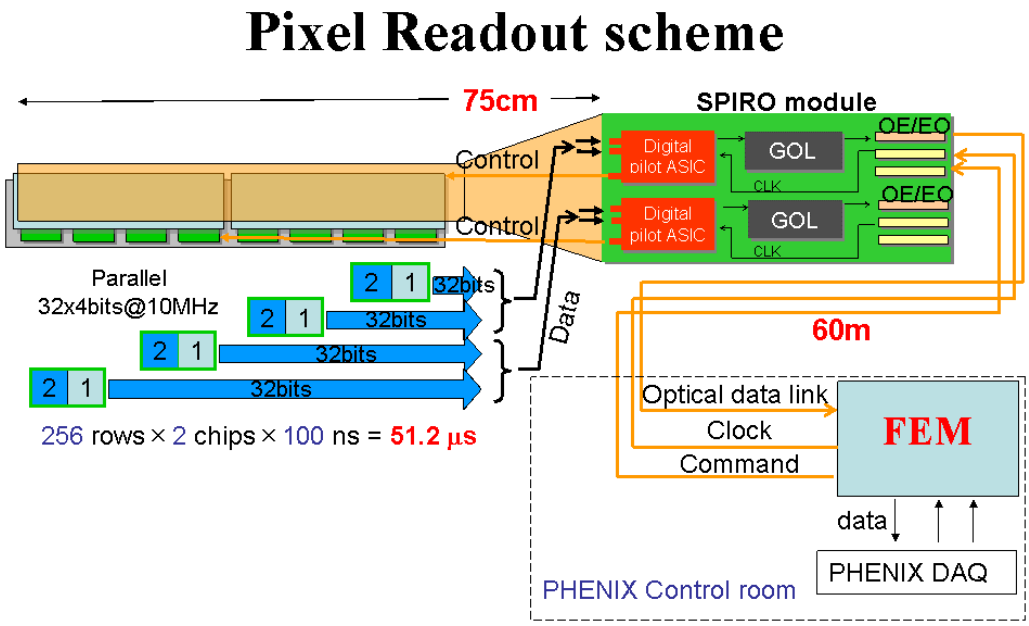

Figure 40 Schematic diagram of pixel electronic system

Pixel Sensor

The pixel detector sensors are designed in a planar technology of CANBERRA and produced as *p*-in-*n* structures on 5" silicon wafers of 200 µm thickness. A pixel cell is defined by p^+ implants in one side of the *n*-type silicon. The pixel dimensions are 50 µm by 425 µm. Every sensor pixel has a contact pad for bump-bonding to the matching electronics pixel on the readout chip.

The array of 32 by 256 pixels is read-out by a single readout chip. The array is surrounded by a guard ring electrode that protects the detection area from leakage currents deteriorating the signals generated by charged particles in the depleted silicon. The guard ring also encircles a "snake" structure intended for quality tests of the bump bonding during the mass production of the assemblies. Those "snakes" have matching structures and contact pads for probing access on the readout chip. A scribe line defines the outer dimensions of the device for the wafer dicing and also contains alignment marks. Figure 41 shows a photograph of a corner of such sensor.

A sensor chip as produced for ALICE pixel detectors and the NA60 pixel vertex spectrometer is of 12.8 by 13.6 mm^2 size and contains an array of 32 by 256 pixels. On a PHENIX pixel sensor chip, four such sensor pixel arrays are

implemented in a linear arrangement on a single substrate[1]. The long side of the pixels is parallel to the long direction of the chip. The 200 μm thick sensors deplete typically at 12V applied to the aluminized n^+ implanted continuous back plane. During operation in the experiment, the sensors are over-biased. The leakage currents are as low as a few nA in well diced material but can go up to a few μA without any danger to the sensors' functionality.

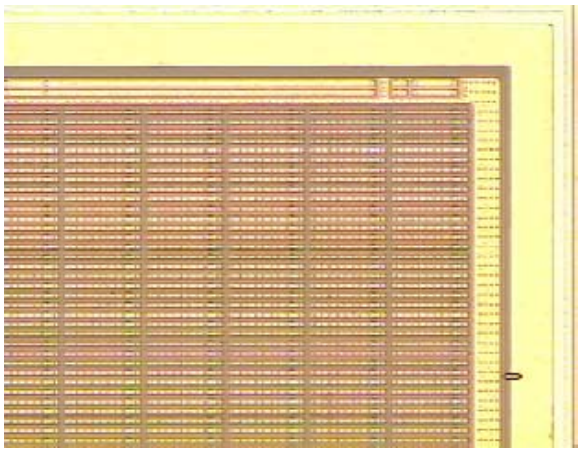

Figure 41 Photograph of a corner of a pixel detector sensor chip, seen through a microscope. A guard electrode surrounds the array of pixel implants. The scribe line defines the outer dimensions of the die.

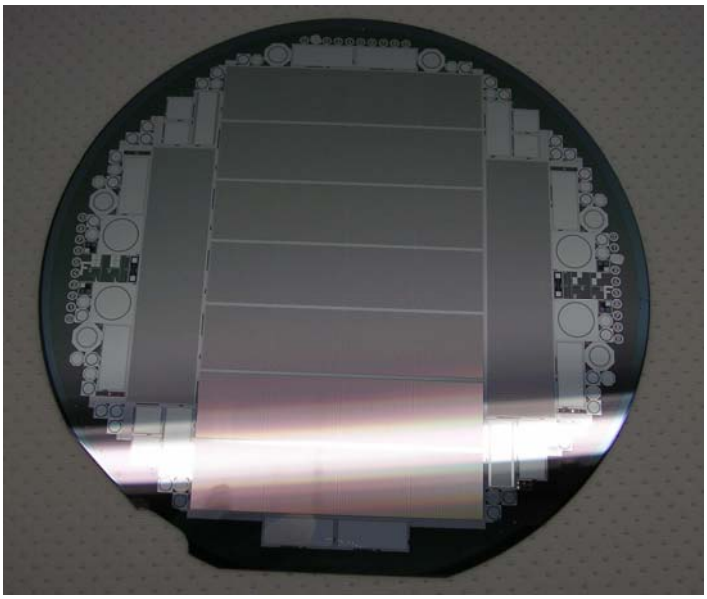

Figure 42 A picture of a 5" silicon sensor wafer with nine PHENIX pixel sensors.

[1] A NA60 sensor chip is read-out by single read-out chip. A PHENIX sensor chip is read-out by 4 read-out chips. An ALICE sensor chip (production version) is read-out by 5 read-out chips.

Nine PHENIX sensor ladders with four pixel arrays each are arranged on the production mask of a 5" wafer as shown in Figure 42. Diodes are placed in the remaining space. They are production-specific to the CANBERRA technology and serve the quality survey. RIKEN has purchased sufficient number of sensor wafers that is needed to build 150 sensor modules.

Pixel Readout chip (ROC)

The pixel detector readout chip (ROC) is a result from a research and development effort at CERN that started more than a decade ago[45]. The recent chip "ALICE1LHCb" is a mixed analog-digital ASIC designed in CERN's EP-MIC group and the ALICE and LHCb teams for an application in the Silicon Pixel Detector of the ALICE experiment and the RICH photo detection of the LHCb experiment at the LHC[46]. It is also being applied in the vertex spectrometer of the NA60 experiment at the SPS[47]. The chip is designed in a 0.25 μm process with radiation tolerant design layout techniques. Each chip has 32 by 256 pixels of 50 μm by 425 μm size. It is designed to be bump-bonded with solder balls of about 20 μm diameter to a silicon sensor that contains an array of sensor pixels with matching size and pitch. The chip provides a binary output signal for every pixel that indicates a charge release by a traversing particle. The threshold of the pixels' discriminators and various other parameters of the front-end electronics can be adjusted and programmed individually for every pixel. Each ALICE1LHCb chip is readout by clocking out 256 32-bit words at a frequency of 10 MHz. Every chip provides an "OR" signal of hit pixels for each readout clock cycle. This feature will allow us to utilize the pixel detector for the first-level trigger logic.

Q/A of the pixel ROC

RIKEN group has carried out quality assurance (Q/A) tests of the pixel read-out chips for the VTX project, initially at CERN, and then at RIKEN. A semi-automatic wafer probe station (model SÜSS PA200) was installed by RIKEN at CERN for the Q/A tests of the readout chips on the wafers. The picture of the probe station and a photograph taken during Q/A tests at CERN are shown in Figure 43. After the initial phase of the tests was completed, the probe station system has been moved to RIKEN Wako campus. The system is used further tests of the pixel readout chips and sensor modules at RIKEN.

Figure 43 Left: Picture of the wafer probe station installed at CERN for the quality assurance tests of the pixel readout chips. Right: Quality assurance test of ALICE1LHCb readout chips in a clean room laboratory at CERN.

The tests performed on the chips include an evaluation of the analog and digital power consumptions, the functionality of the analog and digital controls, and the minimum threshold and noise obtained in response to electrical test signals. Tests of the OR trigger output are included as well. The chips are sorted into three quality classes (I – excellent, II – good, III- bad). Class-I chips are used for the production of the pixel detector ladders. A typical class map of a readout chip wafer is shown in Figure 44.

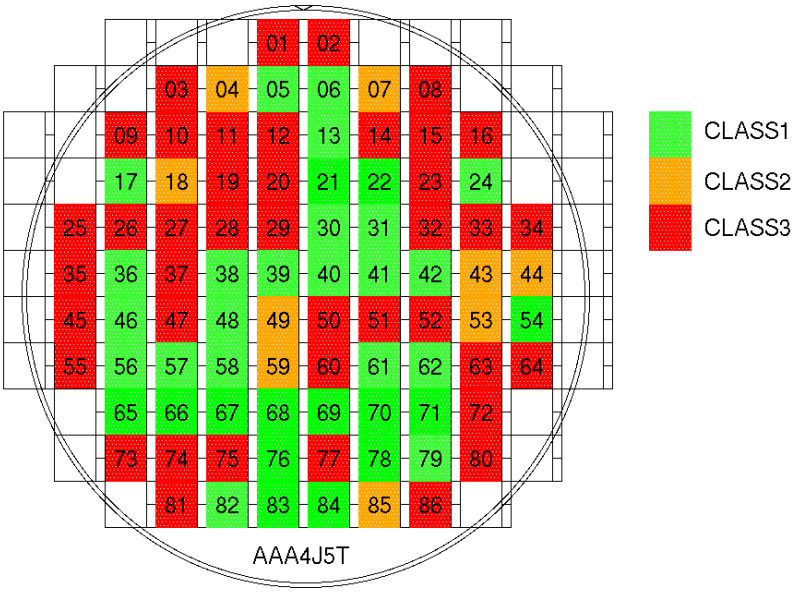

Figure 44 A typical class map of the readout chip wafer.

A total number of 977 ROCs have been probed on the chip wafers as of April 2006, and 641 class-I chips have been obtained. The Q/A results are

summarized in Table 8. The yield of class-I chips from the tested PHENIX wafers is consistent with the results obtained by the ALICE pixel detector group. Those class-I chips and pixel sensors will be sent to VTT, where they will be bump-bonded to form sensor modules. Under a CERN-RIKEN contract, 150 good bump-bonded sensor modules will be produced. The 641 class-I chips are sufficient to make 150 sensor modules covered by the contract. RIKEN has purchased 25 more readout chip wafers which are not probed yet. If additional ROCs are needed, they will be probed at RIKEN.

The mean minimum threshold and noise distributions for the 641 class-I chips and the 171 class-II chips obtained from the Q/A tests are shown in Figure 45. The mean minimum thresholds of the class-I chips is 1508 e^-. The mean noise is found to be 116 e^-. For single pixel hits the average sensor signal from minimum ionizing particles in 200 μm Si is about 16 000 e^- so that a superb signal-to-noise ratio and particle detection efficiency is achieved.

Table 8 Yield of class-I, class-II and class-III chips from four probed wafers.

Wafer ID	Class-I	Class-II	Class-III
ABA4J4T	40	4	42
AAA4J5T	32	2	52
A9A4J6T	26	5	55
AVA4LJT	39	20	27
ATA4LLT	24	28	34
A3A4JCT	36	12	38
AXA4LHT	33	19	34
AZA4IZT	22	3	61
ATA4I5T	44	6	36
AZA4E1T	28	4	54
ACA4J3T	0	1	85
AQA4DTT	11	0	75
A9A4ERT	31	5	50
AWA4E4T	41	13	32
ANA4M8T	31	0	55
ALA4MAT	6	25	55
PJVM15T	41	9	36
PWVM1TT	41	2	43
P0VM1PT	46	5	35
PCVM1CT	33	5	48
P6VM1IT	36	3	30
Total	641	171	977
Yield	36%	10%	55%

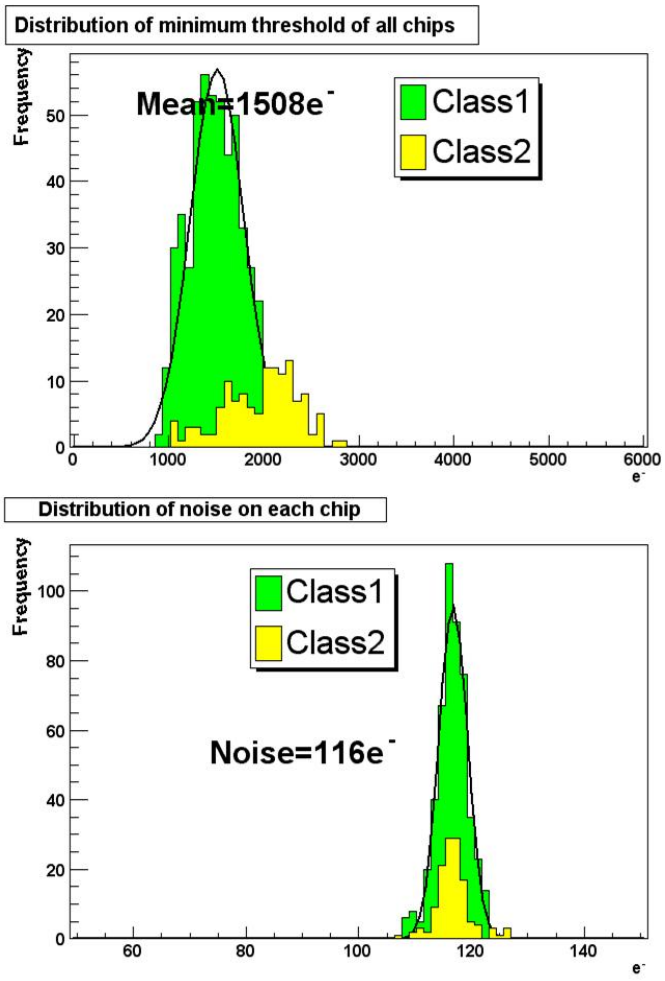

Figure 45 Mean threshold (top) and noise (bottom) of the 641 class-I (green) and the 171 class-II(yellow) readout chips obtained from the Q/A tests.

Interconnection of Sensor and Readout Chip ("Bump Bonding")

The term "bump-bonding" denotes the micro-interconnection of electrical structures with small "balls" of metals or alloys. It is essential for the construction of modern hybrid structures with two-dimensional arrays of high-density designs. Bump-bonding and flip-chip interconnection techniques were already introduced in the late 1960s. They became commercially available only about 15 years ago. Bonding with dimensions smaller than approximately 50 μm is still offered by only a rather small number of vendors or specialized laboratories, and becomes challenging at below 20 μm for specialized applications.

The Technical Research Centre of Finland (VTT), Microelectronics Department of the Information Technology Division, is the vendor of choice at CERN for the production of flip-chip assembled pixel detectors for the ALICE and LHCb experiments. VTT offers an integrated package of bump-bond deposition, wafer thinning and flip-chip bonding[48]. Key features of the process are:

- 200-mm (8") wafer capability.
- Tin-lead solder alloy bumps are used for mechanical strength of the bonded assemblies.
- Bump deposition by electroplating.
- Optional thinning (back grinding) of bumped readout wafers from native thickness of 750 μm down to 150 μm.
- Clean dicing with front side protection using either photo resist or tape.
- Flux-less flip-chip bonding. Alignment accuracy better than 3μm.
- Bump size down to smaller than 20μm diameter.
- Throughput 3-4 assembly bondings per hour.

The requirement for thinnest possible detectors especially in the internal layers of the vertex detector, to minimize multiple scattering and photon conversion, demands the thinning of the readout chips. The native thickness of electronics wafers is 750 μm when they leave the foundry. Since they are processed only from one side, in a layer of only a few micron depths, a large fraction of the bulk can be removed without affecting the electrical properties of the chip. Sensor wafers are processed from both sides to establish the p-in-n structures, and have to be directly produced in their final thickness. At VTT, a procedure has been developed to thin readout chips in a way that conforms to the mechanical stability requirements for bump-bonding and flip-chip assembly. After the electrolytic deposition of solder bumps on a full readout wafer, and before the flip-chip process is performed, the wafer's surface is first protected with a removable film. The backside is then grinded mechanically in several steps. Finally, wet chemical etching or chemical mechanical polishing removes the defect layer. The minimum thickness achieved with 8" wafers is 150 μm, with thickness variations of less than 5 μm.

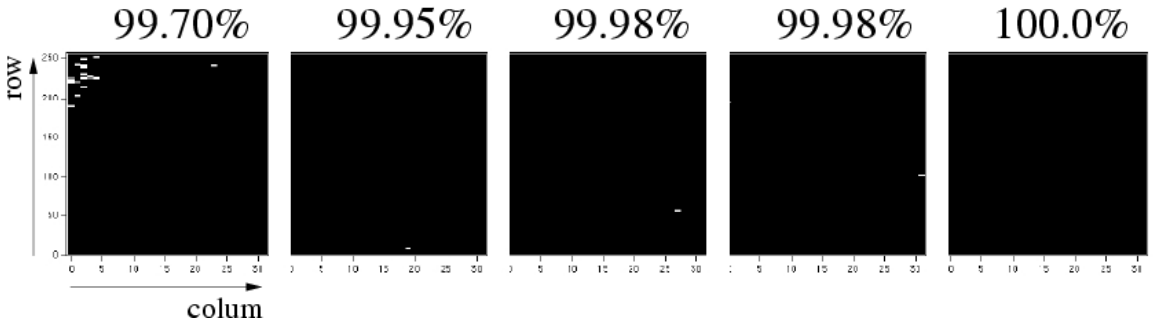

Figure 46 Map of working pixels from a source measurement of one of the first thin ALICE pixel sensor assemblies. The sensor assembly consists of five thinned readout chips of 150 µm thickness that are bump-bonded to a 200 µm thick silicon sensor substrate. The fraction of working pixels is indicated for every chip.

A sizable number of thin sensor assemblies have already been produced for the ALICE experiment prior to the start of the mass production. The test production yielded well working devices. Figure 46 illustrates a test result from one thinned sensor assembly with five readout chips[49].

Under a RIKEN-CERN contract, total of 150 good bump bonded sensor modules will be produced and delivered by VTT. As the first batch of the production, total of 18 PHENIX sensor modules has been produced and delivered in Dec 2005. Figure 47 shows a picture of four of the first PHENIX sensor modules. These sensor modules have been checked initially at CERN and then at RIKEN. Figure 48 shows results of the tests. Clear images of a beta ray source can be seen. In the sensor module in Figure 48, the fraction of the dead pixel is much less than 1 %.

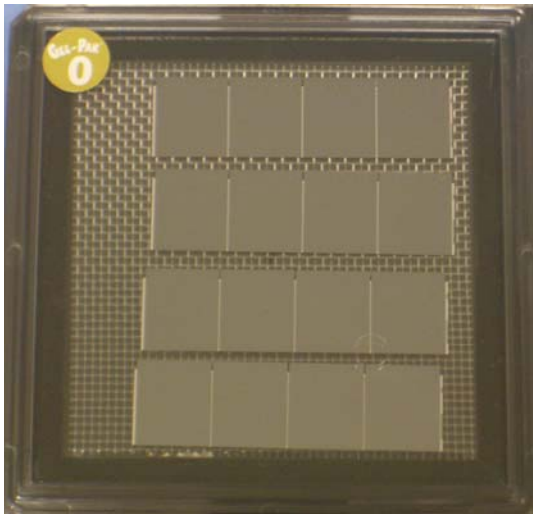

Figure 47 The first four bump bonded sensor modules for PHENIX produced at VTT and delivered to CERN

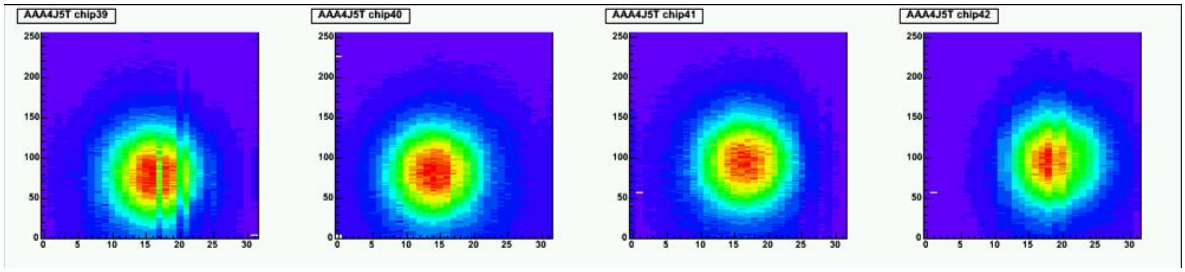

Figure 48 Test results of the first PHENIX sensor modules. Image of a beta ray source placed above the senor+ROC hybrid are seen each of the four ROCs on the sensor module. The data was taken by the self trigger mode using the LVL1 fast OR signal. More than 99 % of the pixels are functional.

Total of 100 sensor modules will be delivered by the end of July 2006, and the remaining sensor modules will be delivered by the end of November 2006. The Q/A tests of the sensor modules will be performed at RIKEN. Recently, VTT has established techniques to replace a bump-bonded ROC from a sensor module. This means, if one of the four ROCs has a large fraction of dead channels due to bad bump-bonding, such a bad ROC can be removed from the sensor modules and replaced by a good one. This will increase yield of the good sensor modules.

Readout Bus

A pixel bus is a printed circuit sandwich made from Kapton and aluminum/copper layers to provide power and control signals for the pixel readout chips, and to bring signals out to a SPRIO module. Connections between the readout chips and the pixel bus are made by wire-bonding. Therefore the metal layers are arranged in vertical steps along the long side of the bus. The structure of the bus and wire bonding of the between the pixel ROC and the pixel bus is illustrated in Figure 49.

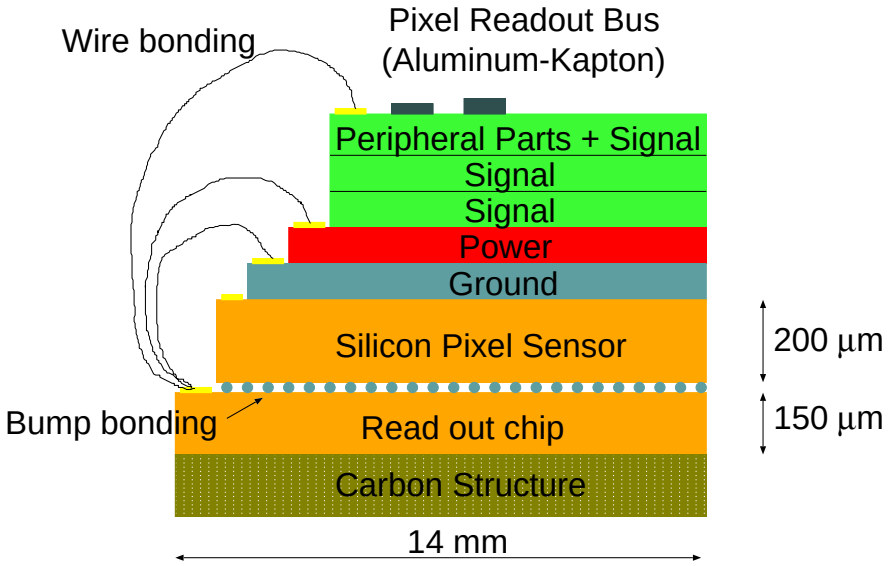

Figure 49 Cross section of a pixel detector half ladder designed for the PHENIX Pixel. The hybrid pixel detector itself consists of a readout chip that is connected via solder bump-bonds to a sensor chip. Every sensor pixel has a corresponding individual signal processing electronic in the readout chip. They are interconnected with small solder balls ("bump-bonds") in a flip-chip process. Eight pixel detector assemblies are wire-bonded to a readout bus structure that runs along the detector on top of the sensors. The half ladder is mounted onto a mechanical stave which includes embedded cooling lines to remove about one Watt of power dissipated by one readout chip.

A pixel bus will be 1.4 cm (3 cm) wide and about 25 cm long, and it carries 190 signal and control lines and a few sensor bias voltage lines. At the end of a pixel bus, a bus extender made by copper/kapton multi-layer flexible PCB is connected to extend the bus lines to a SPIRO module. The connection part of a pixel bus and a copper extender will be 3 cm wide. A copper extender has two high density connectors at the SPIRO side. In the current design, a pixel bus is composed of five metal layers: ground, power, signal lines and a layer for detector bias and auxiliary passive components. A copper extender has double layers for signal, power, and ground lines.

The cross section of the pixel bus is seen in Figure 50. "Horizontal" lines on one of the signal double-layer are running parallel with the long direction of the pixel bus to route the signals to the SPIRO module. "Vertical" lines on the other signal layer are connected to the bond pads on the side of the bus for the wire-bonding to the readout chips. Through-hole connections between the horizontal and vertical lines interconnect the two signal layer components.

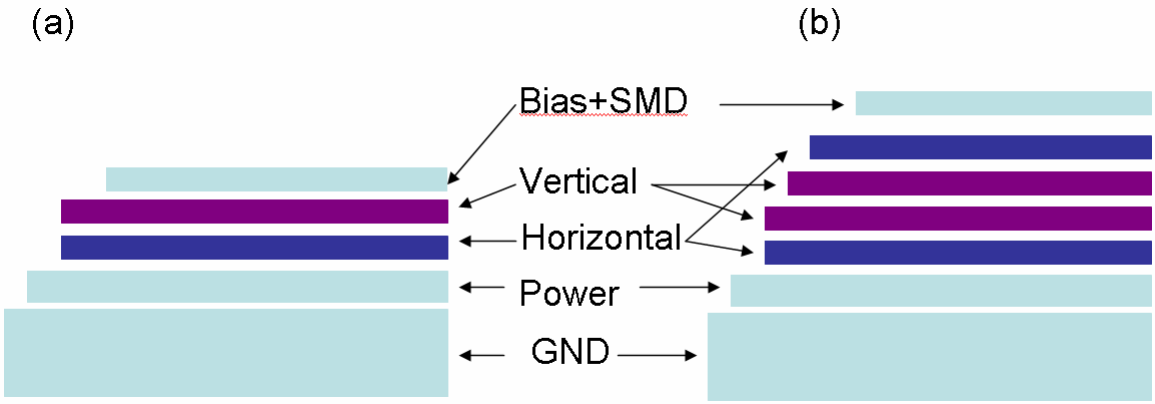

Figure 50 Cross section of the structure of the pixel bus. Two technical solutions are being investigated. Option (a) contains a high-density double-layer of signal lines with a mean line pitch of 70 μm. Option (b) uses a reduced line-density on two signal double-layers with an average line pitch of 140 μm.

Since four ALICE1LHCb chips must be read out in parallel to meet the PHENIX timing requirement, 190 signal and control lines are needed in the horizontal layer, which corresponds to 70 μm line pitch in a single signal layer as seen in Figure 50(a). The capabilities of industrial partners are being explored for a production of such fine pitch aluminum lines. Due to the technical challenge of producing 70 μm pitch aluminum lines, the addition of another signal layer in the pixel bus will be an option. The cross section of the pixel bus made exclusively from aluminum metal layers is seen in Figure 50(b). For this option, the signal line pitch will be 140 μm and the thickness for the pixel bus will be 0.139 % radiation length.

On the other hand, technology to for lines with 60 μm pitch in a copper layer is commercially available. For this reason, a five-layer pixel bus with copper lines for the horizontal and vertical layers, and other lines made from aluminum is our current technology choice. The material budget of this option is 0.236 % radiation length. To make a further reduction of the material budget possible, the effort to produce a pixel bus with exclusively aluminum lines will be continued.

We employ this new strategy to use thinner copper for signal lines. The 3 μm thickness copper foil on the kapton sheet is available in the market. Its radiation length is equivalent to the 18 μm aluminum. This copper foil is much easier for pattern etching by using well established technology. Figure 51 shows etching pattern with 3 μm thickness copper.

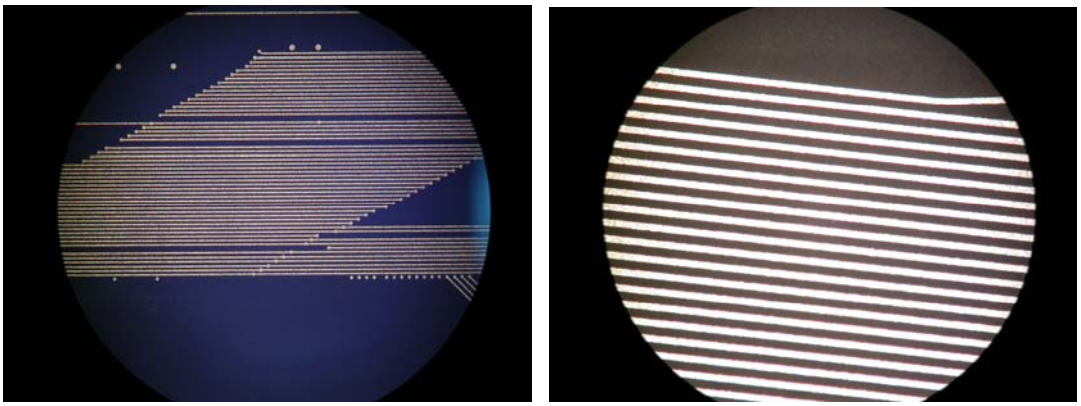

Figure 51 Fine pitch patters with 3 μm thickness copper foil. The test pattern is 70 μm pitches, which is requires for 190 lines of PHENIX pixel bus.

We designed and manufactured the 3cm wide pixel bus and associated copper extender by using 12 μm thicknesses copper for electronics readout test. TheFigure 52 the pixel bus picture, which has 3 signal layers and ground and power plane. The Figure 53 is a picture of the copper extender which connects the pixel bus and SPIRO board. The pixel bus and the copper extender is connected by the wire bonding, and the copper extender is connected by the fine pitch connector. The copper extender has 2 layers.

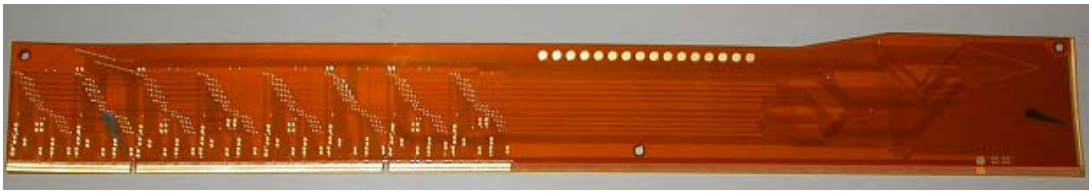

Figure 52 A prototype pixel bus for electrical readout test. The size is 3 cm wide and 25 cm long.

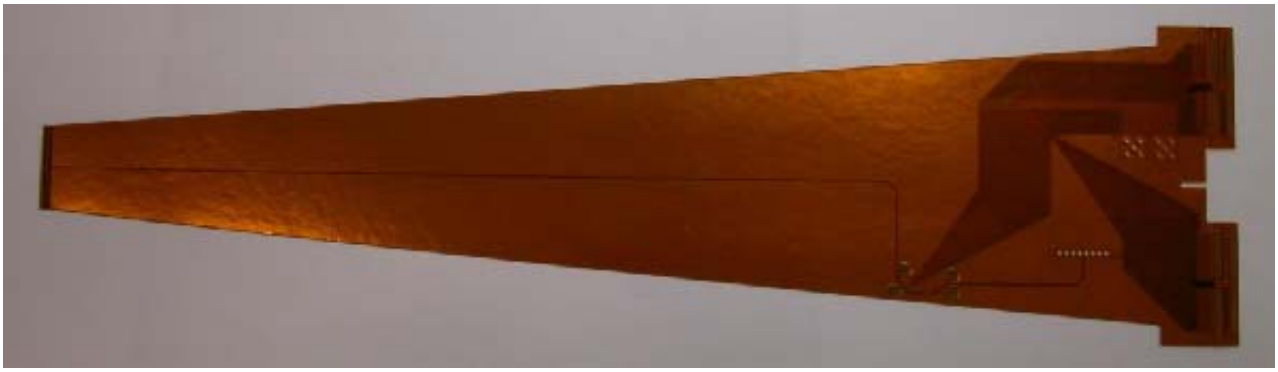

Figure 53 A copper extender connecting a pixel bus and SPIRO board. The width is 3cm wide at the pixel bus side and 14 cm wide at the SPIRO side. The length is 45 cm.

Silicon Pixel Interface Read Out (SPIRO)

The SPIRO board will have the following functions:

- Sending control information to pixel ladders at their operational frequency of 10MHz,
- Serializing data from ladders and sending to FEM boards over optical links at 1.6Gbps,
- Frequency matching between the PHENIX global clock and the high speed G-Link,
- Data format conversion (replacing redundant fast-or fields by parity fields) to match PHENIX requirement.

The major challenges in the construction are:

- Long term reliability in high radiation environment,
- Small size: current space available for SPIRO board is 12cmx16cmx2cm.

The key component on the SPIRO boards is the digital pilot ASIC. Upon pixel chip readout being initialized, each pixel chip presents 256 sequential words of data on a 32-bit bus synchronously at a 10MHz clock. Thus, 25.6μs is required to read the data from a single chip. In the PHENIX data acquisition system, the readout is ultimately performed in 40μs to achieve a maximum throughput of 25 kHz. A sequential readout of the eight chips on a half ladder requires 204.8μs to empty the pixel chip data into the pilot, and hence does not meet our timing constraints. To satisfy the readout time requirement of PHENIX, we must readout four pixel chips in parallel, thus 4×32-bit data will be transmitted to the SPIRO board.

The solution adopted for the first SPIRO prototype is based on a new digital pilot ASIC developed by the RIKEN group. This ASIC option uses the same design rules and radiation tolerant technology as the ALICE pixel pilot ASIC that is presently already functional. It can handle 2x32 bit inputs which allows the simultaneous reading of two pixel chip words by one pilot ASIC. Each 32 bit input handles output from a pair of chips, which represent 512 sequential words of pixel data. Thus, two digital pilot ASICs are required to read data from eight chips. This architecture reduces to 51.2μs the total time needed to empty the pixel chip data coming from a half ladder, but requires twice as much space as the present design of the ALICE pixel Pilot module, and twice the number of optical fibers. The first version of the modified digital Pilot chip

(PHENIX digital pilot v1) was submitted as part of a multi project wafer at CERN to IBM in May 2004. Delivery was made in September 2004

The data transmission from the readout chip to the pilot chip is performed in the following way. The bus carries two times 32 bits with a frequency of 10 MHz to the Pilot chip. The Pilot chip is designed to output at 40 MHz. This means that four 25 ns transmission cycles are available before the next data word from the readout chips arrives. The first two clock cycles are referred to as "cycle-0" and the last two clock cycles as "cycle-1". If no pixel data readout is performed, only control data which includes the fast-OR signals is transmitted in the cycle-0. The fast-OR signal can be used to generate a LVL1 trigger, which is discussed in section 3.5. These data are referred to as slot-0. In this case cycle-1 contains only empty data. During pixel data readout, after transmission of the data of slot-0, event header information (slot-1a) is transmitted in cycle-1. This is followed by repeated slot-0 and slot-1b which contain the pixel hit information. The principle of the data transmission is illustrated in Figure 54.

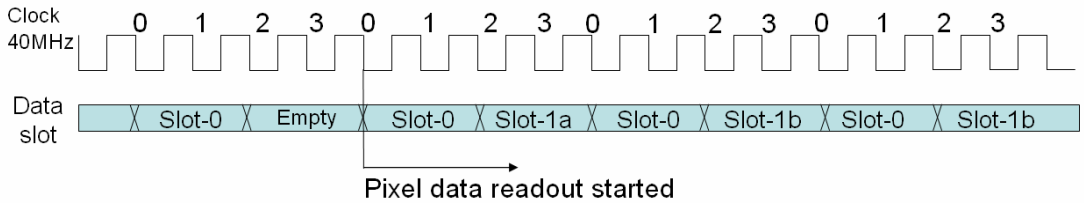

Figure 54 Illustration of the data transmission from the pixel detector.

The first SPIRO prototype based on this version of the pilot chip was designed by the Ecole Polytechnique group and sent to fabrication in October 2005. Six boards were received in December 2005. In this prototype, the data format conversion (replacement of redundant fast-or fields by parity fields) and protocol change (from CIMT to 8b/10b) is implemented in the FPGA. In order to keep the possibility of a final version of a SPIRO board with no FPGA, another version of the digital pilot chip (PHENIX digital pilot v2) was submitted in May 2005, in parallel with the work on the first SPIRO prototype. This new version of the chip in which the data format conversion is implemented was delivered in March 2006.

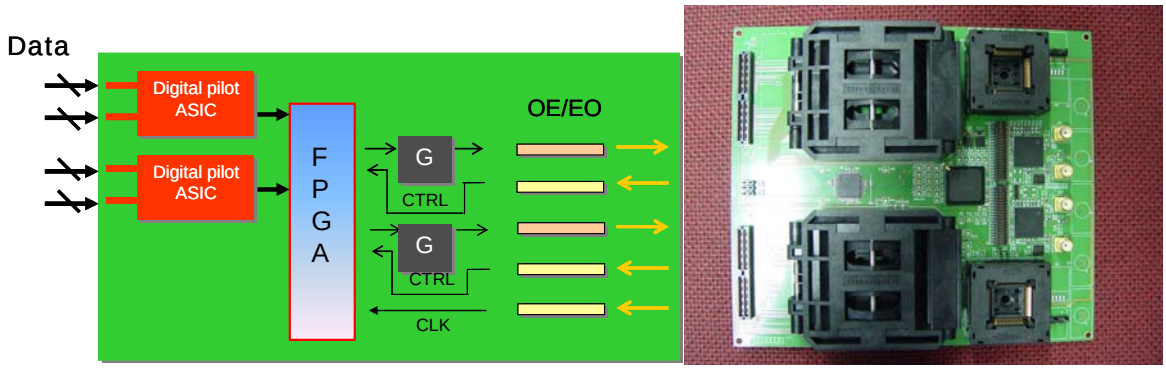

Figure 55 Left : Layout of SPIRO prototype. Right: A SPIRO prototype

However, during the debugging phase of the first SPIRO prototype, it was realized that one critical function of the FPGA will be to implement a FIFO. This will make a clock domain interface between the PHENIX global clock and the high speed link clock, the latter of which uses a local clock source to satisfy the tighter jitter tolerance. More specifically, the serialization is done by a GOL chip which is a CERN solution capable of serializing up to 32bit data input at 40MHz and driving high speed links at a frequency of 1.6Gps (cf Figure 56 for a typical output reading from SPIRO on oscilloscope). This chip works with 40MHz input clock with a peak to peak jitter of less than 100ps to produce the high speed output at an acceptable jitter level. A quartz crystal implanted on SPIRO generates the 40MHz clock to feed the GOL chip with the required jitter specifications; whereas the digital pilot chip will work on the PHENIX clock with a completely different jitter.

Figure 56 SPIRO send Control (Dx.x) + Carrier Extend (K23.7)

It is unlikely that another solution be found to this problem, which implies that an FPGA will probably be necessary in the final version of SPIRO. The development of a second prototype which must be as close as possible to the final production version will start as soon as the following questions are answered:

- Choice between PHENIX pilot chip v1 and PHENIX pilot chip v2,
- How much radiation dose is expected at the location of SPIRO,
- What level of radiation hardness is needed for the FPGA,
- Final mechanical design.

Front End Modules

The SPIRO modules transmit their data via optical fibers. A Front-End Module (FEM) will communicate with two or more SPIRO boards on one side, and the PHENIX DAQ and slow control system on the other side. Since the SPIRO module transmits the data via optical fiber, the FEM can be located in electronic racks away from the vertex region. Each FEM may receive data from several pixel half ladders and thus reduce the number of Data Collection Modules (DCM) needed to interface to the PHENIX DAQ. In order to allow simple manipulations of the data, the FEM will pipe the data through an FPGA. This FPGA will add data headers and trailers to for standard PHENIX data packages. The design of the FEM is very similar to FEM's that are currently employed in the PHENIX readout system.

The development of the FEM for the pixel readout proceeds in three stages. The first stage was a proof of principle test to readout a pixel chip into the PHENIX DAQ system.
Next a full scale FEM prototype was developed with the goal to readout several pixel half ladders in a cosmic ray test as well as in an in-situ test of the pixel ladders in the PHENIX experimental area. In the last stage the final FEM will be designed and a preproduction version will be fabricated. At this point in time the first stage is complete, a prototype has been successfully tested with a SPIRO board and cosmic ray tests with pixel ladders are immanent.

For the proof of principle test we obtained a functional pixel chip mounted on a test board and a pilot module, the NA60 version of the SPIRO module, from NA60 through our close collaboration with them. A transition board, designed in the context of a Masters Thesis at Stony Brook, received the data from the

NA60 pilot module and pipelined it through an FPGA to a drift chamber FEM with appropriately modified firmware. The FPGA on the transition board holds all functionality needed for the PHENIX pixel FEM and was designed to serve as basic building block for future FEM developments. Through a USB port the transition board is fully programmable and the NA60 chain can be controlled and readout directly from a PC independent of the PHENIX DAQ. All necessary slow control software for the pilot module and pixel chip was implemented in a visual BASIC interface. The setup allowed establishing a proof of principle that the pixel chip can be readout into the PHENIX DAQ and that in turn the pixel chips and the pilot chip – core of the pilot module – can be controlled through a PHENIX FEM.

Following the success of the proof of principle test a full scale prototype FEM was developed. A schematic view of the prototype FEM is shown in Fig.x and Fig.xx presents a photograph of a fully equipped prototype. The FEM combines the features of the earlier transition board with those of the drift chamber FEM and adds the IO necessary to communicate with SPIRO boards. It is designed to readout and control 2 or 4 SPIRO boards, either two 2 half-ladders or 4 sensor-readout chip assemblies, from a PHENIX DAQ system. Data from one SPIRO board are received via two 1.6 Gbps optical links and the FEM provides the RHIC clock and serial data link to control the SPIRO board and the pixel readout chips. After reformatting the data as it passes through the processor unit the data are send to a PHENIX DCM via a GLINK optical fiber connection. The clock and control signals are received from a PHENIX GTM, again via a GLINK optical fiber connection. The GLINK connection is provided through plug-in modules developed for the used in the drift chamber FEM's and other PHENIX subsystems.

For debugging and development purposes the FEM and with it the SPIRO boards and pixel ladders may also be controlled and readout via a USB connection. This connection and all necessary software have proven very useful during the proof of principle test and will become an integral functionality of the final FEM. In addition the prototype FEM can also control and read the NA60 readout chain; this was particularly useful during initial tests of the prototype.

A total of 5 FEM's have been manufactured of which one was modified to function as 1.6 GBit FEM data source. At this point in time the FEM has been tested with the NA60 readout chain including a pixel chip. Recently first chain tests could be performed with a SPIRO board receiving data from the FEM data source. During these test the functionality of the chain could be verified and in particular stable data transfer through the 1.6 Gbps optical link was

demonstrated. A full chain test with a first prototype ladder of readout chips, prototype SPIRO board and prototype FEM are ongoing and will lead towards tests of several ladders with cosmic rays the next one or two months.

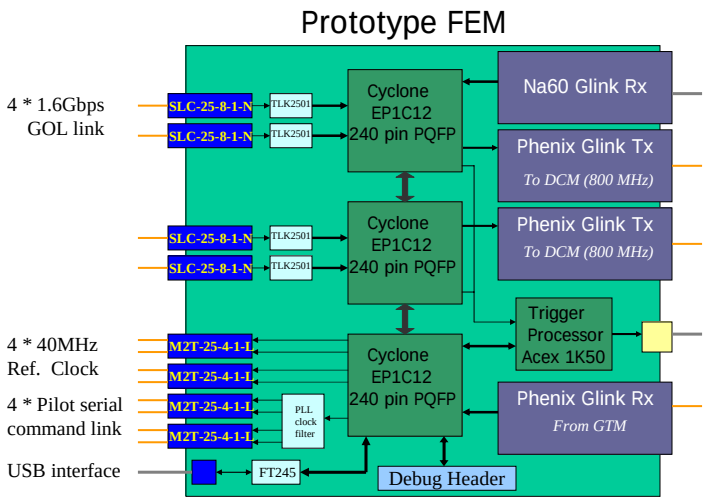

Figure 57 Schematic layout of the pixel FEM prototype. IO units are shown in dark blue, processing units, implemented as FPGA's, in green.

Figure 58 Prototype FEM for pixel detector

Pixel Ladder Assembly

Two half ladders are mounted on a mechanical stave to form a full pixel ladder. The goal of the pixel ladder assembly procedure is to insure that the sensors are accurately located on the mechanical stave with respect to its alignment

pins. This will allow manual placement of the ladders on the structural assembly.

For the silicon pixel detectors the major steps that need to be taken are,

- Q/A of sensor modules which include one sensor and 4 ROCs. This is on going at RIKEN using a probe station.
- Q/A of the readout bus.
- Assemble half ladders, combining readout bus and two sensor modules. This is the most critical mechanical operation in assembling the pixel detector. The sensors must be attached to the ladder within an accuracy of <10 μm.

A ladder can be separated 3 components, (i) two pixel buses (ii) 4 sensor modules, and (iii) a mechanical stave which is made of Carbon/Carbon(C/C) thermal plate, a omega structural piece, and cooling tubes. These components will be glued by two component epoxy paste adhesive, Araldite AW106/HV953U, which is known as radiation hard adhesive and is used in high energy physics experiments.

The pixel sensor adopts binary readout method. General intrinsic resolution of a binary sensor is known as $L/\sqrt{12}$, where L is the size of a pixel. Since the pixel size of our pixel sensor is 50 μm, its r.m.s. resolution is about ~15μm. This means that we must assemble the detector within this resolution. In order to minimize the effort needed in the offline alignment by using real tracks, a precise alignment of the ladder assembly itself is required. After taking into account for a safety margin, we determined that 10μm as the goal of the assembly precision.

The fabrication method of a pixel ladder with high assembly precision and stable quality control should be established before the production of ladders starts. Especially, we have considered how to align 4 sensor modules on a mechanical stave very accurately. A challenge here is that there is no reliable alignment mark on the sensor module except for bonding pads on the ROCs. We can't use the edge of sensor module because dicing position is different about ~40μm from one sensor to the other. Our solution is to use the wire bonding pads of the ROCs as an alignment marks because they have enough position precision relative to the pixel sensor matrix. We need the specific jigs equipped with high magnification microscope, precise moving stage with gauge, vacuum chucking mechanism to the sensor module, glue dispenser robot. We had been consulted with an engineering company to design and manufacture the assembly jigs for the pixel ladders, and the company recently has produced

the jigs shown in Figure 59. We'll start the test to assemble for ladder with actual procedures in production phase.

Figure 59 shows the assembly jig which aligns the sensor module to be put along a straight line. The jig has the microscope and precise X-Y-θ stage with vacuum chucking and linear motion (LM) rails with high accuracy running parallelism < 10μm/m. The sensor module is chucked by the stage and moved to proper position while seeing the pad through the microscope, one by one. Figure 60 shows to be aligned sensor module's position. The Δx, a space between sensor modules in Figure 59, is observed as μm order by the magnetmeter equipped with LM rails. The precision of the space is permitted within the Δx < 50μm at least in Figure 60, the Δy, a offset between sensor modules, is observed to run the stage along the LM rails with the microscope. Aligned sensor modules will be checked by 3D vision measuring machine and confirmed to be aligned permissible range before gluing.

4 sensor modules after alignment are glued with C/C support. The glue, Araldite AW106/HV953U, has a coefficient thermal conductivity (CTC, 0.22W/mK) and is dispensed uniformly by programmable automatic dispenser robot. Each base laid on aligned sensor modules and support has the linear bush and linear bush pin, respectively. The gluing is put two bases together. The glued position of sensor modules and support is determined by the residual of the bush and pin's radius, which is typically ~5μm level. The assembly of cooling pipe is under investigation but the procedure is almost as same as the procedure of gluing between sensor and support.

The bus is also glued on the top of the sensor modules. The gluing procedure is basically as same as the support. The bus has the several alignment holes. The position accuracy for gluing the bus is determined by the manufacturing precision of the holes. The precision is 50μm. Although the accuracy is enough to perform wire bonding between sensor modules and bus.

These ladder components are made of various materials. So we have to care for the properties, thermal conductivity, thermal expansion and Young's modulus and to absorb the difference to keep the temperature of assembly room at 24±1 degrees. The manufacturing the prototype for half-ladder in addition to the preparation of jigs for production phase have been proceeding simultaneously. At last, we had achieved to get a first prototype half-ladder in December 2005 at assembled Japan shown in Figure 61. We possess three half-ladders until today.

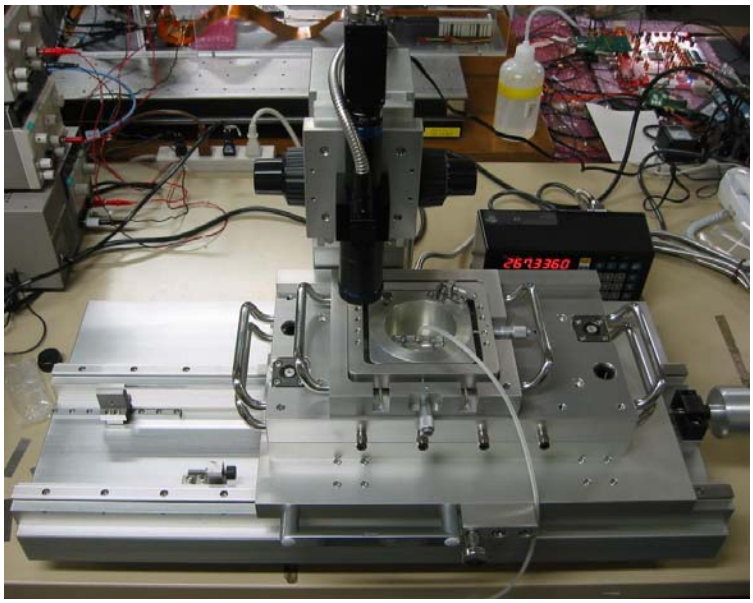

Figure 59 Assembly jigs for ladder delivered in RIKEN, Japan.

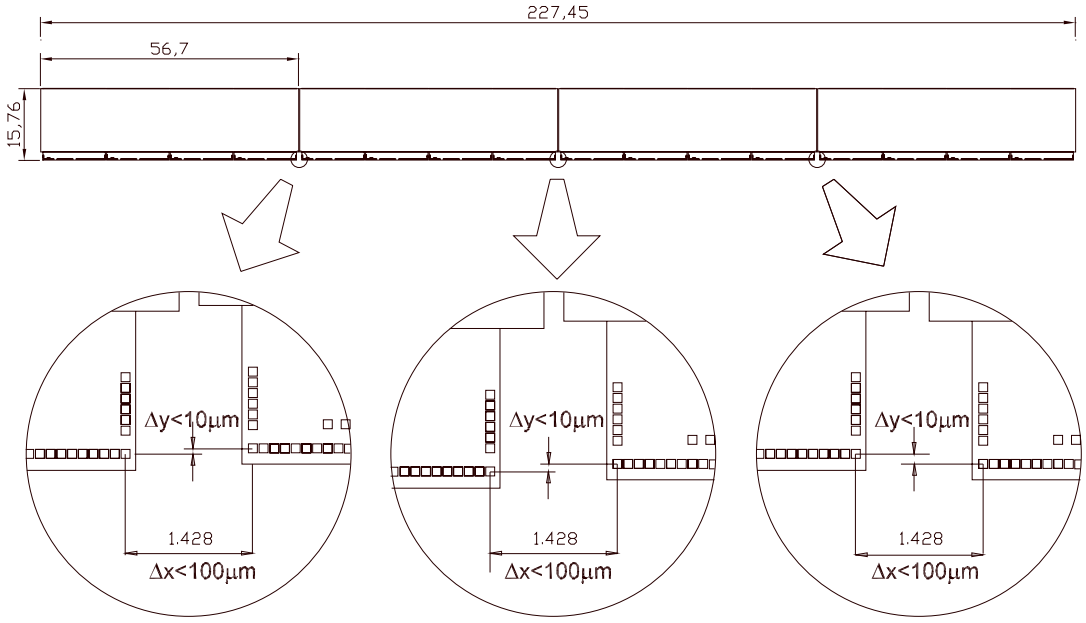

Figure 60 Position of sensor modules to be align in a ladder.

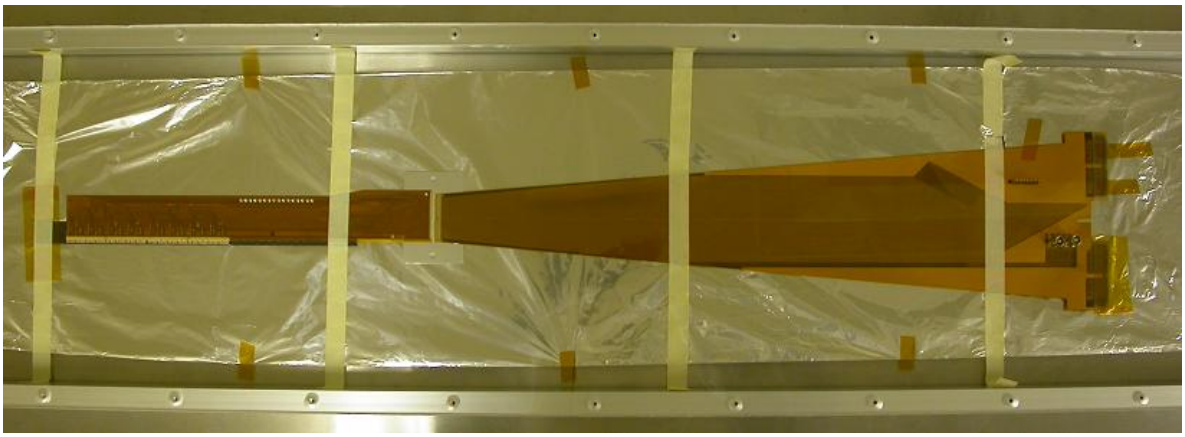

Figure 61 Assembled prototype half-ladder.

4.3 Silicon Strip Detector

We plan to instrument the outer two barrels of the silicon vertex tracking (VTX) with silicon strip detectors of a novel design sensors. The sensor design was developed by the Instrumentation Division at BNL & provides two-dimensional position sensitivity with single-sided processing. A first set of prototypes was produced and tested using the VA2 readout chip. After the test of the first generation sensor, the second generation sensor prototype was developed correcting of the charge sharing asymmetry problem observed in the first prototype generation. The second generation prototypes are being readout by SVX4 chips, which were developed for silicon strip detectors by FNAL and LBL. The pre-production sensors were produced by Hammamatsu (HPK) in 2005. In the final readout system the SVX4 chips would be arranged on readout cards (ROC's) and mounted directly on the sensors. The ROC's would also provide the data bus, power distribution, and all necessary control signals.

Principle Design

The novel strip concept is shown on Figure 1. The sensor is n-type single sided Silicon developed at BNL. For clarity, Figure 2 shows a schematic view of the p+ cathode structure of the strip-pixel sensor. Each sensor is a finely segmented detector with 80μm×1000μm pixels. Each pixel region has two serpentine-shaped metal strip that collect charge produced by an ionizing particle that traverses the silicon. A hit by an ionizing particle will deposit charge on two serpentines. A metal strip connects those serpentines that are in a straight line (*X*-direction), while a second strip connects serpentines that are at a 4.6 degree angle (*U*-direction). This provides a stereoscopic *X*-*U* readout and thus two-dimensional information from one side of the sensor.

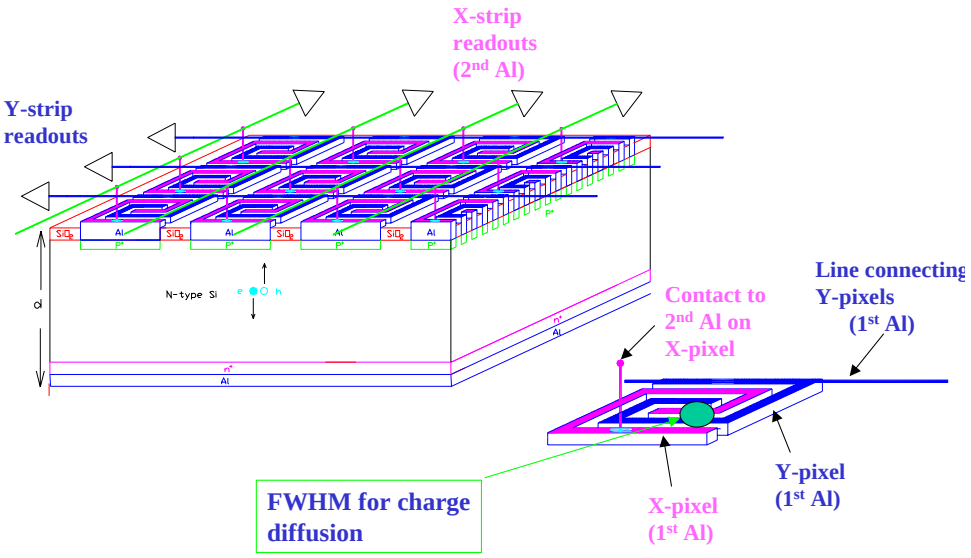

Figure 62 The strip detector concept with interleaved spiral shaped X and Y sub-pixels.

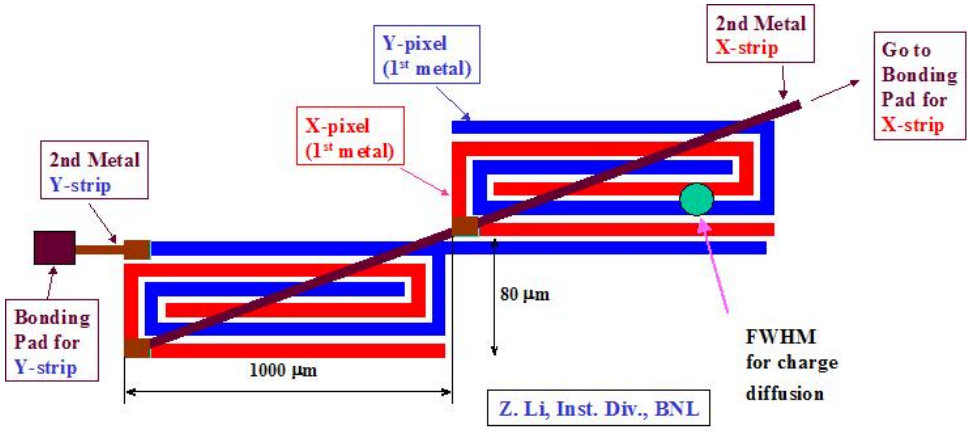

Figure 63 A schematic view of p+ cathode structure of the strip-pixel sensor.

First Prototype Strip Sensors fabrication runs at BNL:

Figure 63 shows a schematic view of the first prototype strip sensors and their geometrical dimensions. Detectors were made on 100 mm diameter n-type Si wafers, with a resistivity of 4-6 kΩ-cm. The thickness of these wafers were 250 µm and 400 µm, and they were processed at BNL. The sensor size is 3 cm x 6 cm, and the detector is divided into two identical halves. In the left half, there are 384 Y strips with 80 µm pitch and bonding pads for readout on the left side; and there are 384 U (or X) strips with 80 µm pitch and bonding pads for readout in the middle of the wafer. The stereo

angle between Y and U strips is about 4.6°. The right half is a mirror copy of the left one with respect to the middle line of the sensor.

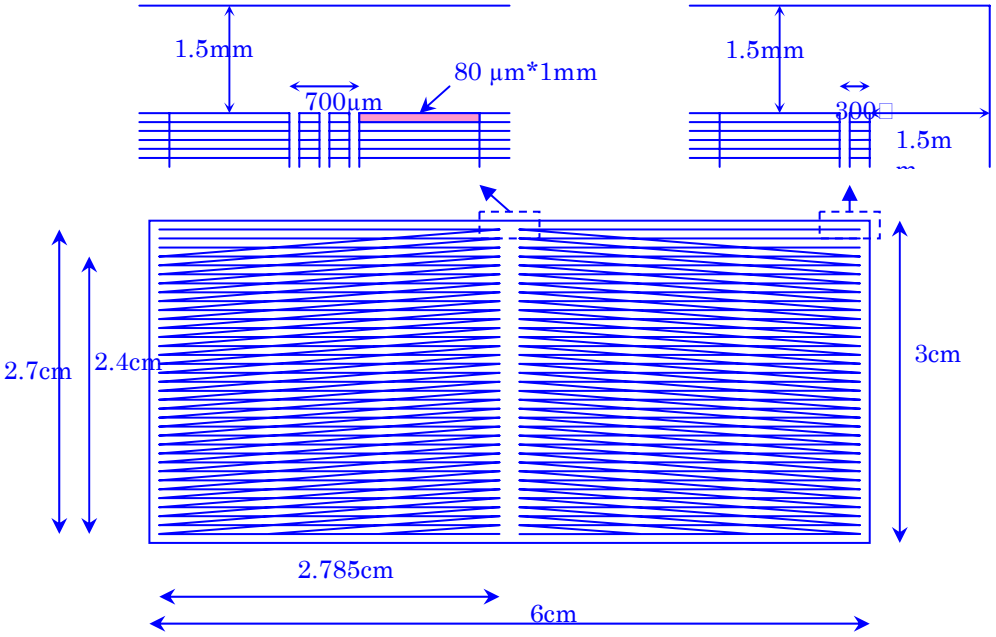

Figure 64 A schematic of the sensor layout of the first prototype Si stripixel sensor.

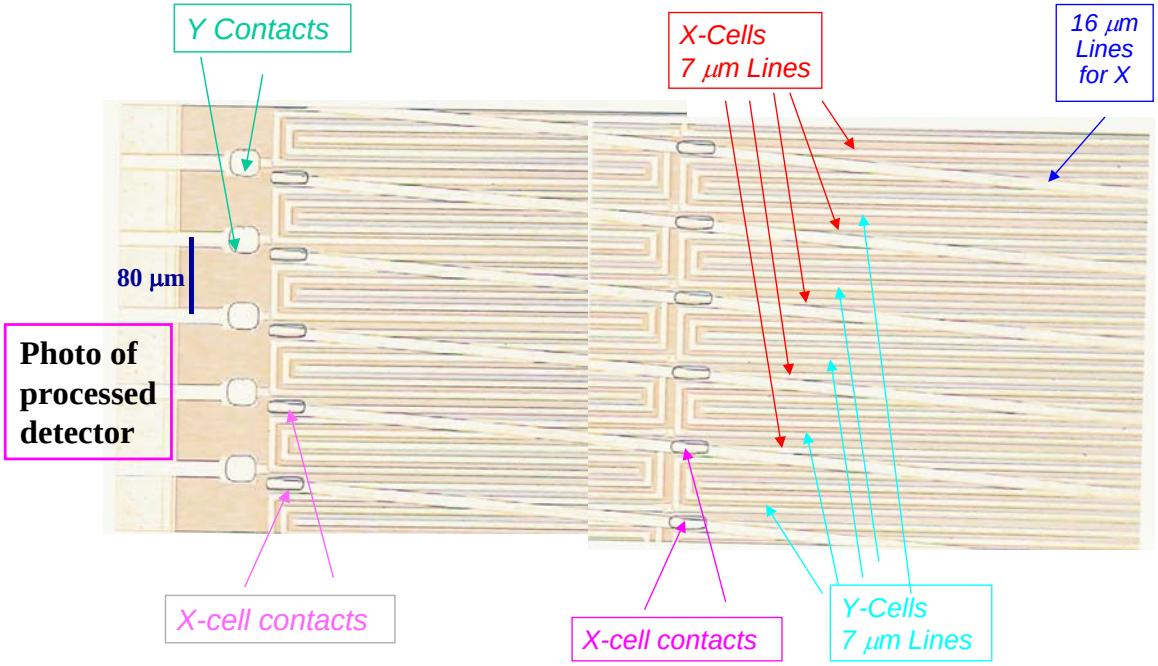

Figure 65 Photograph of the first batch prototype strip sensor: Y strips and X(U) strips are shown.

Shown in Figure 65 is the photograph of a Si stripixel detector in the first prototype batch. Y strips are routed out to the left to bonding pads (not shown), and U strips are clearly seen with a small angle (4.6°) with respect to the horizontal. The contact vias to X sub-pixels (X-cells in the figure) are also visible.

These detectors have been tested in the laboratory and in beam. The second generation of prototypes with 400 and 500 μm thickness have been developed with success and the preproduction has been started at Hamamatsu in 2005.

Laboratory tests of the first prototype strip sensors

The initial tests of the prototype sensors have shown good results. Figure 66 shows the measured current and capacitance as a function of the bias voltage. Full depletion is achieved at a bias voltage of around 80 V. At this voltage the capacitance of each strip is ~10 pF and the leakage current is less than 10 nA.

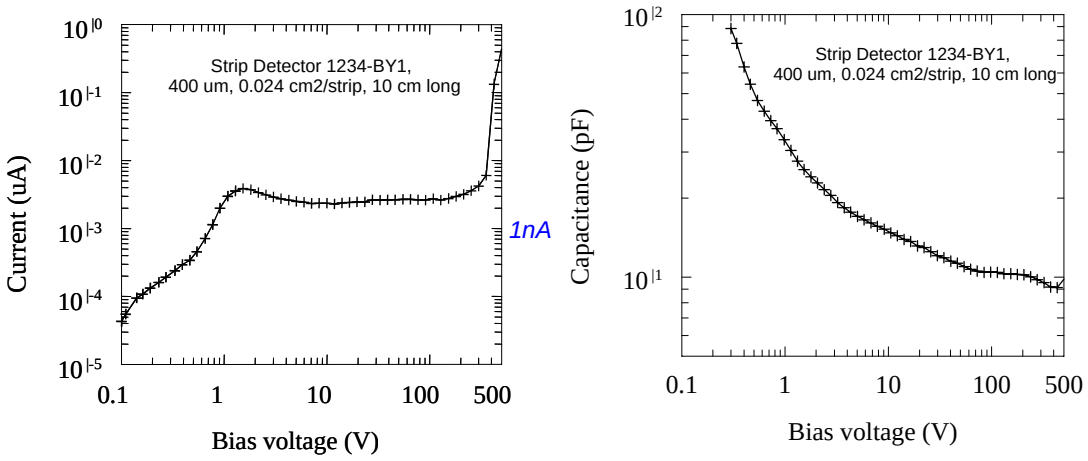

Figure 66 Current and capacity characteristics of a prototype sensor.

To test the sensors in more detail, the Instrumentation Division in BNL has constructed a laser test setup. During the R&D phase the laser setup allows to studies of the properties of the sensors and to find the optimum operation condition, which includes the depletion voltage, the charge collection efficiency, the response to the carrier drift process, electric field profile inside the sensor and so on. The transient current technique (TCT)[50] [1] is applied to obtain the electrical properties of the sensors. The technique is based on the analysis of the current and/or charge pulse shapes, which arise from electron-hole pairs created inside the detector by injecting the fast laser light. During the mass

production of sensors, the existing setup or a newly developed setup based on our experience will provide the basic tool for quality control of the strip sensors and later of the assembled detector ladders.

Figure 67 shows the schematic layout of the laser test setup. The picture of the laser test setup is shown in Figure 68. A nano-second pulsed laser coupled into a focuser through an optical fiber is operated with a pulse generator. Two types of laser are used in the laser tests.

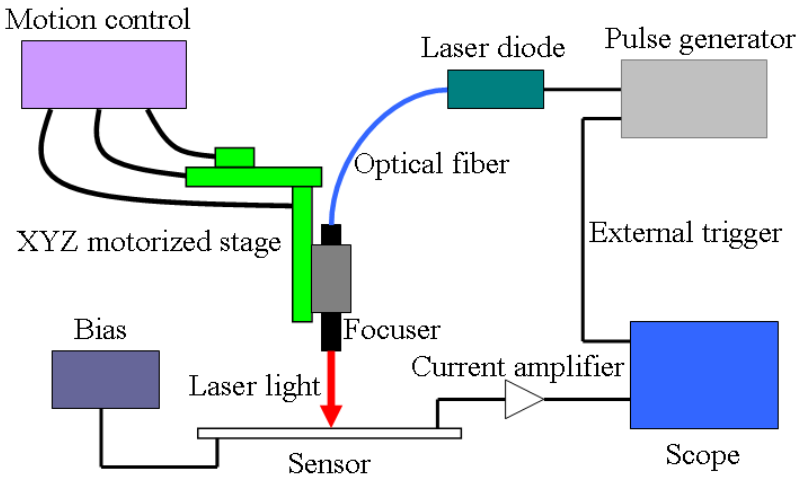

Figure 67 A Schematic layout of the laser test setup.

One is a red laser with the wavelength of 635 nm and the penetration depth of 3 μm in silicon, and the other is an infrared laser with the wavelength of 1060 nm and the penetration depth of 800m in silicon. The red laser is used to study the separate collection of electrons and holes. The infrared laser is used to study the response of the detector to the charge deposition of a minimum ionizing particle (MIP). The focuser was fixed to a *XYZ* motorized stage. The precision of the laser spot positioning with the motorized stage is 0.5m. The laser spot size achieved after focusing is about 10μm in diameter. The current laser test setup is controlled with manual controllers and will be upgraded to have an automatic control with a LabVIEW compatible multi-axis motor drive.

Figure 68 A laser test setup for the strip sensor.

Beam test of the first generation sensor proto-type

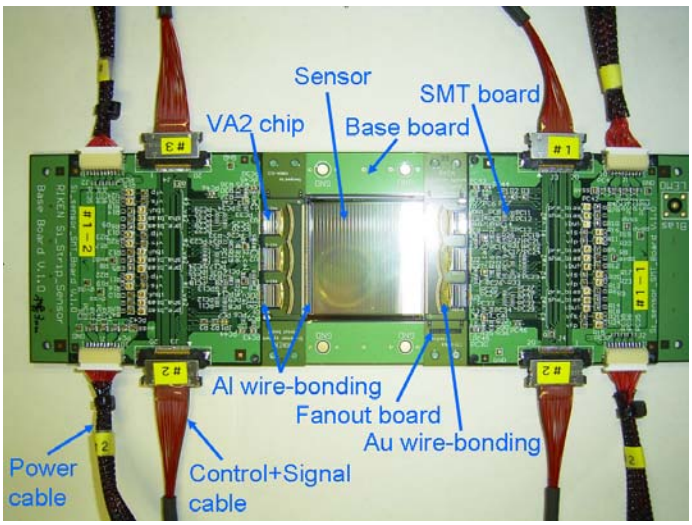

Figure 69 A first prototype detector using the first prototype sensor.

The first generation prototypes sensors were tested using test beam at KEK. To test the prototypes in beam, the sensors were mounted on readout cards designed to read out signals from one side of the sensors (see Figure 69). Each plane consists of a silicon strip sensor, six readout chips, a base-board, two fan out boards (pitch adaptors) and two SMT boards. A bias voltage was applied in the sensor backplane (ohmic side) through the base-board. An analog

multiplexer readout chip with 128-channel charge sensitive preamplifier-shaper circuits, VA2 chip of Ideas ASA[51], was used to read out signals from the sensor. The preamplifier-shaper has a 1-3 μsec peaking time and a nominal gain of 30 mV/pC. The SMT board was designed to operate the VA2 chips and read out multiplexed analog signals through an interface with a VME data acquisition system. Three detectors planes with 400 μm thick sensors and four with 250 μm thick sensors were constructed. The sensor performance in terms of charge sharing properties, detection efficiency and position resolution has been evaluated with a ^{90}Sr β-source and in the test beam at KEK. The beam test was performed at T1 beam line in KEK-PS, which delivered a positively charged particle beam with momentum of 0.5 - 2.0 GeV/*c*.

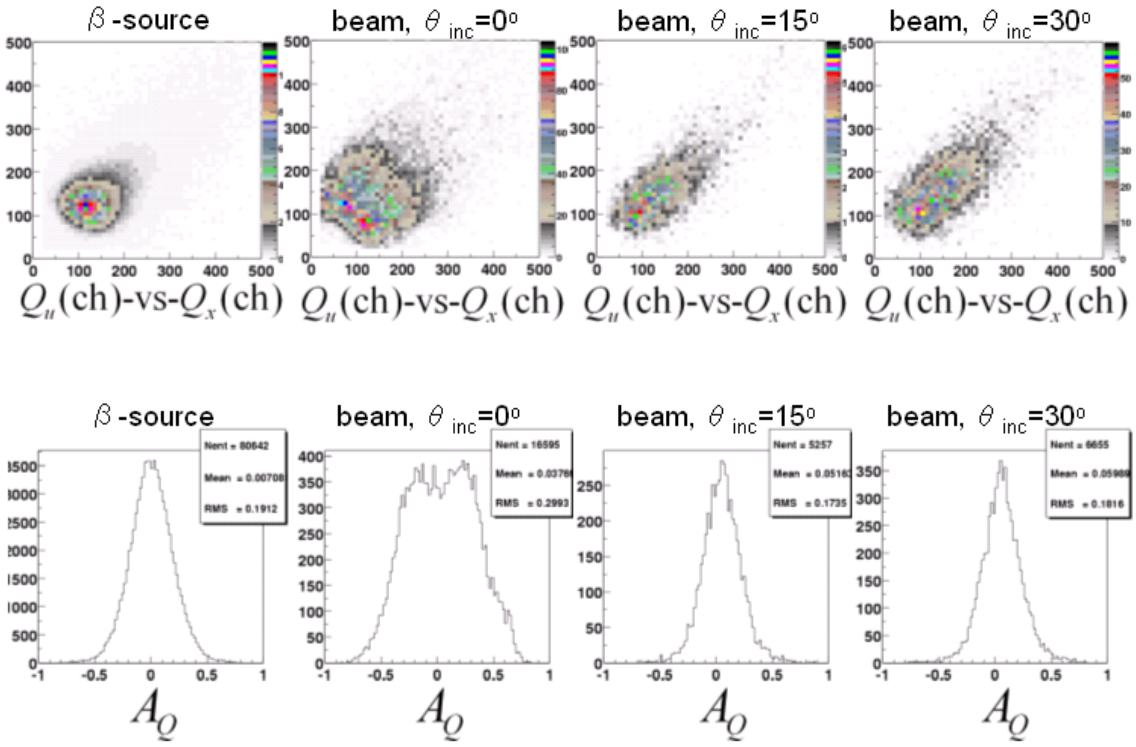

Figure 70 Charge correlations in between x-strips and u-strips found in tests with a radioactive source and with beams of charged particles.

Charge sharing property in x-strip and u-strip can be characterized by the asymmetry, $A_Q = (Q_x - Q_u) / (Q_x + Q_u)$, where Q_x and Q_u represent collected charges in *X*-strip and in *U*-strip, respectively. For optimum two-dimensional position sensitivity, one expects that A_Q on average is zero with a narrow width. The results of the A_Q measurements are plotted in Figure 70. The source test shows the A_Q distribution peaking at zero with a width of about 0.18. This

demonstrates that the principle of two-dimensional position sensitivity by charge sharing works. In the beam tests A_Q exhibited a dependence on the incident angle of the beam normal to the sensor surface, θ_{inc}. For θ_{inc} = 15 degrees and 30 degrees narrow distribution with a peak at zero were observed. However, at θ_{inc} = 0 degrees broad distributions which did not peak at zero were found. This deficiency was traced back to the line width (8μm) and gap spacing (5μm) of the *p+* electrode structure in a single pixel. The line width is too wide compared with the size of charge diffusion, and therefore the charge sharing ratio of the *X* and the *U* strips depends on the position of the hit. For the second-generation prototype sensors a narrower line width (5μm) and gap spacing (3μm) was chosen to overcome this problem.

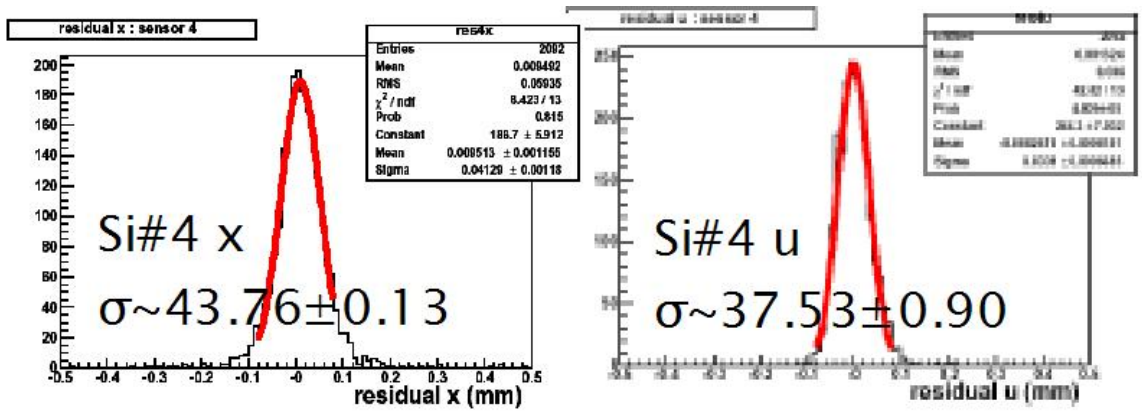

Figure 71 Hit residuals from tracks found using the silicon strip sensors in a test beam experiment.

The position resolution was measured from the residuals of hits on reconstructed particle trajectories. As is shown in Figure 71 the r.m.s. width of the residual distribution for a single strip is about 40 μm. After de-convoluting the fit bias and the contribution of multiple scattering, the intrinsic position resolution of the detector is 23 - 25 μm. This is consistent with the expected resolution for a strip detector of 80 μm pitch ($80/\sqrt{12}$ =23.1).

In this beam test, a reliable measurement of the efficiency of the sensors was not possible. In part this is due to the imperfections in the charge sharing, but more prominently the readout chain suffered from a severe common mode noise, which leads to a less than expected signal-to-noise ratio. This prohibited an efficient hit detection. At present only the lower limits for the efficiency can be quoted. They are 98%, 96%, and 88% for three 400 μm thick sensors.

The low efficiency, 88%, for one of the three test sensor can be attributed to electronic noise at the beam test. A similar study for the second generation sensors was explored. The detection efficiencies and the signal-to-noise ratios was found to be improved by optimizing the operational condition of the detector and by introducing a more appropriate readout chain based on the SVX4 chip

The Second Prototype Sensor and Tests with SVX4 Readout Chip

To correct this charged sharing asymmetry problem observed in the first prototype sensors, a second prototype sensor was designed to have 5 μm line width and 3 μm gap spacing of the p^+ electrode structure in a single pixel. The sensor is expected to have better charge-sharing property, compared with the first prototype sensor with 8 μm line width and 5 μm gap spacing. The second prototype sensor has been processed by the BNL Instrumentation Division. Four sensors with 400 μm and four with 500 μm thickness were fabricated by the end of January 2004 and the middle of May 2004, respectively.

Detectors composed of the second prototype sensors and the electronics hybrids with the SVX4 readout chips were constructed. The study of the signal-to-noise ratio in the detector is essential for the strip detector development and have shown a better than 20:1 S/N using HPK preproduction sensors. The design of the detector is similar to the first prototype detector shown in Figure 69. The VA2 chips and the SMT board in the first prototype detector have been replaced with the electronics hybrid shown in Figure 81, which is developed for CDF Run-IIb Silicon Detector. Three of the four SVX4 chips mounted on the hybrid are used to readout 384 *X*- or *U*-strips of the sensor. One hybrid received from the CDF collaboration is used for the detector. The hybrid is operated by using a test board, which is a simplified version of the PHENIX DAQ.

New Sensor Design

We have developed an improved design of the stripixel sensor, which matches the strip ladder detector design including the ROC described below. Major changes compared with the 1st and 2nd prototypes are :
1) Readout pads are located in the longer-edge of the sensor to make a room for RCC in the center of the sensor and for bus connections between ROCs. This change can be done in the 2nd aluminum layer.
2) Dead space of the 30 *U*-strips in the upper-side in Figure 64 is eliminated by connecting those *U*-strips to the *U*-strips in the lower-side in Figure 64. This change also can be done in the 2nd aluminum layer.

3) Dead space in the middle of the sensor is eliminated.
4) Aluminum lines connected to the inner guard ring are added around the readout pads to make the sensor tests easier.

The modified design developed with Hamamatsu in Figure 72. The stripixel structure of 80 µm × 1000 µm pixel with 5 µm width and 3 µm gap p+ line was kept.

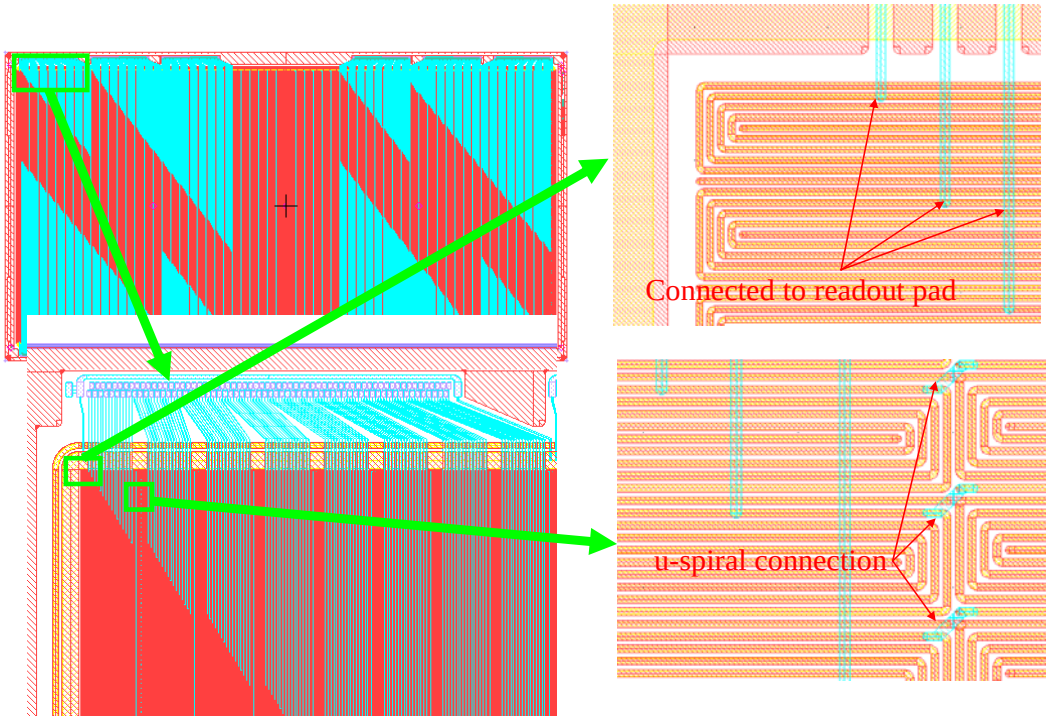

Figure 72 Design layout of the HPK preproduction batch of Si stripixel sensor.

The production of sensors with this improved design was done by Hamamatsu as a part of the preproduction process described below. The new sensor of the preproduction was delivered in 2005.

Sensor pre-production from Hamamatsu (HPK)

In 2005, the stripixel technology developed silicon strip sensors, including the mask design and processing technology, has been transferred successfully from BNL to the detector fabrication industry, the Hamamatsu Photonics, Japan (HPK), for mass production. By the middle of 2005, HPK has produced a pre-production batch of Si stripixel detectors on 6" diameter wafers with thickness of 625 µm, and resistivity > 10 k Ω-cm. As shown in Figure 11, for ease of readout electronics arrangements, the bonding pads for both Y and U strips are moved to the top and bottom of the sensor, with readout routing lines

perpendicular to the strips. This routing arrangement, however, does not require an additional metal layer in the processing, i.e. it is still a double-metal process. Shown in Figure 12 is the photo of a HPK wafer with 3 stripixel sensors. Each sensor has an active area of about 3 cm × 6 cm, with strip length of 3 cm. The leakage current of theses detectors are about on average of 0.4 nA/strip, and inter-strip capacitance of about 10 pF/strip.

The sensor design for the preproduction at HPK is of two types. One is the same as that of the 2nd prototype and the other is the new design described above. The wafer layout in the HPK includes three sensors on one 6" wafer. Our plan was to submit the process for 20 sensors including both designs with 625 µm and 500µm thicknesses. The HPK delivered in 2005 the preproduction sensors; the 500 um was obtained by thinning of the 625 um sensor.

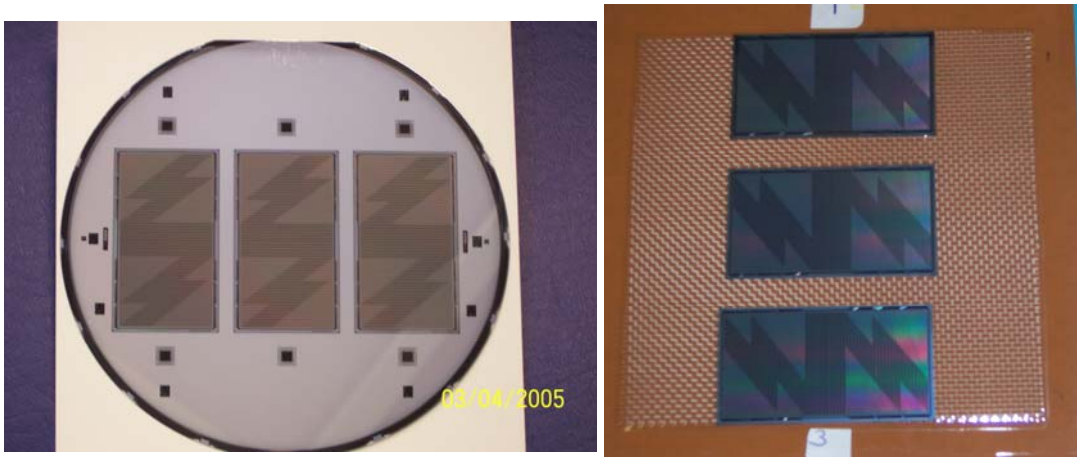

Figure 73 Left: A Hamamatsu wafer before dicing containing three new design sensors. Test diodes are seen along periphery of the wafers. Right: A Hamamatsu wafer diced at BNL

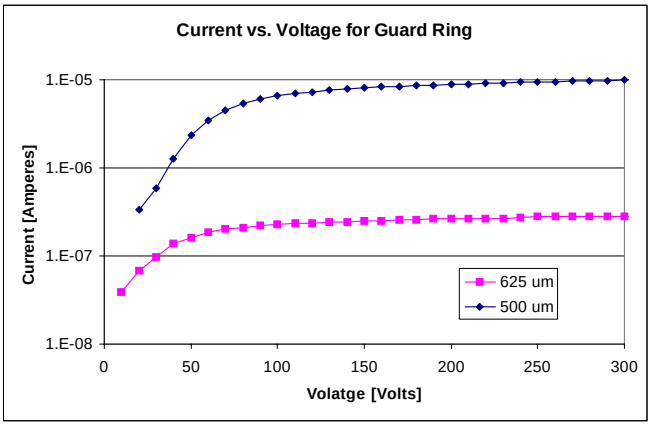

Figure 74 I-V curves of Guard Ring obtained from two sensors with two thicknesses 625, 500 um.

The sensors test at BNL with thickness 500 um sensors were found to have a significantly higher leakage current (for example, the Guard Ring current was 6 uA at V_{DF}=120 Volts) than the 625 um sensors (Guard-Ring current: 300 nA at V_{DF} = 120 V), see Figure 13. Similarly, strip current measurement show high leakage current for the 500 um sensors, which saturates the limit imposed by the SVX4 chips (15nA/strip). The 625 um new design sensors bonded to the SVX4 have lower measured strip leakage current (0.4 nA/strip) and have been chosen for the detector. A more detailed description of the tests can be found in the section strip tests section.

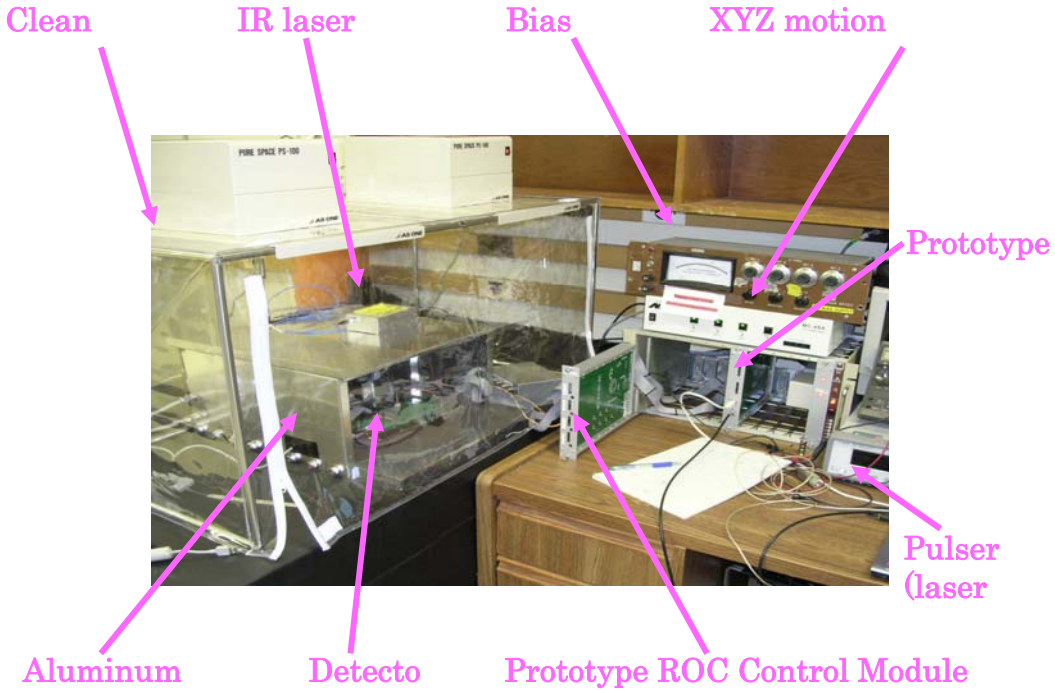

Figure 75 Laser test setup for the strip sensor of new design.

In the fall of 2005, IR laser tests have been performed on these HPK detectors in Oak Ridge National Lab. The IR test setup is shown on Figure 75. Detectors composed of the preproduction sensors and the electronics hybrids with the SVX4 readout chips were constructed, see Figure 76. The tests of the detector shown on Figure 76 using the IR laser tests presented on Figure 77clearly show the 2-dimensionl position sensitivity of the detector with laser induced signal in both X and U strips. Signal to noise ratio (S/N) measurements have shown a better than 20:1 S/N on these HPK Si stripixel detectors for PHENIX SVX. This value is as expected taking into account the charge sharing between the Y and U strips. For better understanding the S/N and the response of the detector to the charge deposition of minimum ionizing particle (MIP), we are studying the

optimization of the precision of the laser spot positioning. We are also planning to do source tests and building a telescope to measure the cosmic rays.

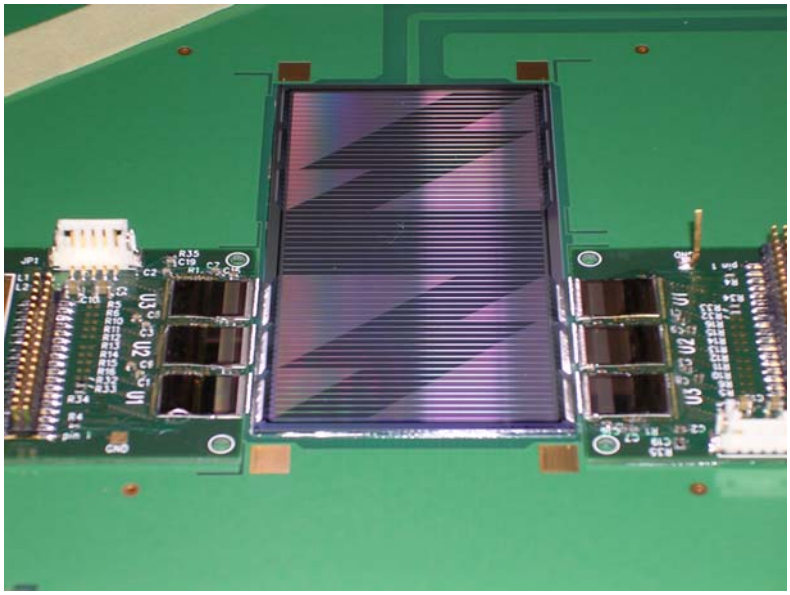

Figure 76 Prototype strip detector using HPK sensor of the preproduction.

Mass Production

The mass production of 400 sensors will soon start at HPK on June 2006. A QA program has been set at BNL/SBU/UNM to pick out 200 good sensors needed, and this task will be completed in 2007. The full silicon strip detector system will be assembled at BNL and installed in 2008-2009 in RHIC at BNL. A flow chart of the mass production of the strip detector is shown in Figure 78

- **Charge-sharing**
  - **IR laser pulse injection**
  - **Need optimization of laser spot size**
  - **Details are under study.**

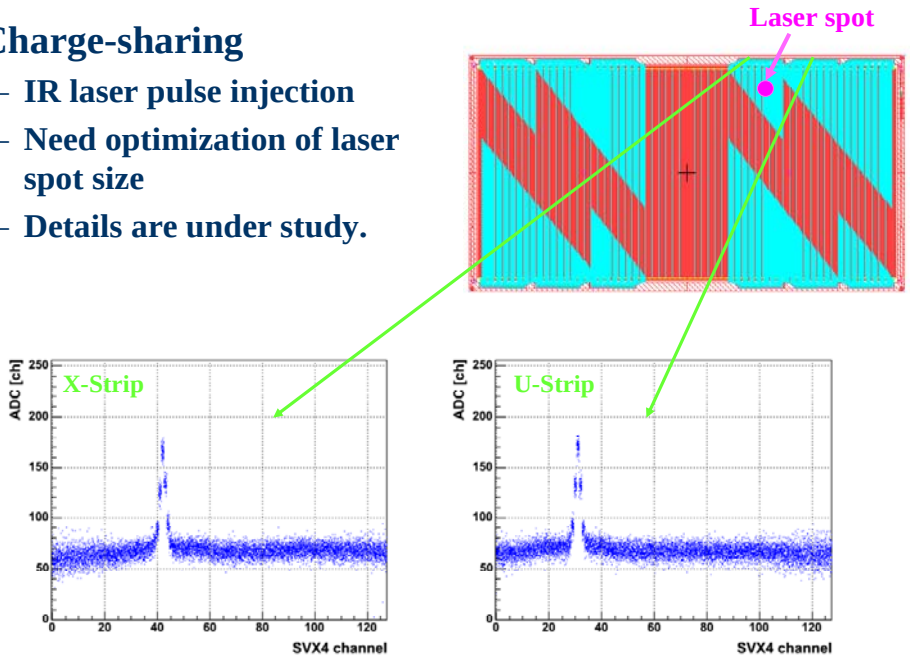

Figure 77 IR laser induced signals in X and U strips of a HPK Si stripixel detector.

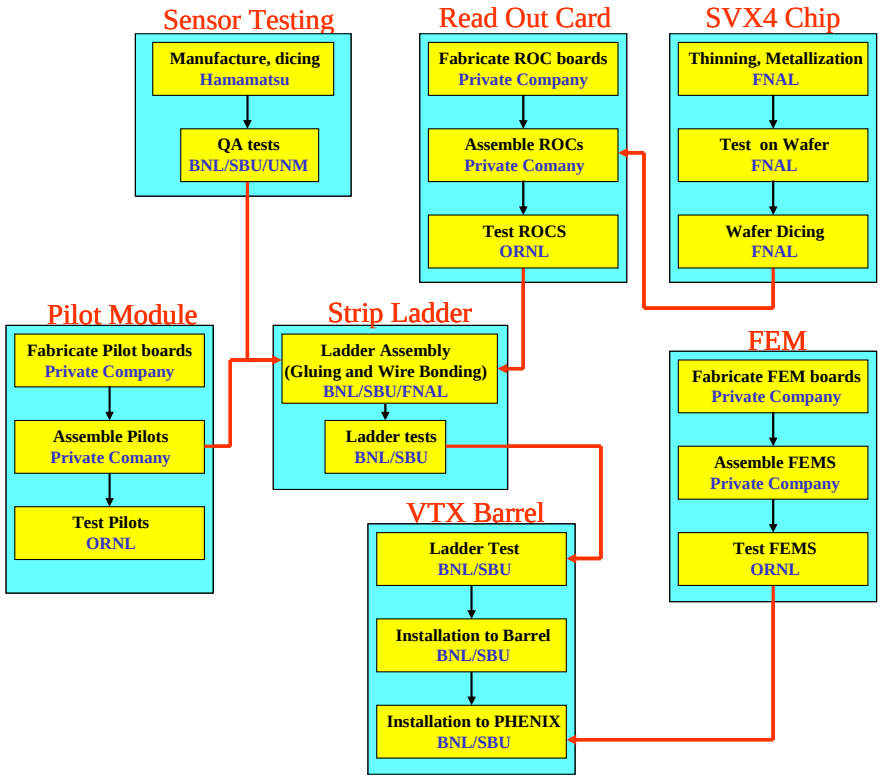

Figure 78 Strip detector production flow chart

Strip-pixel Front-End Electronics (FEE)

Overview

Schematic pictures of the strip-pixel FEE are shown in Figure 79 (physical overview) and Figure 80 (functional overview).

Racks: A PHENIX standard rack located on top of the PHENIX central magnet houses sensor bias supplies, low-voltage power for the front-end electronics, and Front-end Module crates.

Front-end Modules (FEMs): FEMs are the interface between the strip-pixel detectors and the PHENIX DAQ.

FEM-to-PM Cables: These cables carry signals and power from the FEM to the Pilot Modules in the inner detector region.

Pilot Modules (PMs): Located at the edge of the environmental enclosure, roughly 40 cm from the collision vertex, the PMs provide local power filtering and a form-factor transition for signals and power entering the detector acceptance region.

PM-to-Ladder Cables: Bring signals and power to the corresponding ladder, one azimuthal segment of the detector.

SVX4: The strip-pixels will be read out with SVX4 chips, a 128-channel 8-bit ADC ASIC developed by FNAL/LBNL.

Read-out Cards (ROCs): ROCs are thin printed circuit boards that host the twelve SVX4s plus control circuitry and a few passive components required to digitize data from one strip-pixel sensor.

ROC Control Chip (RCC): A custom ASIC developed for this project that serves as the interface between the SVX4s on one ROC and the corresponding FEM.

These different components are described in detail in the following sections.

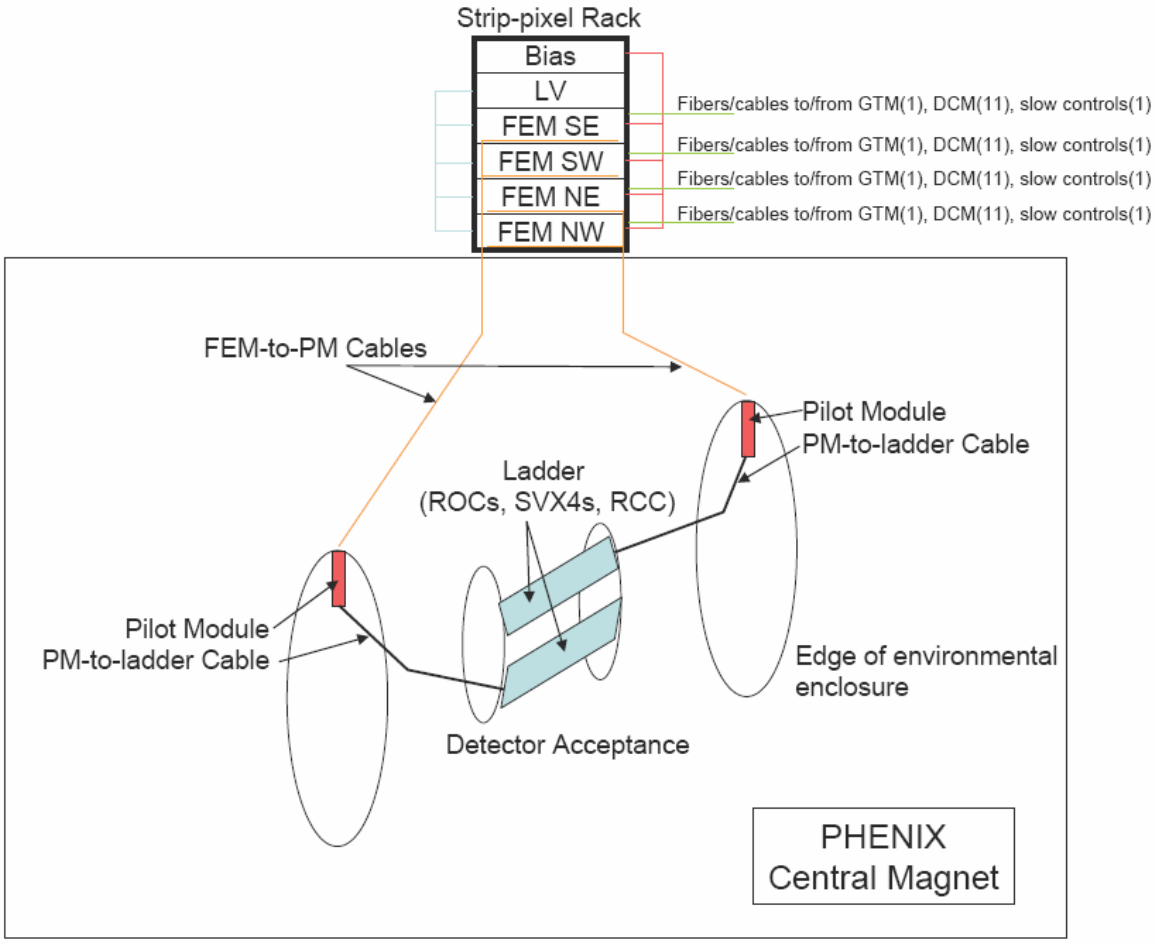

Figure 79 Physical overview of Strip-pixel FEE components.

Front-end Modules (FEMs)

Front-end modules serve as the interface between the ROCs and the PHENIX DAQ: Granule Timing Modules (GTMs) for clock and fast controls, ARCNet or Ethernet for slow controls and Data Collection Modules (DCMs) for archiving accepted event data. Each FEM services ¼ of the strip-pixel's 44 ladders, is housed in a commercially available crate with VME-standard hardware, and consists of one Controls Interface Board (CIB), eleven Data Interface Boards (DIBs, one per ladder) and a commercial backplane.

The CIB receives input from a GTM and the slow controls system. These signals are distributed across the backplane to the DIBs which parse the control commands received from the CIB, send them to their corresponding ladder, receive and format accepted event data from the ladder, and transmit those to a DCM. The DIBs also distribute low-voltage FEE power and sensor bias power to each ladder. Command parsing and data formatting functions are

implemented in FPGAs and have been largely exercised with existing prototypes developed at ORNL. The data formatting code is particularly simple, and is almost entirely a subset of code developed for previous PHENIX subsystems. It consists of setting the appropriate control bits, constructing the event header and trailer, and moving the 16 bits of channel/ADC data per struck channel (which comes in as two 8-bit words on opposite phases of a clock) onto a single 16-bit word clocked on the leading edge of a clock.

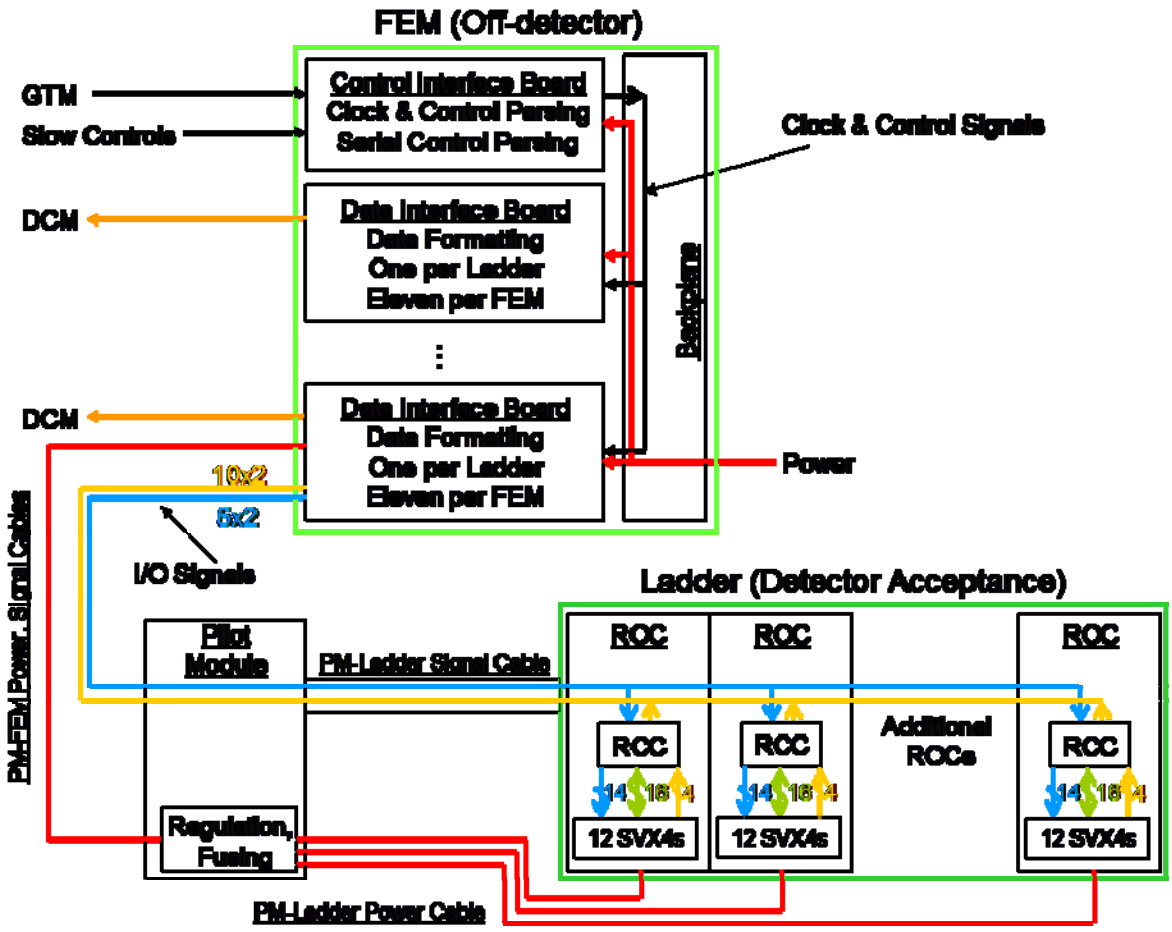

Figure 80 Functional overview of Strip-pixel FEE components.

FEM-to-PM Cables

Communication (control signals and data transmission) between a FEM and a PM is carried out using only LVDS signals to reduce noise. There are a total of 15 signal pairs, carried on ~10 m shielded twisted pair cables, that connect each PM to its DIB. A second cable carries power from each DIB to the PM. Separate analog (~9A/ladder) and digital (~4.5A/ladder) supplies are required, in addition to the sensor bias. Conductors will be sized to satisfy safety and

voltage drop requirements. Connectors for both the signal and power cables will be chosen to meet strict space requirements at the PM end of the cables.

Pilot Module

The ROCs need to receive timing and control signals, they need to send out data, and they need local power regulation, filtering and fusing. The region in and near the detector acceptance has limited space, limited serviceability, and can expect to see a significant radiation dose; all of which argue to put as little intelligence there as possible. Therefore we have chosen to have the PM pass the 15-pair LVDS control and data bus to/from each DIB directly to the ladder, only changing the form factor from twisted-pair cable (the FEM-to-PM cable) to a ribbon cable that can be wirebonded to a ROC (the PM-to-Ladder cable). The PM also has individual regulation, filtering and fusing circuits for each ROC, thus minimizing the consequences of single-point failure.

PM-to-Ladder Cables

The 15-pair LVDS control and data bus to/from each DIB is carried from the PM to the ladder on a single flex cable. The analog power, digital power, ground and sensor bias are carried to each ROC with a separate flex cable. Trace thicknesses and widths sufficient to maintain an acceptably low IR drop do not make a significant contribution to the overall material budget.

SVX4 readout chip

The strip-pixels will be read out with the SVX4 chip developed by FNAL/Berkeley collaboration. The SVX4 is implemented in the 0.25 μm TSMC process and is inherently rad-hard. It is a 128-channel chip with a 46-deep pipeline cycled by the beam-crossing clock, thus providing the LVL1-latency required by the PHENIX DAQ. LVL1-accepted events are stored for future pipelined readout. The SVX4 allows up to 8 bits of analog information, although the number of bits are programmable. Several pedestal-subtraction steps offer robust protection against common-mode noise. On-board zero suppression is provided for, but can be turned off (see discussion below). The SVX4 also provides for four-deep multi-event buffering required by the PHENIX DAQ. Protyping efforts at ORNL have allowed us to verify compatibility of the SVX4 with the PHENIX DAQ (serial programming, clock & fast control and data read-out).

In Fall 2003 FNAL cancelled the Tevatron Run-IIb silicon upgrade projects. Through a contract with FNAL we have purchased a sufficient number of tested-good die to complete the project.

Sensor Readout Card (ROC) / Readout Bus

CDF has implemented readout of a silicon detector using 2cm × 4cm circuit boards holding four bare-die SVX4 chips mounted chip-on-board, see Figure 81. We have chosen a similar implementation, but we require twelve SVX4 chips in a 3cm × 6cm area to readout both orientations (1536 channels) of a sensor.

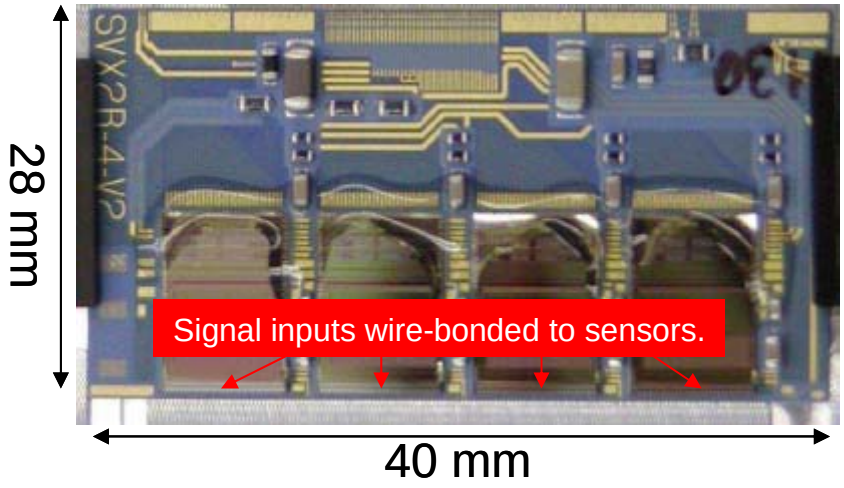

Figure 81 CDF Hybrid with dimensions shown. This board contains four SVX4 chips, local power filtering and traces for power, ground and data/control signals and is functionally equivalent to the proposed ROC.

Using a nomenclature common to a number of other PHENIX subsystems the circuit boards hosting the SVX4s are termed Readout Cards (ROC's). There is one ROC per sensor, five (layer 3) or six (layer 4) sensors per ladder and 44 ladders for a total of 246 ROC's (and 2952 SVX4s). In addition to the twelve SVX4s, each ROC has local power and sensor bias voltage filtering, a thermistor (connected in a resistor divider network to provide local temperature monitoring), and one custom ASIC known as the ROC Control Chip (RCC), which is described in the next section. A schematic drawing of the ROC is shown in Figure 82 on top of a sensor.

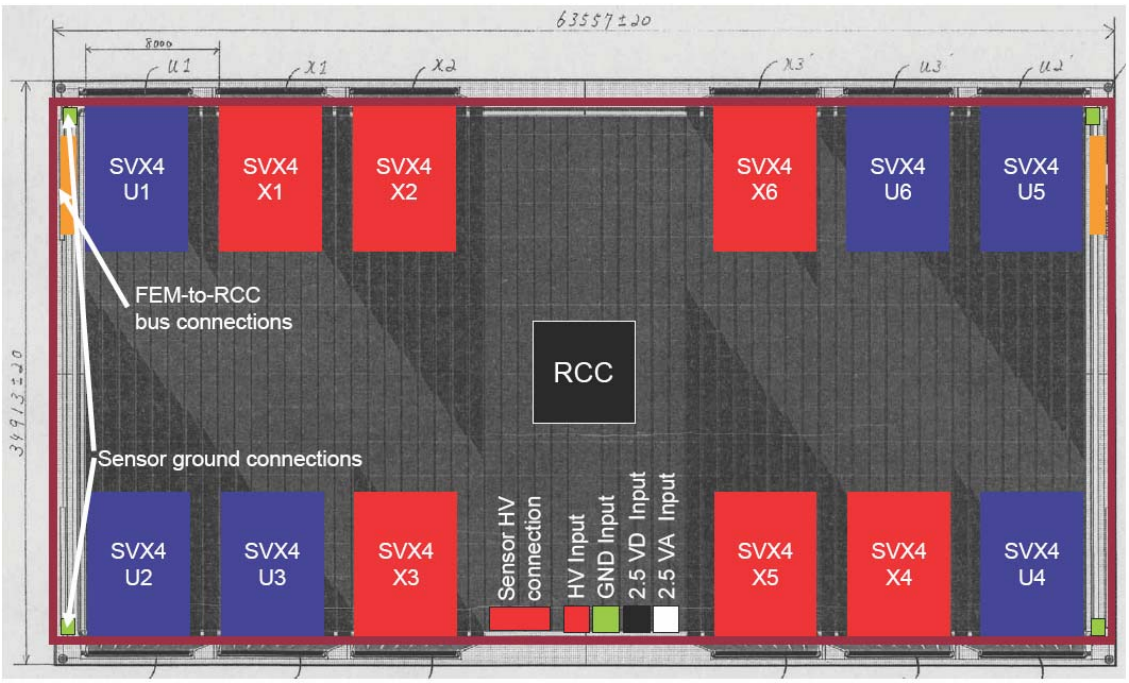

Figure 82 ROC top layer w/ major components (SVX4, RCC) and bus connections shown. There are a relatively small number of additional passive components required. One ROC reads out one sensor, a total of five (layer 3) or six (layer 4) are incorporated in one ladder.

The sensor design incorporates a pitch adapter directly into one of the metallization layers, eliminating the complication of an external pitch adapter. Since the ROCs are as large as the sensors the ladder geometry is greatly simplified by mounting the ROCs directly on top of the sensor. The bottom layer of the ROC (the layer adjacent to the sensor) is a shield layer with a single-point connection to ground.

There is an LVDS bus for communication between the FEM and the RCCs on each ROC. This bus is daisy-chained across ROC boundaries to form a bus without any extra material. Power is brought into each ROC separately to minimize voltage drop and the consequence of single-point failures. There is more than sufficient room for the ROC-to-ROC signal and power connections as shown in Figure 82 (signal buses are shown to scale assuming 100/100 μm trace/space).

In a typical application SVX4 chips share a common data bus with control of the bus mediated with a token-passing scheme. The twelve SVX4s on a ROC share one bus, but the bus control is broken into four separate pieces (one for each orientation of each half-sensor) whose action is controlled by the RCC. In

this way each orientation in each half-sensor can be bypassed, reducing the consequence of single-chip failures.

ROC Control Chips (RCCs)

The RCCs serve as a state-driven de-multiplexer, directing the serial and clock & fast control inputs and the data outputs. Chip operation is controlled by two input data lines, latched on the edge of the input 4xBCLK clock, and their corresponding enable lines, and by the geographical address of the ROC. The RCC also has one 8-bit ADC to digitize the voltage drop across the thermistor (which is reported in the accepted event data and can be read out via slow controls) and one 8-bit DAC to allow programming of the SVX4 test input voltage source. The RCC has LVDS and TTL I/O channels to communicate with its SVX4s and LVDS I/O channels to communicate with the FEMs. Like the SVX4s, bare-die RCCs will be mounted chip-on-board.

The RCC serves to minimize the effects of single-point failures (one broken SVX4 could take out all of the chips in its serial path) and avoids the need for individual signal readout cables for each sensor. The RCC ASIC technology is driven by radiation dose expectations and space constraints. These chips are largely digital and are being tested using an FPGA implementation which will greatly simplify any necessary revisions.

AC vs. DC Coupling

The SVX4 chip is designed for the use with an AC-coupled strip sensor but the strip-pixel sensor is a DC-coupled device. There are three consequences of the difference in coupling. The first is that the leakage current from the sensor will rapidly saturate the SVX4 input preamp. The preamp dynamic range is 200 fC, which allows a maximum 15 nA/strip leakage current given the minimum reset interval (~13 μsec) which is set by the RHIC abort gap frequency. The expected charge injected by collision-related hits in this time is negligible. The leakage current also increases the system noise. However, the SVX4 uses correlated sampling, measuring the pedestal on the first quarter of every clock cycle and the signal on the remaining three-quarters of the cycle. Therefore the noise increase is only due to the jitter on the injected electrons over three quarters of the RHIC 106 nsec clock cycle (at the maximum 15 nA/strip leakage current this corresponds to $\sqrt{7000}$ electrons ~ 85 electrons) which is less than 0.1% of the expected signal size. Finally, at room temperature the leakage current temperature is highly temperature dependent, which could result in significant time-dependent pedestal shifts. This effect is essentially eliminated by the SVX4 Real Time Pedestal Subtraction feature which, effectively, subtracts of the chip-averaged pedestal determined for each event.

All these problems are exacerbated by exposure of the sensor to radiation and are improved by cooling the sensors. An ASIC with 128 channels of RC circuitry to allow AC coupling the inputs was considered, but did not appear to be practical due to the large size required. Assuming operation at 0°C doses of 3×10^{12} n-eq./cm^2 can be tolerated before the leakage current with DC coupling becomes unacceptably large.

ROC Thickness

The thickness of the ROC is a critical component of the overall detector thickness. The thickness is dominated by the copper power, ground and shield layers. Therefore we have decided to implement the ROC as a standard (although thin) printed circuit board to reduce risk. Our best estimate for the total thickness is summarized in Table 9, and sums to 0.64% X_0 (assuming 17.2 μm copper plane thickness). Significantly thinner planes can be fabricated and will be tested as a part of our prototype effort.

Table 9 Summary of contributions to ROC thickness.

Component	Material	X0 (mm)	Length (mm)	Width (mm)	Scale Factor	Height (um)	Qty	%X0
Ground/Power/Bias planes	Copper	14.3	60	30	0.95	17.2	3	0.342
Passive elements	Estimate from second round ROC							0.030
SVX4	Silicon	93.6	9.11	6.4	1	300.0	12	0.125
Thruhole plating	Copper	14.3	60	30	0.1	25.0	1	0.017
Trace planes	Copper	14.3	60	30	0.56	8.6	2	0.067
Insulator layers	G10	357.5	60	30	1	25.0	5	0.035
RCC	Silicon	93.6	7	7	1	300.0	1	0.009
Gold flash	Gold	3.35	60	30	0.5	0.4	1	0.006
Nickel plating	Nickel	14.7	60	30	0.5	2.0	1	0.007
Total								**0.638**

Zero Suppression

The SVX4 allows for on-chip zero suppression. However, the PHENIX DAQ is not designed to handle zero-suppression prior to the DCM because the pipelined architecture assumes a fixed length data packet. However, the use of this feature has some significant advantages, as described below.

The digitization of the SVX4 ADCs proceeds in parallel and takes 128 clock cycles (uses both edges), regardless of zero-suppression. The data is then passed through the RCCs when the Data Collection Modules send a signal

indicating that they are ready to receive data. The data from each channel consists of an 8-bit address and an 8-bit ADC value. Data transfer from the SVX4s to the FEM uses an 8-bit bus which transfers the address on the leading edge of a clock signal and the ADC value on the trailing edge. So each channel's data is transferred in one clock cycle.

The readout of each SVX4 on the ROC needs one clock cycle for a header word and one clock cycle per hit channel (128 × occupancy). The maximum possible occupancy is 1. Readout and digitization can be driven by clocks of different multiples of the beam clock frequency (9.4 MHz) and must be completed within 100 μsec (943 clock cycles) for an entire ladder. This can be expressed by:

$128/M + 72\times(1+128\times\text{occupancy})/N < 943$ clocks,

where M is the digitization frequency in units of the beam clock frequency, and N is the readout frequency (defined similarly). The digitization frequency M sets the charge-per channel and needs to be set to 4 in order to have the signals fill the 8-bit range. The maximum value for N is 2 given that the fastest signal on a ROC is four times the beam clock frequency and we need to be able to latch signals on both clock edges.

We find that the maximum occupancy is 20%. The consequence is that we need to either a) use on-chip zero-suppression, b) use a significantly higher readout speed ($N = 10$), or c) have more output links per ladder. For cost and simplicity we have chosen to use the on-board zero suppression feature of the SVX4. An occupancy of 20% is more than five times the maximum expected luminosity for the inner barrel in central Au+Au collisions. Therefore zero-suppressed events *should* always fit in the required length of time (although a mechanism to pass up an error condition will still need to be developed).

We also cannot preclude the possibility that we will want to reduce the required time to 50 μsec, which would reduce the maximum occupancy to 10%, making it even more difficult to operate without zero suppression. This should still be sufficient safety margin on the occupancy (a factor of 2.5) assuming that system noise is under control.

The steps described above, digitization of SVX4 ADCs and readout of SVX4 data through the RCCs and into the FEM, is termed conversion. Data transfer from the FEM to the DCM is also subject to the 100 μsec restriction, but should proceed in roughly half the time as the conversion step since this step uses 16-bit communication.

Finally we need to maintain the ability to read out the entire detector with zero suppression turned off, both for the initial debugging phase and for regular pedestal collection runs. This is handled by increasing the conversion time and transfer time settings in the PHENIX DAQ and by configuring (via slow controls) the SVX4s and the FEMs appropriately (the SVX4s need to turn off zero suppression, the FEMs need to extend a timeout period and the length of the transferred data packet, and the FEMs need to modify a header word to communicate the different packet length to the DCMs.

Prototyping Results

We developed a prototype version of the ROC in which the SVX4s were mounted on four separate boards called "hybrids" (three chips each) that were mounted on the sensor edge and connected to a separate board containing the RCC circuitry in an FPGA implementation. A schematic picture of the hybrids attached to the sensor is shown in Figure 83. One sensor module (four hybrids wire-bonded to one sensor) was tested at ORNL. A picture of the setup is shown in Figure 84. Results look very promising, as shown by the ADC spectra in Figure 85. The average S/N ratio is 20:1.

We have also developed a second round prototype with the sensor form factor so that we can mount the ROC directly on top of the sensor. The RCC implemented as an off-board FPGA. The top layer of this board is shown in Figure 86. We have received 15 boards, of which one has been sent to RIKEN to practice the technique for attaching the sensor and one has been sent to a company to mount the SVX4s. We intend to assemble six sensor modules, corresponding to one complete ladder, into a telescope and test with cosmic rays and/or test beams, as illustrated in Figure 87.

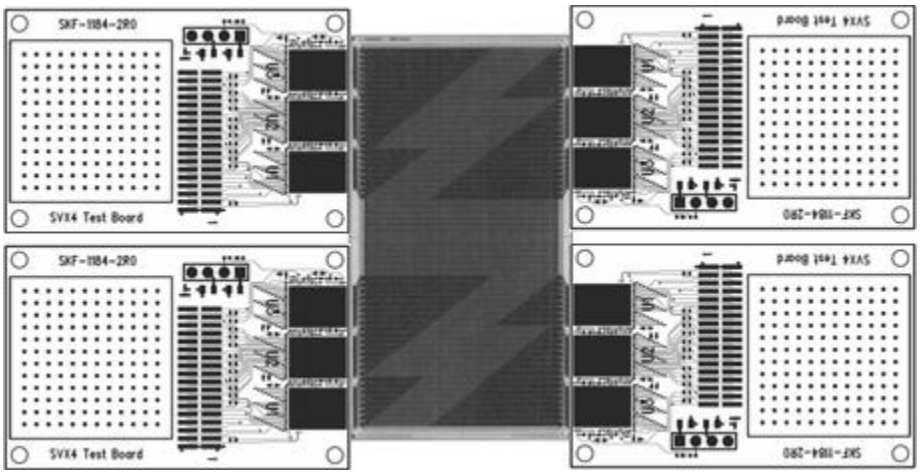

Figure 83 A schematic picture of four SVX4 hybrid boards of the first ROC prototype connected with a new design Hamamatsu sensor.

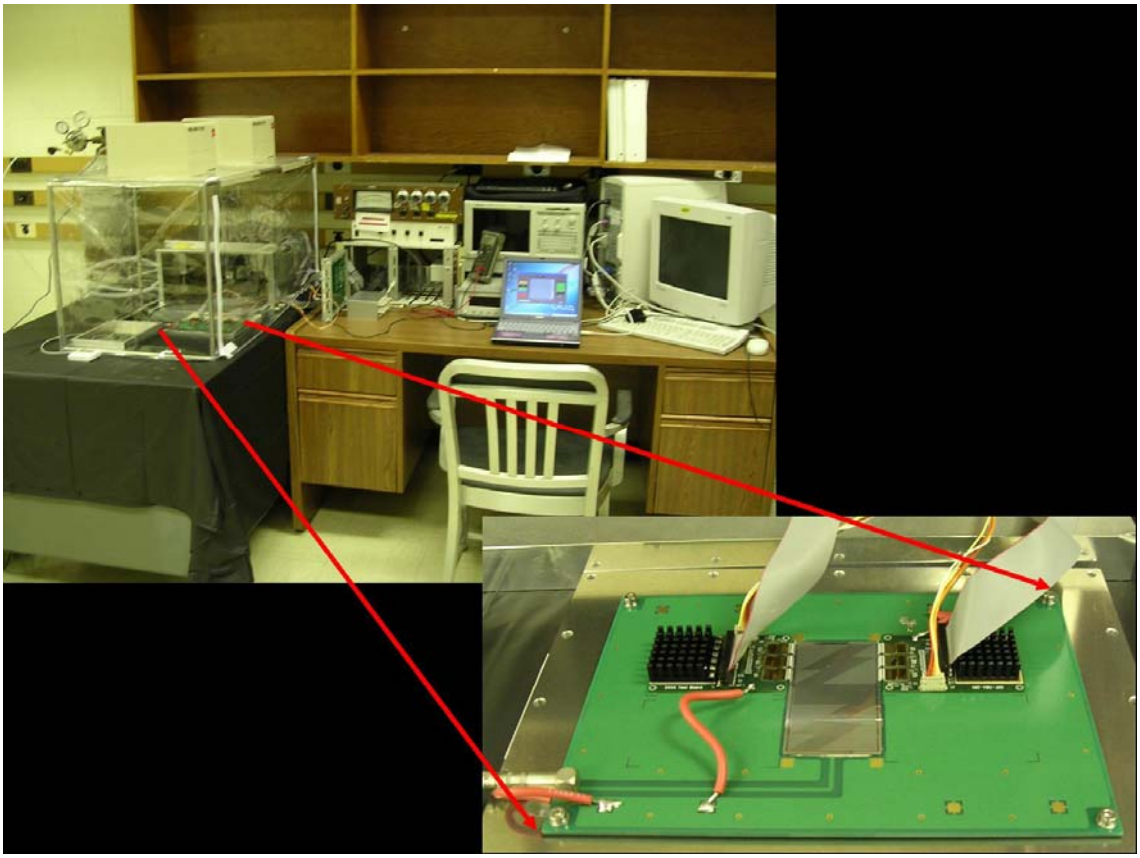

Figure 84 Picture of setup used to test first round ROC prototype.

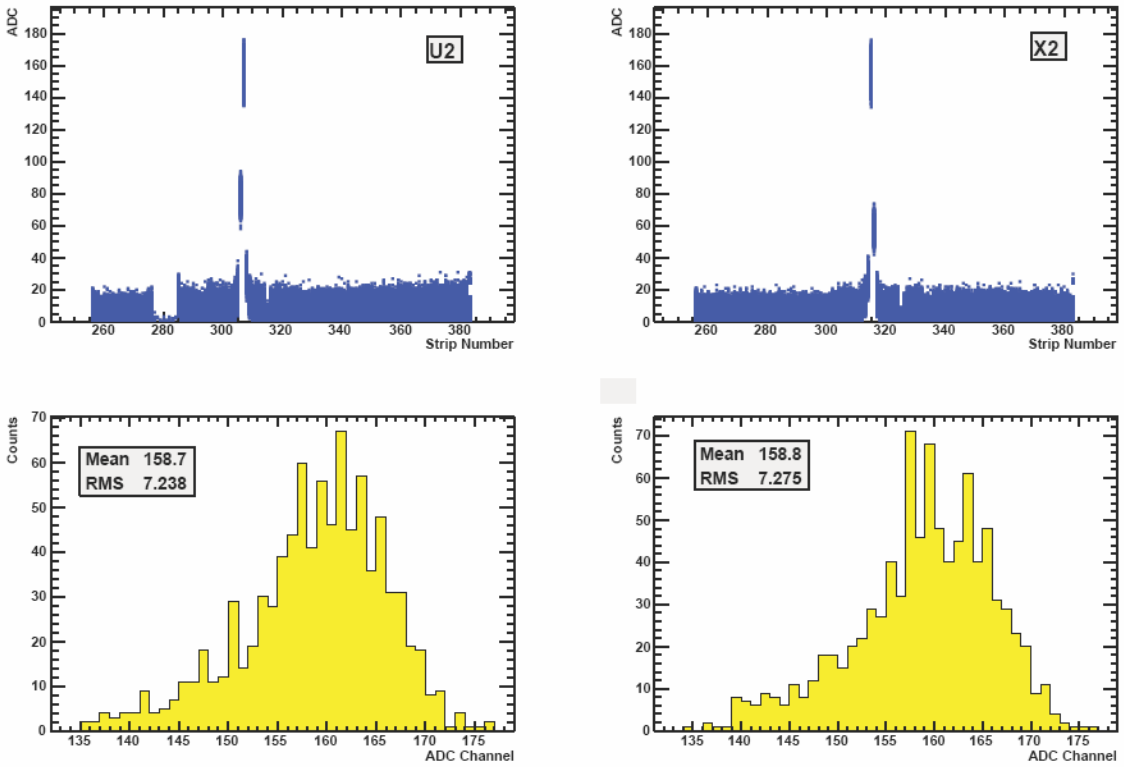

Figure 85 System response to synchronous laser pulses with a MIP-equivalent pulse height. Top plots show ADC vs. strip number for X and U strips (recall, when one pixel is hit there should be roughly equivalent signal in each orientation). The bottom panels show the ADC spectra for the peak channels in each orientation, showing a signal-to-background ((peak – pedestal / peak width)) of ~ 20:1.

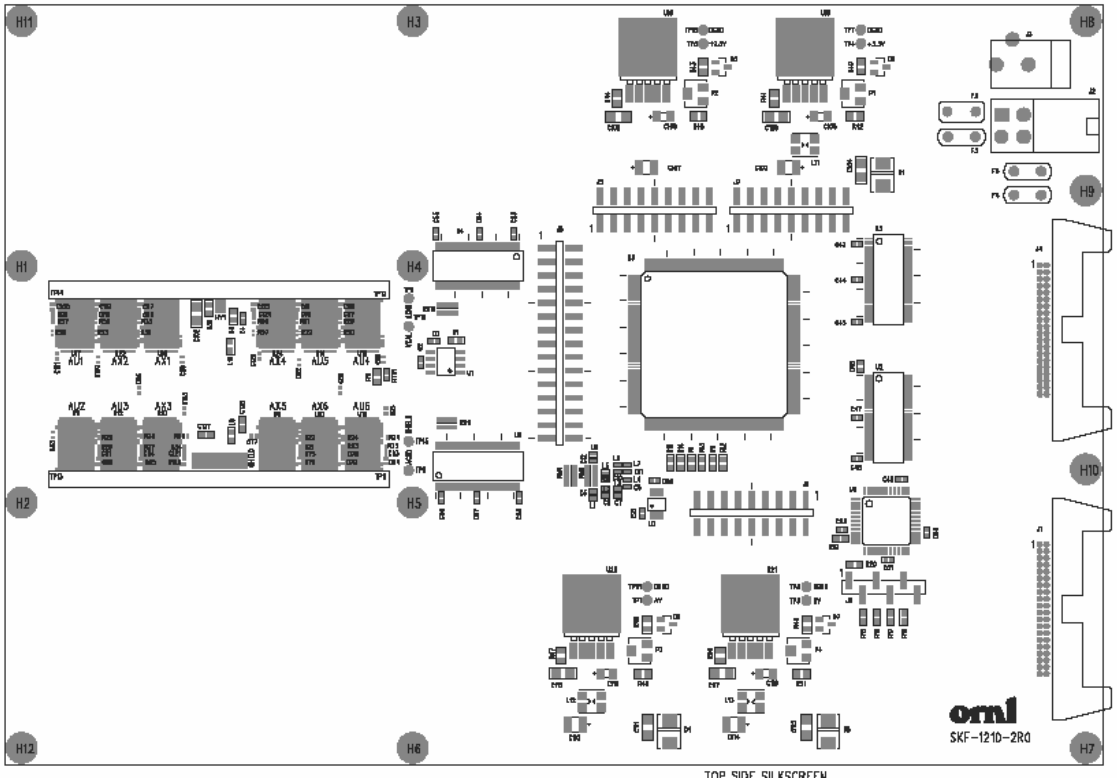

Figure 86 Top layer of the second ROC prototype. The SVX4s are mounted in the area on the left. The sensor mounts underneath this board with wirebonds reaching through slots in the board.

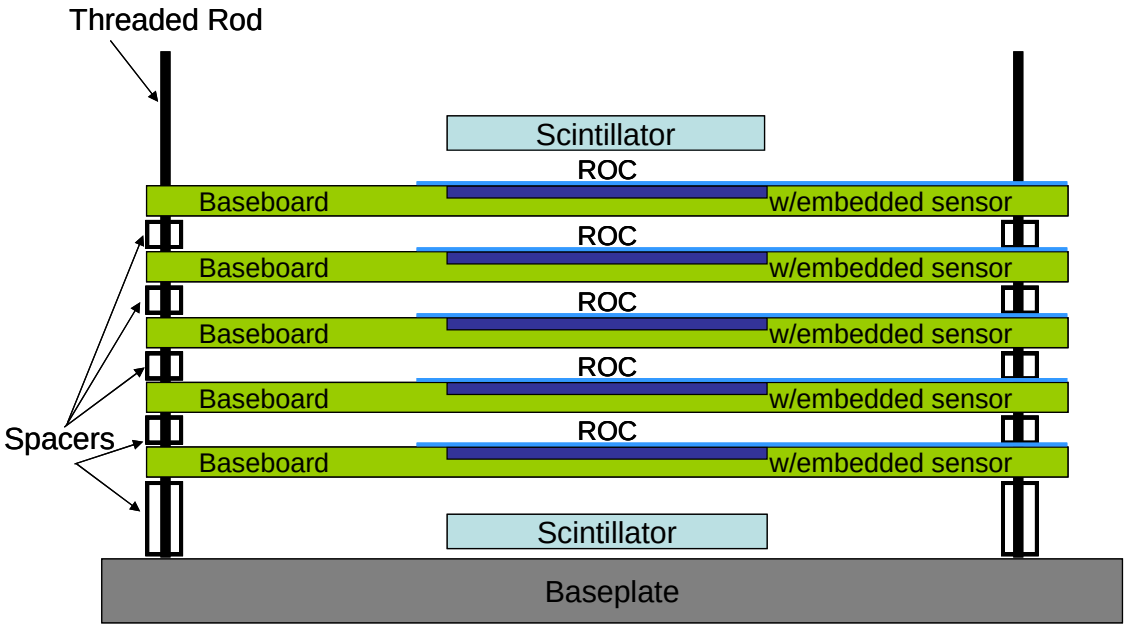

Figure 87 Schematic drawing of telescope assembly to test second round ROC Prototype.

Strip Testing

Testing facilities have been set up at Brookhaven National Laboratory (BNL), Stony Brook University (SBU) and University of New Mexico (UNM) to perform Quality Assurance (QA) tests on the stripixel sensors, see Figure 88. Each of the laboratories is equipped with a clean room containing a probe station. The UNM and SBU testing facilities were previously devoted to silicon testing for the CDF and DO experiments, respectively.

Figure 88 Left panel: The clean room for strip sensor QA tests at BNL. Middle panel: Picture of QA station at BNL. Right panel: Picture of QA station at SBU.

The testing procedures have been developed in the process of testing several rounds of test production sensors. Two vendors, Hamamatsu (HPK) and

SINTEF were chosen to produce the prototypes. This test production involved two different designs that we have designated “old” and “new”. The new design incorporates several features optimized for present design of the strip read-out card (ROC). The old design sensors were ordered from both SINTEF and HPK, but only HPK was able to produce new design sensors. Figure 89 shows the old design sensors on the left panel, the new design sensors on are presented in the middle panel and the diced wafer on the right panel. The dicing was done at the instrumentation division at BNL.

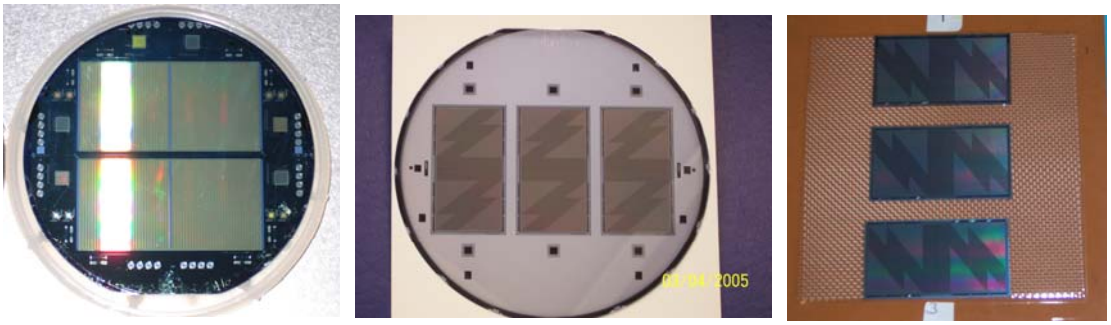

Figure 89 Left: A SINTEF wafer containing two “old” design sensors. Middle: A Hamamatsu wafer before dicing containing three “new” design sensors. Test diodes are seen along periphery of the wafers. Right: A Hamamatsu wafer diced at the Instrumentation division at BNL.

Selection of the company to produce the sensors:

Measurement of SINTEF sensor u-strips gave no current. This was due to a mask alignment problem during production. Figure 90 shows the misalignment between 2nd aluminum layer and the SiO_2 between the Al layers. HPK sensor did not have this problem.

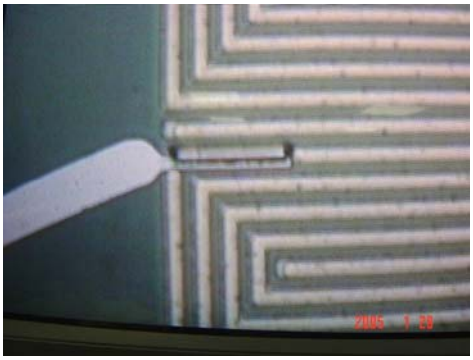

Figure 90 High resolution image showing bad read out connection to spiral sensor area. The Second Aluminum layer, containing the readout connector, is poorly aligned with hole in SiO_2, and so does not connect to first Aluminum layer.

QA tests of the prototypes sensors delivered from HPK:

In the first preproduction delivery, a total of 3 new design prototype wafers (9 sensors) with thickness of 625 um were delivered by HPK. Upon request HPK produced 3 wafers (9 sensors) of 500 um wafers by thinning a subset of the 625 um wafers. The dicing of the first wave of the preproduction was done at the instrumentation division at BNL. Dicing of a second delivery of the preproduction was split between BNL and HPK, and had 14 new design 625 um thick sensors. All of the 625 um and the majority of the 500 um have been subjected to a battery of QA tests. Each sensor underwent a visual inspection. Digital images of each section of the sensor were stored for future reference. On each sensor detailed I-V and C-V measurements were performed for the guard ring and a number of strips. Examples of such measurements are shown in Figure 91.

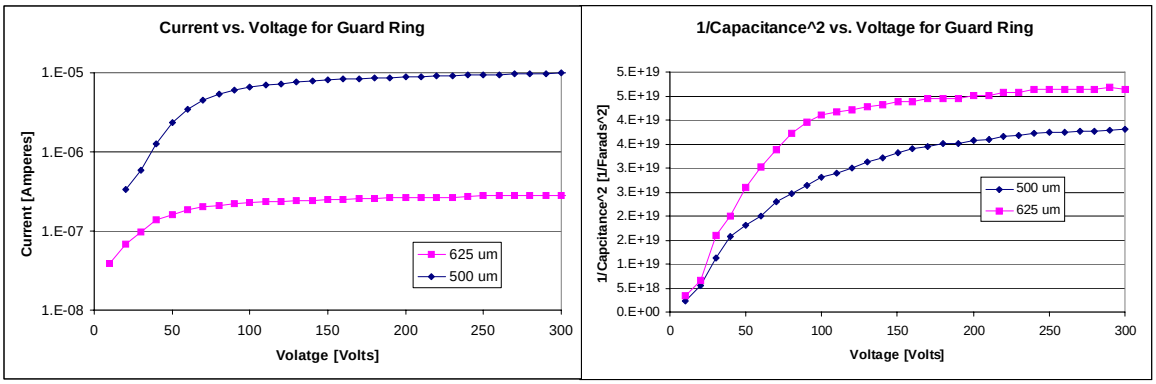

Figure 91 Left panel: I-V curves of Guard Ring obtained from two sensors with different thicknesses(500 um and 625 um). Right panel: C-V curves obtained from the same sensors used for I-V tests.

The 500 um sensors were found to have a significantly higher leakage current (for example, the Guard Ring current was 6 uA at V_{DF}=120 Volts) than the 625 um sensors (Guard-Ring current: 300 nA at V_{DF} = 120 V), see Figure 4. Similarly, strip current measurement show high leakage current for the 500 um sensors, which saturates the limit imposed by the SVX4 chips (15nA/strip). The 625 um new design sensors bonded to the SVX4 have lower measured strip leakage current (0.4 nA/strip) and have been chosen for the detector.

A more detailed test in which the current and capacitance were tested for each strip were performed at 200V. These tests are shown in Figure 5. The testing results are planned to be stored in a database and the results are accessible on the internet. The majority of the tests were performed at BNL and SBU. The

UNM facility has performed more specialized test on irradiated sensors which are described in section X (Sotiria's section).

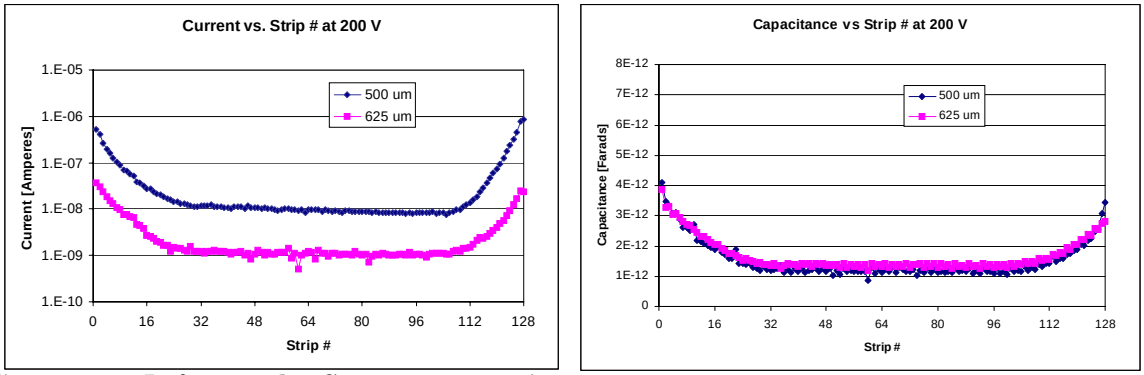

Figure 92 Left panel: Current vs strip obtained from two sensors with different thicknesses (500 um and 625 um). Right panel: Capacitance vs strip obtained from the same sensors presented in left panel. Rises on edges of both plots is due to edge effects of the grounding scheme when measuring with a probe card.

The test production sensors have been categorized into 4 classes. Sensors are classified based on bulk characteristics—whether or not the sensor demonstrates a clear full depletion region and high breakdown voltage—and strip measurements—the number of strips that show abnormal current and capacitance. Class definitions have been used to determine which type of tests each sensor is appropriate for. For example, telescope tests in which the sensors are bonded to ROCs required the highest quality sensors (class I) but irradiation tests only required sensors with at least partial functionality (class I-III). For the upcoming production round QA criteria may be modified based on sensor performance in the full read-out chain.

Measuring total leakage current of the sensor 625 um delivered from HPK:
To measure the total leakage current (I_{tot}) of the sensor and eventually to extract the leakage current per strip (I_{strip} = I_{tot} / #strip, where #strip = 12 x 128 = 1,536), two sensors tested for QA at BNL have been sent to RIKEN to be mounted on PCBs to apply bias voltage. All strips were wire bonded to a single pad on the PCB. The guard ring of the sensor was wire bonded to the GND pad of the PCB, see Figure 6. The I-V and C-V were measured at the room temperature 19.5 deg. C. The measurements of I_{tot} vs V and $1/C^2$ vs V are presented on Figure 7. The measurements revealed that the total current of the sensor I_{tot} = 302 nA and this implies that the current per strip is on the order of I_{strip}= 0.2 nA. These two sensors which have been wire bonded to PCBs were installed in the interaction region of PHENIX during Run 6 of RHIC to study the irradiation effect on the performance of the sensors. A similar scheme, with a sensor mounted on PCB at BNL and wire bonded at FNAL, will be used to study the stability of the leakage current as function of time for an extended period. The temperature and humidity will be monitor during this study at BNL/SBU.

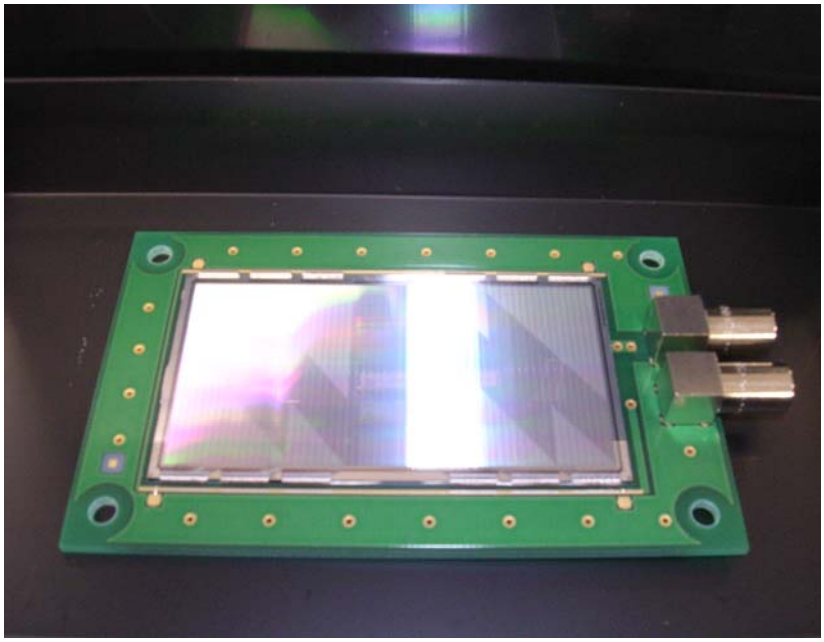

Figure 93 Picture of sensor 625 um thickness mounted on PCB to apply bias voltage. All strips were wire bonded to a single readout on the PCB. The guard ring of the sensor was wire bonded to the GND connection of the PCB.

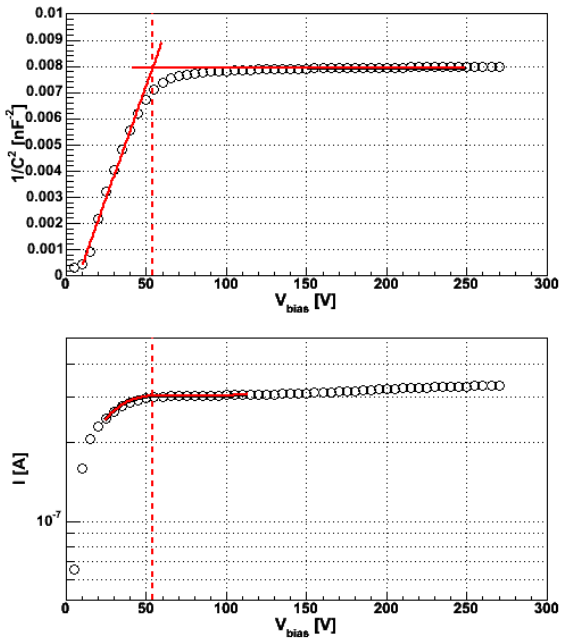

Figure 94 Top panel: Capacitance vs. voltage curve obtained from sensor 625 thickness mounted on PCB. All the strips are wire bonded to a single pad on the PCB. The bottom panel corresponds to the I_{tot} vs. bias voltage obtained from the same sensor discussed in the top panel.

Full production from HPK:

HPK is under contract to produce 400 sensors. These sensors are scheduled to begin arriving in June. HPK will perform resistance and doping tests and then dice the wafers. Further QA tests as described above will be performed at BNL, SBU and UNM.

The testing is supervised by one BNL scientist. Two graduate students from SBU are responsible for developing the testing software, analysis code, and testing procedures. 10 other students, from SBU and Iowa State University, have performed testing during the pre-production rounds. This level of manpower is expected to increase or at least remain constant during testing of the HPK full production sensors. Assuming a testing rate of one sensor per day the entire process should take a maximum of six months.

Strip Ladder Assembly

.

For the testing of the strip sensors and the SVX4 chips, we will benefit from the knowledge of the BNL Instrumentation Division and the cooperation with the FNAL silicon laboratory. The ORNL group, which is developing the ROC, will work together with other groups, including University of New Mexico, to test and assemble the ROC's. The University of New Mexico group draws on knowledge and experience gained during similar work for the ATLAS and CDF vertex detectors

For the silicon strip detectors the major steps that need to be taken are:

- Fully test sensor at the BNL laser test stand.
- Fully test the SVX4 chips at the FNAL electronics test facility
- Test bare readout card
- Mount SVX4s on ROC's
- Test ROC assembly. This will require cooling fixtures for the chips and mini-DAQ's at all fabricating institutions
- Attach ROC's to sensor
- Send to wire bonding facility
- Test ROC/sensor combo
- Assemble ROC/sensors into ladders. This will be done in manner similar to that done for the pixel detectors.
- Attach pilot modules to ladder
- Test complete ladder, needs complete cooling system and mini-DAQ.

4.4 Mechanical Structure and Cooling

A conceptual design of the silicon vertex detector was commissioned by the LANL group with HYTEC, Inc. HYTEC contributed to the ATLAS silicon group and has 15 years of design experience with silicon vertex detectors. For PHENIX they have also designed the station-1 muon detectors and the station-2 spider and also did the finite element analysis of the station-3 octants. The VTX mechanical conceptual design was finished and the report is summarized in this section.
[http://p25ext.lanl.gov/~hubert/phenix/silicon/HTN-111003-0001.pdf].

The next steps following this conceptual design are to fully specify the requirements for the VTX mechanical support and cooling. These requirements will incorporate the integration needed for all the PHENIX upgrade detectors in the inner region, including the VTX barrel described in this proposal, the silicon end-caps (FVTX), the hadron blind detector (HBD), and the nose cone calorimeters (NCC). Hence there are two major mechanical engineering tasks contained in this proposal: 1) the internal support and cooling of the VTX detector (described in this section) and 2) the integration of the VTX detector into the inner region of PHENIX (described in the next section).

For the internal support and cooling of the VTX detector, the major results from the conceptual study are:

- The use of sandwich composites will satisfy the radiation length requirements and provide the required stiffness.
- The outer frame structure should be a single diameter encompassing both the barrel and end-caps.
- The modular clamshell design can satisfy the stability requirements provided the connection issues are studied further.
- An octagon arrangement is suggested to facilitate utility routing and fabrication.
- Structural end disks at either end of the structure are recommended to prevent deformation.
- The ladders should have a simple support at one end and floating support at the other end to minimize thermal strains.

The R&D issues identified are:

- Building prototypes of ladder assemblies to verify calculations.
- Building full-scale prototype to test static and dynamic stiffness.
- Develop connections of modules.
- Develop support design.

- Refine calculations and develop full concept for 0 deg operation if necessary.

Design Criteria

The goal of the study is to establish a feasible design and to identify outstanding design issues. The study is based on a preliminary list of design requirements and a straw-man design of the detector structure. To adequately address all structural and mounting issues a fully integrated design, which includes the barrel detectors and future end-caps extension, is needed. This design needs to address all integration issues not only for the barrel and the end-cap vertex trackers, but also with other potential PHENIX upgrades.

The design requirements of the conceptual study were:

- Modular Design
  - End-caps detectors can be installed independently at a later time
  - Support structure separated vertically into two half shells
- Detector Coverage
  - Hermetic design
  - Four barrel layers
  - Four end-cap layers in each forward section
  - Fiducial volume < 20 cm radius, z < 40cm
- Radiation length goal < 1% per layer
- Room temperature operation desirable, 0 deg Celsius if needed
- Dimensional stability < 25 microns

In the conceptual study, the ALICE1LHCb pixel hybrids for the inner layer and silicon strip detectors with SVX4 readout for the three outer layers provide the basis for cooling and radiation length analysis of the barrel detector. At the time, for the end-caps a modified ALICE type chip that has 1/5 to 1/10 of the number of pixels was assumed[2]. These choices resulted in a estimated heat load of typically 0.7 W/cm^2 for the barrel and 0.1 W/cm^2 for the end-caps.

Structural Support

The selection of materials for the support structure is based upon the above criteria where the most important material properties are a low radiation

[2] After the completion of this study a more promising technology for the end-caps has been identified, but the heat load is expected to be similar.

length, low density, high stiffness, and availability. Out of three candidates (i) beryllium, (ii) graphite fiber reinforced plastic (GFRP), and (iii) Carbon-Carbon, the GFRP was chosen for the study because of its wide availability, works well in sandwich composites, and has good radiation length and strength properties.

Structural Analysis

The structural analysis includes two studies, a first study using finite element analysis models and the resulting modal frequencies to look at dynamic stiffness of tracker concepts and a second study to look at the static stiffness with mass loaded structures. The lower modal frequency limit is set at 70 Hz on a fully loaded structure so that the natural frequencies due to environmental conditions such as pumps, traffic, etc. do not couple into the structure and cause instabilities greater than 25 microns.

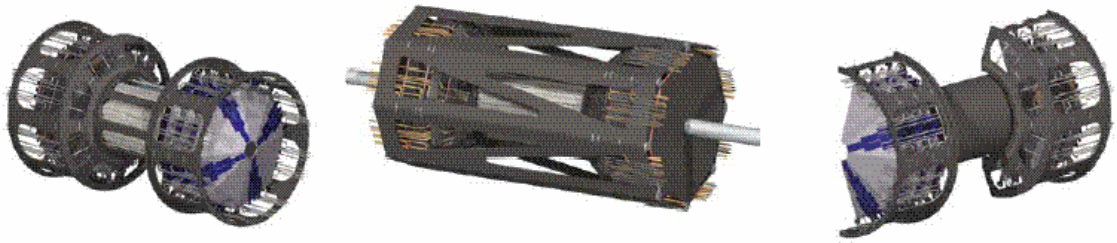

Figure 95 Design concepts studied for the vertex detector support structures. The center most concept with the constant outer diameter shell had the highest fundamental frequency.

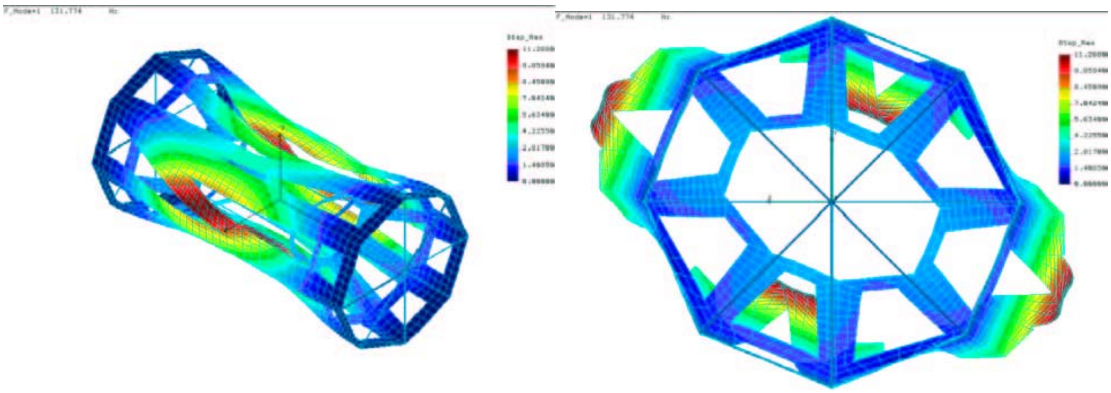

Figure 96 First mode shape that dominated the dynamic structural stiffness analysis

Various support structures shown in Figure 95 were studied. The center most structure has the highest frequency limit. The dumbbell shaped structure has the lowest mode frequencies below 53 Hz while the concept with the

uniform shell with constant outside diameter has the lowest fundamental mode at 132 Hz, well above 70 Hz. In Figure 96 the associated first mode shape of the concept that has the highest fundamental frequency is shown.

The static analysis under gravitational load is shown in Figure 97 for the concept with the uniform shell. A 1.0g load is applied vertically to the fully loaded structure. The maximum displacement is 14.5 microns and the maximum stress is 130 psi. These satisfy the design criteria so the uniform shell with constant diameter has been chosen as the concept to be pursued.

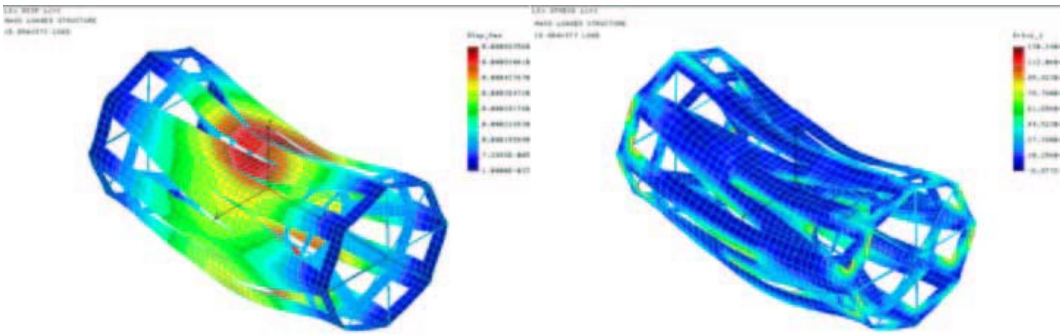

Figure 97 Displacement and principle stress from a 1.0g gravity load on a full mass loaded structure

Detector Ladders and Cooling

The mechanical design draws on a ladder concept for supporting both the inner layer of pixel and the outer strip detector layers. The pixel detectors and strip detector array are arranged in a longitudinal fashion, and at a slight cant angle, which provides a small amount of overlap for hermeticity. The pixel and silicon strip detector both contain on-board electronics, thus necessitating cooling along the Z-axis of the detectors, thus the ladders simultaneously must provide mechanical support and cooling.

The barrel region is about 30 cm in length and thus the ladders need to be supported only at their ends. Open ring like structures at the two ends of the ladders, shown in Figure 98, provide attachment points for the ladders and serve to combine the staves into two halves of a clamshell. Figure 98 also illustrates the cross section of a ladder structure, it is composed of a thermal plane (Carbon-Carbon) onto which the pixel modules or strip detectors are mounted. The thermal plane collects the distributed electronic heat, as well as providing a conductive path to the cooling tube. All elements are bonded with thermally conductive, rigid setting adhesives. The omega shaped piece holding the cooling tube on to the C-C thermal plane provides significant stiffness to the ladder.

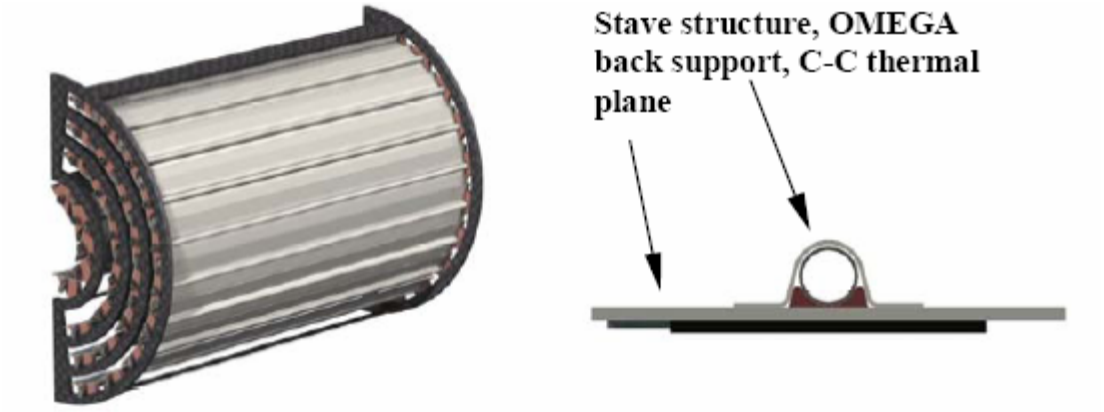

Figure 98 3D model of the barrel region on the left and the ladder structure on the right showing a cooling tube mounted on a C-C thermal plane and the sensor and electronics on the underside.

Cooling Analysis

The total heat load that must be removed from the vertex detector is at least 3.1 kW, which is dominated by power dissipation in the barrel detectors. There are generally two choices for the coolant system, single-phase and two-phase. In a single-phase system the coolant is circulated through pipes in a closed system. In a two-phase system the coolant arrives as a liquid and then evaporates into the detector volume where it is collected and removed. The two-phase system has the advantage that it is a more efficient coolant and a lower total mass is required. However, the two-phase system is more difficult to implement because of issues concerning more sophisticated temperature and pressure control. The single-phase system is simpler in implementation and design and therefore chosen to be the baseline design.

An important issue in the design of the mechanical structure is the operating temperature. In the initial design requirements we stressed the importance of room temperature operation and the design presented here is based on this assumption. However, the design engineers have developed the concepts that will allow operation at 0 deg by using suitable coolants that can operate at these lower temperatures. A more detailed study of the enclosure and thermal stresses would need to be done to confirm the concepts at reduced operating temperature. After this study was concluded, it was noted that the outer 3 layers of the barrel might perform better at 0 deg because of the mismatch between the SVX4 chip which is an AC coupled device and the strip sensor which is a DC coupled device. The concern centered on leakage

currents from the sensor that could saturate the SVX4 chip. The other option is to reset the chip regularly during the empty beam-crossing at RHIC.

The selection of coolants was based on previous experience in the design of the ATLAS detector and the choice was to use one of several perfluocarbon candidates, commonly called fluorinerts. These fluids can be used in either a single or a two-phase system and are environmentally acceptable. Based on a number of considerations the fluorinert C_5F_{12} was chosen as the baseline.

In comparison to the ATLAS detector the heat load is very modest and a single-phase system can be used. Since the barrel is only 30 cm long the design assumes that the ladders need only be supported at the ends and the cooling structure can serve as the means of joining the two half ladders of the pixel layers.

The concerns with this approach center on:

- Out of plane distortions from thermal strains due to different CTE's
- Gravity sag
- Mass of the structure exceeding radiation length guidelines

A series of calculations were done on the thermal aspects of this concept by using the outer barrel ladders since the greatest total heat load, 27 W, exists there. Using a temperature rise of 2 deg C as the maximum allowed temperature rise in the ladder the results indicate a good solution exists with an Al tube diameter of 3 mm and a wall thickness of 0.2 mm.

The result for the out-of-plane distortions for room temperature operation is quite acceptable, 0.18 microns. For the possible design requirement of 0 deg operation the out-of-plane distortions increase because of the difference in CTE's of the C-C and silicon, but is still acceptable at 3.5 micron. Bowing along the length of the ladder due to thermal strain because of the temperature gradient at room temperature is an acceptable 6.8 microns. However, if the detector is cooled, the bowing increases to over 80 microns. This is more than desirable so addition R&D is necessary.

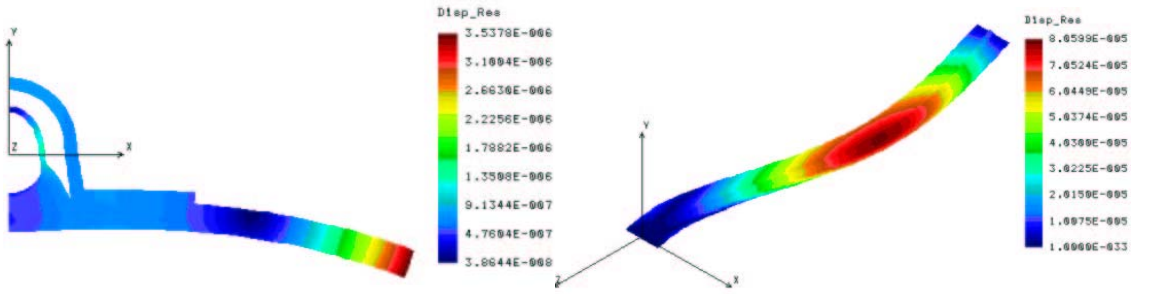

Figure 99 Left panel shows the out of plane distortions and the right panel shows the bowing for the 0 deg solution.

Figure 99 illustrates the 0 deg solution. While the temperature drop for the coolant is still the same as at room temperature the reference temperature is always 25 deg since that is the temperature of assembly. The increased bowing is due to reducing the operating temperature to 0 deg.

For the gravity sag the general bowing of the ladder is acceptable at 18-20 microns.

Radiation Length

The radiation length budget for the ladder described above exclusive of the sensor and electronics consists of:

- Composite thermal backplane
- The cooling tube and tube support
- The omega piece
- The coolant

The combined radiation length is 0.7% with the single largest contributor being the tube support (0.28%). The liquid coolant contributes 0.074%, cooling tube ~0.1%, and the omega piece and C-C facings ~ 0.2%.

Integrated Design

As a future extension of the VTX detector, we are planning for end-cap silicon detectors that cover the forward rapidity regions and the acceptance of PHENIX muon arms. The end-caps will complement the VTX barrel by providing larger rapidity coverage, higher total rates and greater reach in transverse momentum. The interface between the barrel and the end-caps is intended to be as seamless as possible, but because of their close proximity, care must be taken to avoid interference of their services for readout, power and cooling. This is already being done to streamline engineering on the

design. Although the end-cap detectors are not part of the present proposal, we include them in the mechanical design of the VTX for future upgrade.

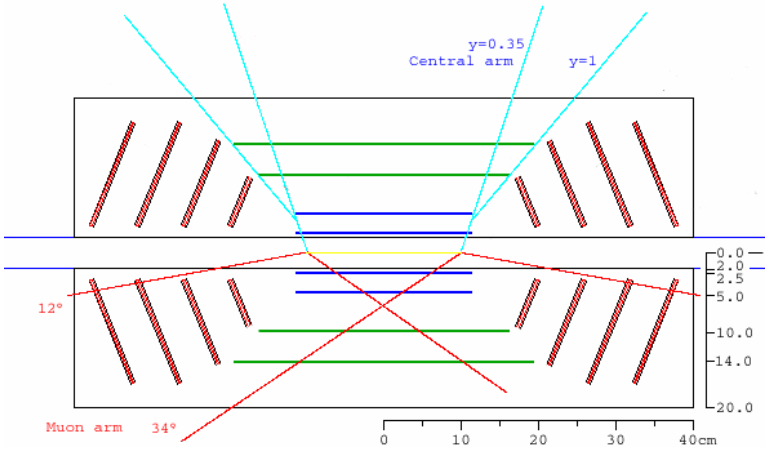

Figure 100 Schematic cross-sectional view of VTX detector (barrel and end-caps)

Figure 100 is a schematic for the current cross-sectional view of the VTX detector including both of the barrel and the end-caps. The blue lines are the pixel layers at radii of 2.5 cm and 5 cm, while the green lines are the strip layers at radii of 10 cm and 14 cm from the beam axis (yellow line). The cyan lines at an angle corresponding to a rapidity of y=1 define the edge of the strip layers. Also in cyan are lines indicating the PHENIX central arm acceptance. The set of four thick red lines on either side of the of the VTX barrel denote the position of the end-cap layers. The thin red lines on the bottom half indicate the PHENIX muon arm acceptance for an "interaction diamond" of z = ±10 cm. The black rectangles represent the envelope for the VTX, where clearance for the 4 cm diameter Be beam pipe defines the inner surface of this envelope, while space for future detector upgrades constrains the outer surface.

The right-hand diagram of Figure 101 is a refinement of the cross-sectional view in Figure 100, showing possible routings for cabling and cooling of the barrel layers. Two possibilities are shown: the inner layer services are routed along the beam pipe, while services for layers 2, 3 and 4 are routed out along a direction roughly corresponding to y=1. No support structures, or services for the endcap, are shown. The left-hand diagram is a perspective view demonstrating how services are brought in radially at both ends, using the entire perimeter.

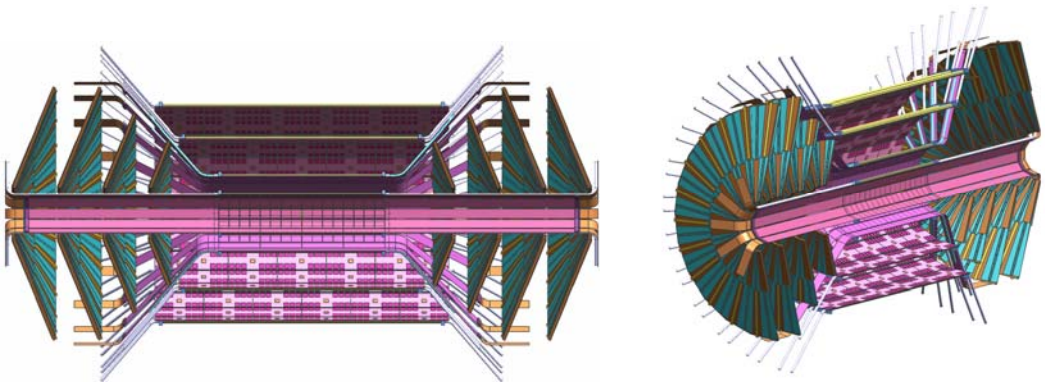

Figure 101 3D models of the VTX detector produced at LANL.

New design R&D

Since the completion of this study a new contract has been awarded to HYTEC to continue their design studies of the VTX detector, this work will be conducted during FY06 and 07. During the first year design and analysis of the barrel ladder staves will be completed. The ladder cooling tubes will be specified, along with the omega piece and thermal plane material. The barrel mounts will be designed along with the space frame that will hold the VTX sensor assembly. During the second year the suspension system for the space frame will be specified, along with the dry gas enclosure and the coolant system. As the final lay-out for the pixel and strip layers is finalized, a set of fixtures will be needed to allow for precision assembly of the ladders to better than 25 microns.

Figure 102 shows isometric views of how the internal design structure fits in the dry gas enclosure on the external suspension system. HYTEC's past experience has shown that detectors such as the VTX can experience two categories of loads, (1) "messy" or "dirty", and (2) "clean." In this case the messy loads associated with the gas enclosure, electrical cables, and utility lines should be decoupled from the clean loads associated with the GFRP space frame.

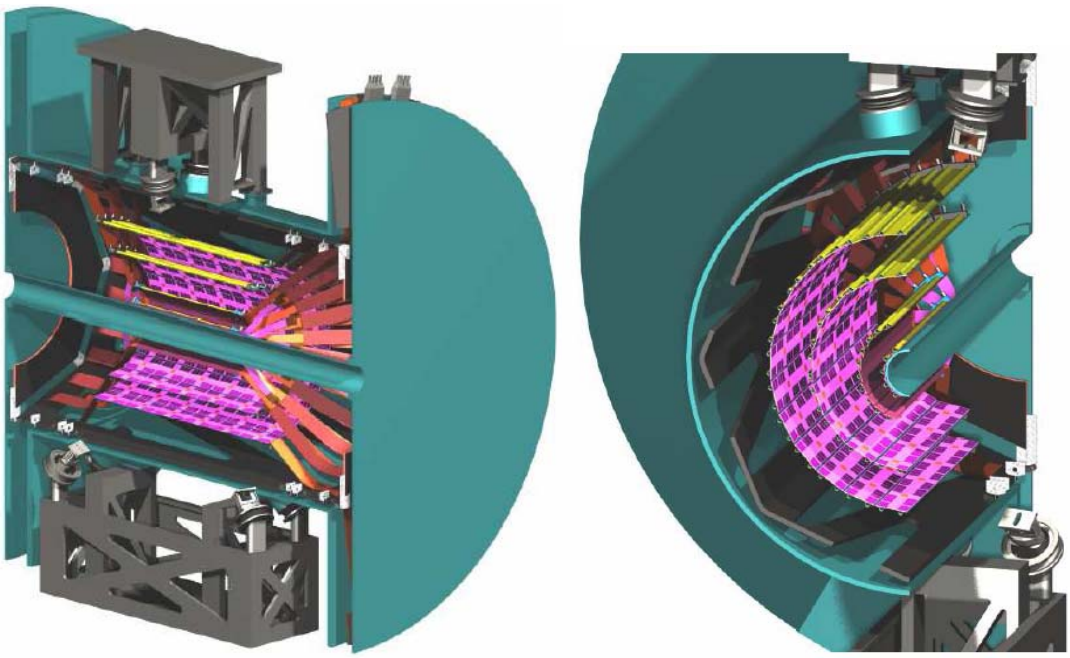

Figure 102 Isometric views of VTX from HYTEC showing dry-gas enclosure and suspension system

In Figure 102 it can be seen that hard points will be designed for separate mounting (or suspension) of the enclosure and the inner GFRP barrel space-frame structure. Connections from hard points to the inner barrel structure will be made via the metal bellows feed-through fixtures shown above and below the gas enclosure cylinder walls.

4.5 Detector integration into PHENIX

Once the individual detector components and the mechanical support structures become available, the VTX system needs to be assembled, integrated into the PHENIX setup, and connected to the support and ancillary systems as well as to the DAQ. These steps are critical for the successful completion of the project and need to be addressed well in advance and in close contact with the developments of the detectors and support structures.

VTX detector assembly

Each step from delivery of sensors and readout chips, to the assembly of detector ladders, to their final mounting in the mechanical support structure, will require intensive quality control and testing of the components. Special equipment, infrastructure and expertise are necessary to complete these tasks. We have started to plan the necessary steps and to optimize the use of expertise within our collaboration.

Error Budget

Our general philosophy will be to utilize fixtures wherever possible to allow the assembly of the VTX to be within the tolerances established by simulations. This will be accomplished by adhering to a strict error budget. The errors can be separated into intrinsic errors due to the strip width and assembly errors. The intrinsic error due to strip width is simply width/$\sqrt{12}$ = 23μm for an 80 μm micron strip. The assembly errors are due to the following,

a. locating the sensors to the precision alignment pin holes on the ladders
b. placing the ladders onto the structural frame
c. placing the assembly into the hermetic enclosure.

By using precision fixtures we will minimize these assembly errors to < 10 μm each. A precision drill fixture can be used to drill the pin hole on the ladders and in the structural frame. The structural frame will be held rigidly in a fixture that will allow positional changes during ladder installation.

Half detector assembly

All fully tested ladder assemblies, pixel and strip will be received by the BNL/Stony Brook and retested to insure that nothing was damaged in transport. The ladders will be inserted into the structural assembly beginning with the outermost layer proceeding to the innermost layer. The structural assembly will be securely held in an accurate holding fixture that will allow the structural assembly to be rotated so the ladders can be placed on the pins and fastened into place by either screws or glue and an accurate survey can be conducted and recorded. A final test of the completed half detector will be done under a full system test, full cooling and readout. If ladders are shipped to the assembly in small lots then much of the VTX assembly can be done in parallel to the ladder production.

Integration into PHENIX

Mechanical mounting

The mechanical mounting of the detector will be done by BNL PHENIX Operations, in close consultation with HYTEC. The current concept would be to support the VTX detector directly on a suspension system developed by HYTEC. The suspension system from HYTEC would attach to the mechanical support structure designed by BNL PHENIX Operations that spans between the copper nose cones on the pole-tips of the PHENIX central magnet. The two halves of the split barrel will be either hinged together at the top or the bottom, or be mounted independently.

The development of this concept will require careful consideration of a number of issues, including precision and stability requirements, accommodation of future detectors (e.g. silicon vertex detector end-caps, and nose cone calorimeters), the attachment and routing of cables, fibers and cooling tubes. Figure 103 shows how the vertex tracker is placed with other proposed upgrade detector in PHENIX in a small space inside of the PHENIX central magnet.

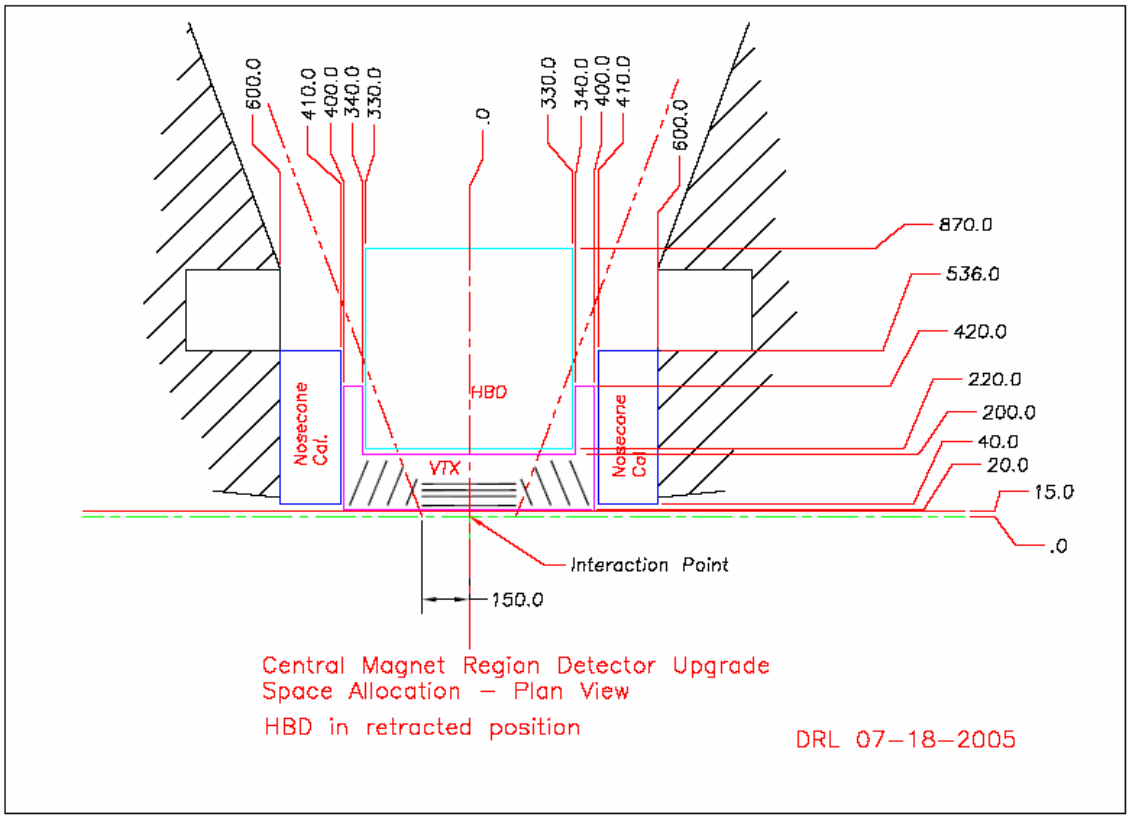

Figure 103 The inner region of PHENIX central magnet with the envelopes of proposed upgrade detectors. The silicon vertex tracker (VTX), a hadron blind detector (HBD), and nose cone calorimeters are shown.

Support and Ancillary Systems

Additional platforms installed on top of the PHENIX central magnet yoke will be required to support electronics racks and cooling system equipment. These racks will include space for low voltage and bias supplies, and whatever readout electronics for the silicon detectors. The platforms must also provide area for cooling system pumps, and compressors or chillers. In addition, these platforms will be used for ancillary systems in future detector upgrades in the central magnet such as the HBD.

Beam pipe

A new beryllium beam pipe with a smaller 4 cm inner diameter and 500 μm nominal thickness will be critical to perform the anticipated measurements. The inner surface of this pipe may need to be NEG (non-evaporative getter) coated to help reduce beam induced vacuum instabilities. The new beam pipe will need to taper out to match the standard 5 in diameter lines of the RHIC rings.

DAQ

The VTX readout system will be matched to the requirements of the PHENIX high rate data acquisition (DAQ) system. The current DAQ system has a bandwidth corresponding to approximately 10 kHz level 1 (L1) trigger rate with a planned upgrade to 25 kHz. Currently each front-end module (FEM) sends uncompressed events of fixed length to Data Collection Modules (DCM) through a gigabit optical link. Each DCM has four sets of optical receivers, field programmable gate arrays, and digital signal processors (DSP), which zero-suppress and buffer the events from four FEMs. An additional DSP is used to merge the data from the four sets. The DCMs and FEMs pipeline events with the capability to buffer at least 4 L1 triggers. Since the FEM data is of known length no data flow control between FEM and DCM is necessary in the current design and only the DCM participates in the busy logic for the DAQ.

Because the VTX will deliver substantially larger data volumes than the currently operated detectors, it will be necessary to zero suppress the data at the front-end before it is transmitted to DCMs. As a consequence some of the current DCM functionality must be taken over by the read-out cards on the detector and the FEMs off the detector. In particular, after the zero suppression, the FEM data will no longer be of fixed length and therefore the FEMs must participate in the busy logic.

Since the new requirements are common to most of the planned PHENIX upgrades detectors, we have launched an R&D effort to develop the new DCMs independent of this proposal. We anticipate that the development will be completed within 2 years, in time to produce new DCMs for the VTX detector. Once the new DCMs are completed the PHENIX Electronics Facilities and Infrastructure (EF&I) and Online Computing Systems (ONCS) groups will oversee the electronic integration and readout of the VTX detector.

4.6 Software

Software infrastructure development and integration in PHENIX

Significant progress was made in developing VTX off-line software infrastructure, and integration of VTX software in the PHENIX software framework. Code for storing and retrieving various VTX parameters (geometry, simulation parameters) from the PHENIX database was developed, and is used

in simulated event reconstruction. VTX hits are a part of the PHENIX global tracking and can be used for improving momentum determination of charged tracks and reconstructing displaced vertices.

Two different algorithms can be used for including VTX hits in global PHENIX tracking: Kalman Fit, and the default PHENIX global tracking package (CGL). The future work in this area will be concentrated on optimizing global tracking parameters for both Kalman Fit and CGL in order to improve position and momentum resolution, and on further database development.

Standalone tracking

In parallel to the track matching effort, an algorithm for standalone tracking in the VTX is being developed by The Stony Brook University group. VTX detector can not provide as good momentum resolution as the PHENIX Drift Chamber, but large acceptance of the VTX detector will be helpful for correlation studies (e.g. jet correlations).

The code uses the two pixel layers to reconstruct the primary vertex. Then, using all four layers (and the primary vertex), the algorithm determines multiple scattering between layers for a track candidate, and uses that information to find the probability that the candidate is a true track. The reconstruction efficiency is close to 100%. In addition to track reconstruction, the algorithm can also determine the momentum of the tracks with resolution better than 20%. Momentum resolution for charged tracks with momentum > 1 GeV is shown in Figure 104.

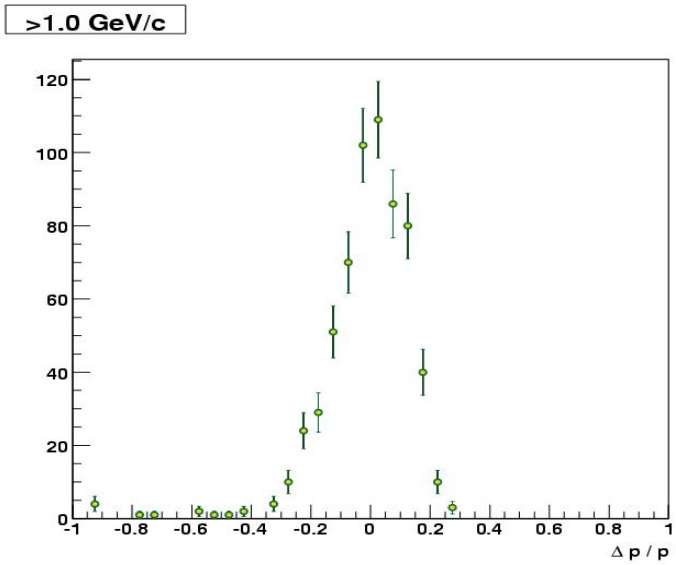

Figure 104 Momentum resolution for charged particles with momentum > 1 GeV obtained using VTX standalone tracking.

Event display

Stony Brook University group also develops an event display for the vertex upgrade.

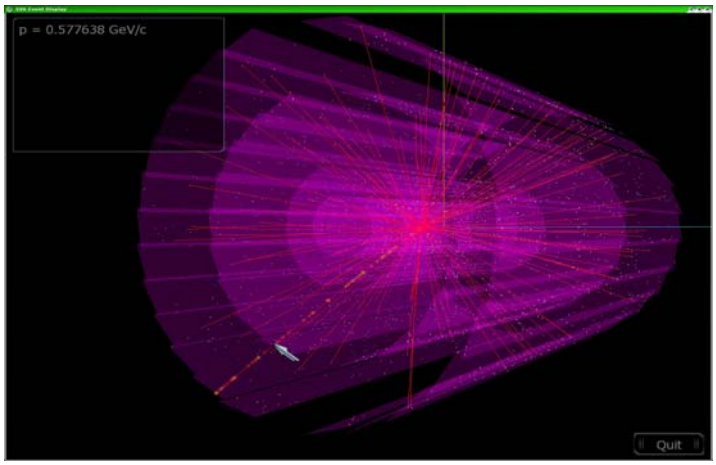

Figure 105 Example of VTX event display

This event display allows to view pixels and sensors, show hits and tracks from any angle, and display track information. The code is based on OpenGL, and an example of the event display is shown in Figure 105.

Simulation studies

Several large scale simulation projects for general use are planned. One such project – simulation of Au+Au events at 200 GeV using Hijing event generator is already completed. Events generated in these projects are used to optimize detector parameters and to test and improve offline software.
One recent example is a comparative simulation study on the influences of the silicon vertex detector material budget on some of the physics measurements by PHENIX. These include the J/Ψ mass resolution and acceptance and the Distance of Closest Approach (DCA) for reconstructed trajectories in the Central Arm of PHENIX. We inferred that, without using the hit information from the Vertex detector, the J/Ψ mass resolution is degraded by about 10 MeV/c^2 and the efficiency by about 30% (see Figure 106) for a thickness of 5.6%. There is an on going effort to look further into the problem by including hits from the vertex detector and tuning the hit errors used in the tracking.

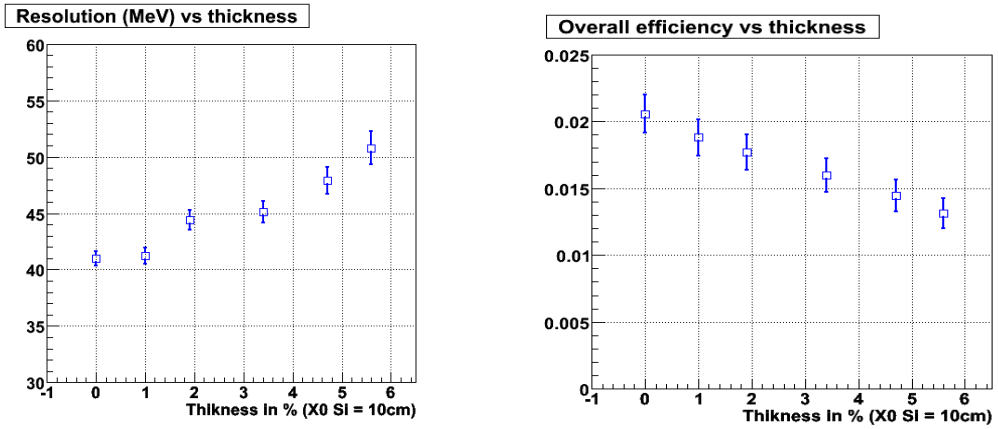

Figure 106 J/Ψ mass resolution (left) and reconstruction efficiency times acceptance (right) as a function of the silicon vertex detector sensor thickness.

Detector database

In parallel with offline database development, a database to store Q/A test, assembly, geometry, and calibration data is being developed. This database system (PVD) uses several technologies that are based on open-source applications which are already used in the PHENIX computing environment. The database back-end is based on PostgreSQL 7.3 (upgrades are expected), which is already used for the main PHENIX database. The web server is Apache, with PHP support enabled, allowing for active web pages that access the DB information. Finally, we are using standard PHP packages for DB access and graphing (jpGraph).

At present, the sensor inventory system is partially implemented and under intense development, with completion expected by late spring 2006. Bench test information (CV and IV) are already being shipped directly from the Labview PC in the silicon lab, directly

to the PVD server. This information can already be accessed online and graphs can be produced automatically. This functionality will be integrated with the inventory system as it is completed.

As the VTX construction continues, it is expected that the DB design will evolve with it on short time scales, with relevant web pages developed to access the new information. BNL Chemistry (P. Steinberg) is coordinating this work, with help from the USB group, at least for the Stripixel bench tests.

Future plans

The focus of our efforts in the future will be shifted towards preparation for the real data analysis. Tools for data decoding, detector alignment and calibration will be developed. To store alignment and calibration results in the PHENIX database current database code will be upgraded. Clustering algorithm will be developed.

Simulation studies will continue in order to optimize reconstruction. For this purpose we plan to run large simulation projects for general use. One such project – production of simulated AuAu events at 200 GeV using Hijing is now completed. Simulation of single B and D mesons and embedding them in AuAu Hijing events will start in the nearest future. Other simulation plans include developing better detector response.

5. Project management and responsibilities

The organization and management of the proposed effort is embedded in the management structure of the PHENIX experiment, which is part of the BNL RHIC project. The new organization must satisfy a number of requirements including a clear interface to the existing RHIC and PHENIX management structure, clear roles and responsibilities within the existing PHENIX subsystem structure. Particular attention has to be paid to the fact that a significant portion of the project is supported by foreign contributions. Clear deliverables, responsibilities for deliverables and the accountabilities of the participating funding Agencies have to be defined. These responsibilities will be formalized in memoranda of understanding (MOU's) between PHENIX and the participating institutions. In this section, we outline our proposed management organization and delineate responsibilities within the project.

5.1 Project background

The proposed project is part of a detailed upgrades program to enhance the physics capabilities of PHENIX over the next 8 years. Realizing this plan will enable PHENIX to remain competitive well beyond the turn on of LHC expected for 2008, as well as to advance our understanding of QCD by fully exploiting the unique spin physics capabilities of RHIC. The plan covers a broad range of measurements in *A+A*, *p+A*, and *p+p* and its goal is to provide key measurements which currently can either not be addressed at RHIC or only with limited accuracy.

The development of the PHENIX upgrade program started in response to the NSAC long-range plan developed in 2000. The strategy was consolidated at a workshop in Montauk, NY March 2001 and at BNL August 2002. Since then individual upgrades have been followed up in detail within four PHENIX study groups.

The PHENIX upgrades plan was first presented to BNL management in a proposal seeking funds to initiate a broad-based R&D effort to develop the detector technology necessary to realize our goals. BNL charged a Detector Advisory Committee (DAC) to review the R&D plan. After the first review December 19-20, 2002, at BNL the committee named the PHENIX silicon vertex tracker a high priority in the future development of PHENIX. Some quotes from this report:

"Physics Motivation: … Charm has emerged as valuable probe of QCD dynamics … The measurement of hadrons with open charm requires excellent vertex identification, which can only be achieved with state of the art silicon vertex detectors …"

"PHENIX Microvertex Tracking Detector: The extension of the capabilities of the PHENIX detector to provide a direct measurement of charm and open beauty will have major impact on a number of physics questions both in *A+A* and *p+p* collisions. This upgrade is therefore a very high priority in the future development of PHENIX."
"It is likely that a detector system with adequate performance can be constructed using existing technology and it is therefore possible and desirable that a detailed proposal for this upgrade be in place in time for inclusion in the planning process for FY05 construction funds."

Responding to the DAC review, the silicon study group developed a PHENIX internal letter of intend proposing a two component silicon vertex tracker system, one component - a barrel detector - extending the capabilities of the PHENX central arm detectors and the other - an end-cap detectors - extending the physics reach of the muon detector system. This LOI was reviewed in March 2003 at a joint meeting of the PHENIX detector council (DC) and executive council (DC). Following their recommendations PHENIX management (PM) endorsed both projects and charged the silicon study group to develop a proposal for a silicon barrel detector for immediate presentation to DOE through BNL.

The DAC met again on Nov 22-23 2003 and reviewed a preliminary version of the VTX proposal. The committee report stated that "the Collaboration has made impressive progress…. and a viable design is close." They raised seven issues or concerns, which have been addressed in a revised proposal that was submitted in October 2004.

In NSAC subcommittee Review of Heavy Ion Nuclear Physics report (November 2004), they recommended that construction of the PHENIX Silicon Vertex Upgrade as one of the essential investment in the field.

The revised proposal was then reviewed by a Technical Advisory Committee in January 2005. The TAC found that "this project has been brought to a state that can meet the requirements for a DOE Major Item of Equipment project, to be funded in FY 2006." The TAC made several technical advices. We continue the R&D along with the advices given by the TAC. The project has been included as MIE in president's budget proposal starting in FY07.

5.2 The management plan for the VTX

PHENIX management structure

The VXT project is part of the PHENIX project and as such integrated into the PHENIX management structure as described by the PHENIX bylaws. The PHENIX Detector Council (DC) will advise PHENIX management on the design, construction, and integration of the VXT. The DC is co-chaired by the operations manager (E.O'Brien) and the upgrades manager (A. Drees). The VTX subsystem manager will serve as a member of the DC.

Role of BNL

Because we expect that all DOE funding for this effort will be directed through the BNL Physics Department, BNL line management will have ultimate fiscal and management responsibility for the construction of the VTX and for its subsequent operation.

VTX Project Organization

The VTX project office consists of the project manager and the deputy project manager, along with the project electrical and mechanical engineers. In general, the project manager is responsible for the scientific management of the project, the deputy project manager is responsible for the delivery of the DOE portion of the VTX. The project engineers are responsible for the electronic and mechanical oversight of both the strip and pixel subsystems.

The full VTX project office will meet regularly as a group as well as with the PHENIX management to assure that the project meets the performance and budget goals.

The project manager is Y. Akiba, RIKEN.
The deputy project manager is C. Ogilvie, Iowa State University.
The electronic project engineer is E. Mannel, Columbia University
The mechanical project engineer is W. Sondheim, LANL.

Under the VTX project office, there are four subsystem managers. Each of the subsystem managers is responsible for one of four major subsystems: strip detector, pixel detector, integration, and software. The subsystem managers and deputy subsystem managers are:

- Pixel detector: Atsushi Taketani (RIKEN)
- Strip detector: Abhay Deshpande (Stony Brook) and Rachid Nouicer (deputy, BNL)
- Integration: Robert Pak (BNL)

- Software: Alexandre Lebedev (ISU)

The subsystem managers report directly to the VTX project office and will be responsible for the design, construction, installation, and testing of their subsystem in accordance with the performance requirements, schedule, and budget.

The organization chart of the VTX project is shown in
Figure 107.

Details of the responsibilities of the project manager, the deputy project manager, the project engineers, and the subsystem managers are described in the management plan for the Silicon Vertex Tracking Detector (VTX) for the PHENIX.

Details on the management personnel can be found in Table 10.

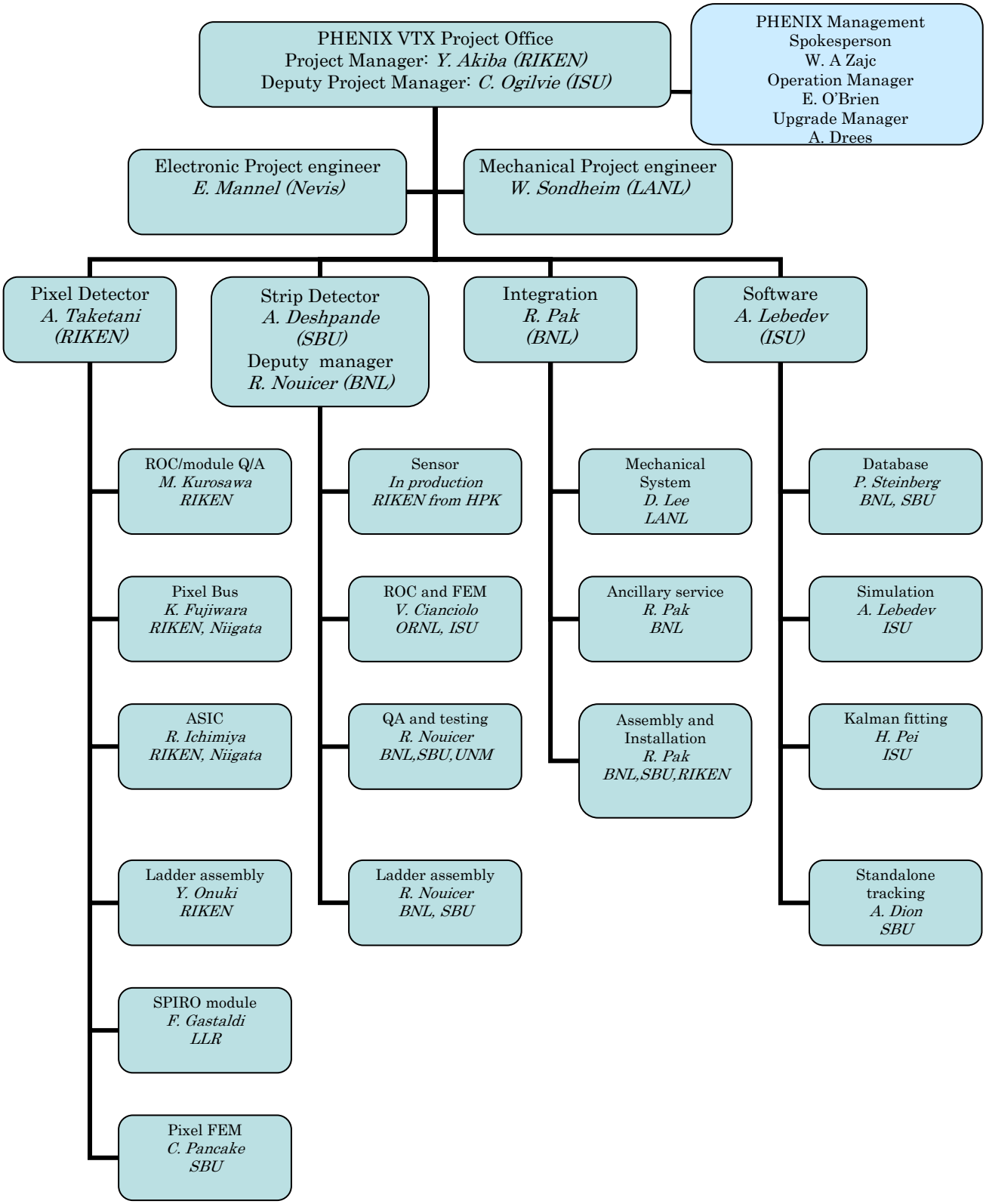

Figure 107 Management chart of the VTX project. The fiscal responsibilities for the individual tasks are specified in bold letters. The institutions participating in each task are given in italic. In PHENIX the DAQ is a separate subsystem and therefore not connected to the VTX management.

Table 10 Professional Background of the leaders in the VTX project.

	People	VTX FTE now	VTX FTE after 2007	Experience
VTX project Office	Project Manager Yasuyuki Akiba (RIKEN)	50%	100%	Managed construction and installation of RICH for PHENIX, approximate budget $10M. Physics Working Group convener for PHENIX. A deputy spokesperson of PHENIX.
	Deputy Project Manager Craig Ogilvie (ISU)	50%	100%	Led PHENIX Silicon study group. Managed construction, installation of multiplicity counter for E866 AGS. Physics Working Group convener for STAR and PHENIX
Project Engineers	Electrical Engineer E. Mannel (Columbia)	100 %	100%	Electronics of HiRes cosmic ray experiment
	Mechanical Engineer W. Sondheim (LANL)	25 %	50%	Mechanics of PHENIX Muon Tracking system
Subsystem manager	Pixel Manager Atsushi Taketani (RIKEN)	100%	100%	Lead RIKEN group for the development of the pixel detector. Lead the RIKEN part of PHENIX MuID construction
	Strip Manager Abhay Deshpande (Stony Brook)	50%	100%	Several years experience in PHENIX, managed design and installation of the New Trigger Counter.
	Deputy Strip Manager R. Nouicer (BNL)	100%	100%	Several years of experience in Si detector in Phobos. Lead the strip Q/A test effort at BNL for > 1 year.
	Auxillary Systems and Integration Manager Robert Pak (BNL)	100%	100%	Several years in PHOBOS as RHIC Liaison. Responsible for day-to-day operations in PHOBOS.
	Software A. Lebedev (ISU)	50%	100%	Oversee simulations, reconstruction, DCA, efficiency calculations.

Deliverables

The requirements and the deliverables of the VTX project are described in the management plan. Here we list the major items and its responsibilities.

Silicon strip detectors:

- Silicon strip sensors designed and tested to specifications (RIKEN)
- SVX4 readout cards (ROC's) developed and manufactured (DOE)
- Strip sensors integrated with ROC's (DOE)
- Pilot modules to readout ROC's from detector assembly (DOE)
- Front-end modules (FEM's) to collect data from pilot modules (DOE)
- Detector ladder, sensors-ROC's assemblies with pilot module mounted on readout bus (DOE)
- Commissioning of strip detector ladders (DOE)

Silicon pixel detectors:

- Tested sensor assemblies which include one sensor and 4 readout chips (RIKEN)
- Readout bus to read data from sensor assemblies manufactured and tested (RIKEN)
- Two sensor ladders mounted on readout bus and tested (RIKEN)
- SPIRO modules (IN2P3/Ecole Polytechnique)
- Half ladders, combining readout bus, two sensor ladders assembled and tested (RIKEN)
- Assembly and commissioning of half ladders to full ladders (RIKEN)
- Front-end modules (FEM's) (StonyBrook, funded by RIKEN)

DAQ system

- Data collection modules for pixel and strip detector manufactured and tested (DOE)

Mechanical Systems and Integration

- System support requirements specified, including heat loads, power distribution, mechanical tolerances and ground scheme (DOE)
- Mechanical support structure designed and manufactured (DOE)
- Ancillary systems operational, including power distribution and cooling system (DOE)
- Strip and pixel detectors ladders mounted in mechanical support (DOE)
- Full system tested in assembly laboratory (DOE)
- Commissioning of full detector system (DOE)
- VTX installed at final location in PHENIX experimental (DOE)
- Full system test in PHENIX (DOE)
- Integration into PHENIX DAQ system (DOE)

5.3 Institutional participation

Currently 20 institutions with a total of 97 collaborators participate in the VTX project. The institutions and their anticipated project responsibilities are listed in Table 11.

Table 11: VTX Project Institutional Participation

Institution	Project Responsibility and participation
Brookhaven National Laboratory (BNL chemistry, BNL physics, and BNL Instrumentation Division)	Database software Detector infrastructure Strip sensor Strip detector Q/A, testing, assembly VTX detector assembly VTX detector integration to PHENIX E,S,H&Q
Charles University (Czech)	Pixel testing, software
Columbia University	VTX detector electrical integration Oversight of electrical system DCM
Ecole Polytechnique (France)	SPIRO module
Florida State University	Simulation study
Iowa State University	Project management Software Strip FEM
Institute of Physics, Academy of Science, Prague (Czech)	Pixel testing, software
KEK (Japan)	Pixel assembly
Kyoto University (Japan)	Simulation study
Los Alamos National Laboratory	Mechanical system Oversight of the mechanical system
Niigata University (Japan)	Pixel bus, Pixel Q/A and testing
OakRidge National Laboratory	Strip ROC, strip FEM
RIKEN (Japan) and RBRC	Project management Pixel ASIC, Pixel Q/A and testing Pixel bus, Pixel assembly Strip sensor, SVX4 chip
Rikkyo University (Japan)	Strip sensor testing
Stony Brook University	Pixel FEM Strip detector Q/A, testing, assembly
Tokyo Institute of technology (Japan)	Pixel Q/A and testing
University of New Mexico	Strip Q/A and testing

5.4 Foreign contributions

The VTX project is funded in part by the RIKEN Institute. The tasks for which the RIKEN Institute has taken fiscal responsibilities are identified in the project chart (
Figure 107) and are given in more detail below:

Outer layer silicon strip detectors:

- Silicon strip sensors designed and tested to specifications (RIKEN)
- Strip sensors integrated with ROC's (RIKEN)

Inner layer silicon pixel detectors:

- Tested sensor ladders which include one sensor and 4 readout chips (RIKEN)
- Readout bus to read data from sensor ladders manufactured and tested (RIKEN)
- Two sensor ladders mounted on readout bus and tested (RIKEN)
- SPIRO modules to readout and to control pixel half ladders (IN2P3)
- Half ladders, combining readout bus, two sensor ladders and pilot module assembled and tested (RIKEN)
- Assembly and commissioning of half ladders to full ladders (RIKEN)

To enhance the expertise to carry out the work RIKEN has initiated several co-operations with the BNL Instrumentation Division on silicon strip sensors and with the ALICE/CERN pixel group on the silicon pixel detectors. For the pixel hybrid detectors a memorandum of understanding between RIKEN and CERN is in place. The objective of the memorandum is the delivery of silicon pixel hybrids developed for the ALICE experiment at CERN to RIKEN

6 Budget and schedule

6.1 Total estimated cost (TEC)

The costs and schedule for the VTX project have been developed using engineering estimates, vendor quotes and experience from the construction of the silicon pixel detector for NA60 and ALICE. The proposed project is based on a cost sharing between the DOE Office of Nuclear Physics and the RIKEN Institute of Japan. Responsibilities for specific deliverables have been discussed in the previous chapter. RIKEN funding started in April 2003 and has provided approximately $3M per year for three years. In addition, RIKEN provides substantial manpower (equivalent to ~ $1M) through in house contributions. The total estimated costs for the proposed DOE construction project is $4.6 M in actual dollars for FY07 through FY09 including an average contingency of 26%. We have implemented a work breakdown structure (WBS), which is the basis for the following is a more details on the cost estimate and schedule.

Fiscal Responsibilities

Table 12 summarizes the mapping of the major construction tasks onto the proposed fiscal responsibility as discussed in the previous section. Completion of some of these tasks will require collaboration and expertise from institutions funded through the DOE as well as from foreign institutions. In order to proceed with the project in a timely manner and to bring technologies ready as soon as possible, R&D and prototype cycles for some of the major tasks have been developed based on both DOE and RIKEN funding.

Table 12 Map of construction tasks and WBS numbers onto the proposed fiscal responsibilities.

WBS	Construction Task	DOE	RIKEN/IN2P3
1.1	**Silicon Barrel**		
1.1.1	**Strip Detector**		
1.1.1.1	Strip FEE	X	
1.1.1.2	Strip Sensor		X
1.1.1.3	Strip System test	X	
1.1.1.4	Strip Assembly and test	X	
1.1.2	**Pixel Detector**		X
1.2	**DAQ**	X	
1.3	**Electronic system Integration**	X	
1.4	**Auxiliary Systems and Integration**	X	
1.5	**Management**	X	
1.6	**Installation and pre-ops**	X	

Contingency Analysis

Contingency is the amount of money, above and beyond the base cost, that is required to ensure the project's success. This money is used only for omissions and unexpected difficulties that may arise. Contingency funds are held by the Project Manager. The contingency % is calculated for each WBS item as

Cont % = technical risk factor ×Base% + cost risk factor ×Base% + schedule risk factor ×Base%

For the majority of the project, Base%=7.5%, the exception is the strip FEE cost estimates where the Base% is evaluated for different items and ranges from 4 to 10%.

Risk Factors

Technical Risk – Based on the technical content or technology required to complete the element, the technical risk indicates how common the technology is that is required to accomplish the task or fabricate the component. If the technology is so common that the element can be bought "off-the-shelf", i.e., there are several vendors that stock and sell the item, it has very low technical risk, therefore a risk factor of 1 is appropriate. On the opposite end of the scale are elements that extend the current "state-of-the-art" in this technology. These are elements that carry technical risk factors of 4. Between these are: making modifications to existing designs (risk factor 1.5), creating a new design which does not require state-of-the-art technology (risk factor 2, and creating a design which requires R&D, and advances the state-of-the-art slightly (risk factor 3).

Cost Risk – Cost risk is based on the data available at the time of the cost estimate. It is subdivided into 4 categories.

The first category has a risk factor between 1 and 2. It includes elements for which there is a recent price quote from a vendor or a recent catalog price. If the price of the complete element, or the sum of its parts, can be found in a catalog, the appropriate risk factor to be applied is 1. If there is an engineering drawing or specification for the element, and a reliable vendor has recently quoted a price based on these, the cost risk factor to be applied is between 1 and 2.

The second category has a risk factor of 2. It includes elements for which there exists some relevant experience, e.g. if the element is similar to

something done previously with a known cost, or if the element is something for which there is no recent experience, but the capability exists.

The third category has a risk factor of 3. It includes is for elements for which there is information that, when scaled, can give insight into the cost of an element or series of elements.

The fourth category has a risk factor of 4. It includes is for elements for which there is an educated guess, using the judgment of engineers or physicists.

Schedule Risk – If a delay in the completion of the element could lead to a delay in a critical path or near critical path component, the schedule risk is 3. If a delay in the completion of the element could cause a schedule slip in a subsystem which is not on the critical path, the schedule risk is 2. Only elements where a delay in their completion would not affect the completion of any other item have schedule risks of 1.

Overhead Estimate

All manpower costs are quoted as fully loaded numbers, i.e. including overhead and benefits. The M&S overheads are calculated with the current overhead rules in BNL, ORNL, LANL, and Universities. Also listed as overhead are 18% for the first $600K of any funds that are transferred from BNL to an institution. When this transfer overhead can be avoided, e.g. between national labs, the transfer overhead rate is zero.

Budget

Table 13 and 14 summarize the estimated costs for the VTX project for the DOE project. For those items for which we seek funding through the DOE, a detailed cost-breakdown is given in Table 13. The cost of the DOE is after the start of the construction in FY07. Both of the Total Estimated Cost (T.E.C.) for the construction and Total Project Cost (T.P.C = T.E.C plus installation and pre-ops) are shown. The amounts are in FY07 dollars. An inflation rate of 2% for materials and 4% for manpower is compounded for FY07 through FY09 results in the Total Project Cost of 4.6M in at year (AY) dollars.

Table 13 The cost summary for the PHENIX VTX construction project. Amounts are in FY07 kilo-dollars.

WBS	Name	Material k$	Manpower k$	BNL Transfer k$	Contingency %	Conting. k$	TEC k$	Preops k$	TPC k$
1	VTX project	1,522	1,824	195	26	912	4,455	105	4,560
1.1.1	Strip	624	740	5	26	360	1,730	0	1,730
1.1.1.1	Strip FEE	494	631	0	24	267	1,393	0	1,393
1.1.1.2	Strip Sensor	29	0	2	29	9	40	0	40
1.1.1.3	Strip System test	9	24	0	42	14	47	0	47
1.1.1.4	Assembly and Testing of Strip ladders	92	85	4	39	70	250	0	250
1.2	DAQ	99	30	23	25	38	191	0	191
1.3	Electronics System Integration	139	348	59	21	116	662	0	662
1.3.1	electronics oversight	0	330	59	18	71	460	0	460
1.3.3	Electronic Services	139	18	0	29	45	202	0	202
1.4	Auxillary Systems & Integration	660	652	98	27	386	1,796	0	1,796
1.4.2	Mechanical Structure	511	247	94	31	264	1,116	0	1,116
1.4.3	Assembly of ladders onto barrel	39	30	4	30	22	95	0	95
1.4.4	Infrastructure	110	108	0	23	51	269	0	269
1.4.5	Mechanical system Integration	0	267	0	18	49	315	0	315
1.5	Management	0	55	10	18	12	77	0	77
1.6	Installation	0	0	0	30	0	0	105	105

Table 14 The budget Profile of the VTX Project. An inflation rate for 2% for material and 4% for manpower is assumed in the AY dollars.

WBS	Name	TPC		FY07 AY k$	FY08 AY k$	FY09 AY k$	FY10 AY k$	TPC AY k$
1	VTX project	4,560		1,990	2,027	554	95	4,666
1.1.1	Strip	1,730		718	920	128	0	1,766
1.2	DAQ	191		0	195	0	0	195
1.3	Electronics System Integration	662		173	404	106	0	683
1.4	Auxiliary Systems & Integration	1,796		1,070	475	281	0	1,826
1.5	Management	77		29	33	18	0	80
1.6	Installation	105		0	0	21	95	116

6.2 Schedule

The following plots summarize the construction schedule to complete the VTX detector upgrade for PHENIX. The overall schedule is shown in Figure 108. It assumes start of the DOE construction project in FY07. The subsequent plots, Figure 109 to Figure 112, show the detailed schedule for each major WBS element.

Figure 114 gives the funding profile for the DOE project. In this schedule the VTX detector will be completed in summer 2009 shutdown to be ready for RUN10.

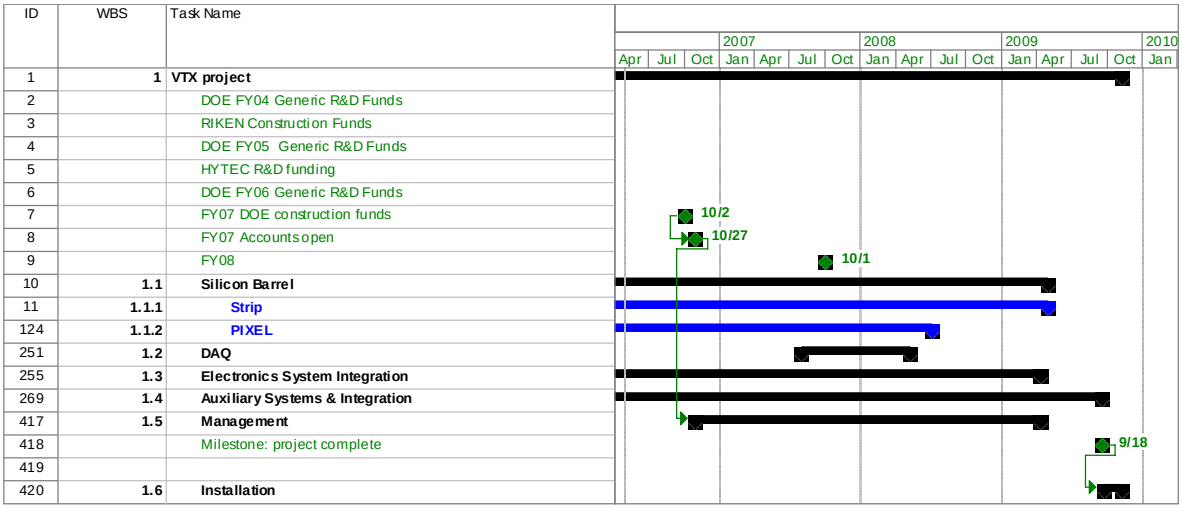

Figure 108 The overall schedule for the VTX Project.

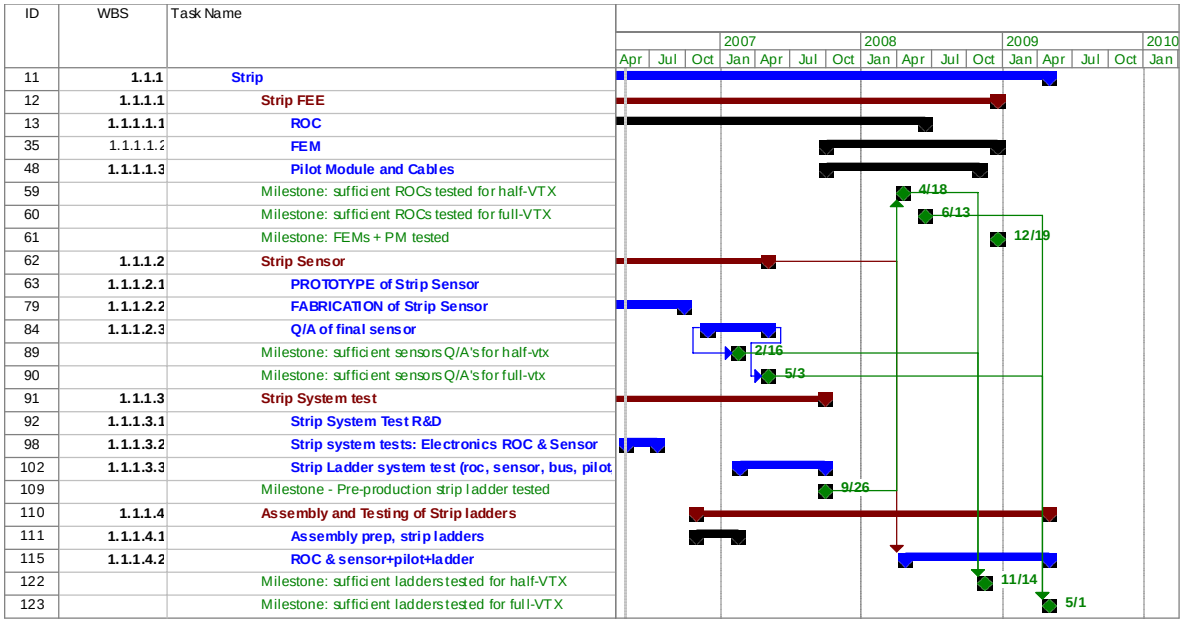

Figure 109 The schedule for the strip layers.

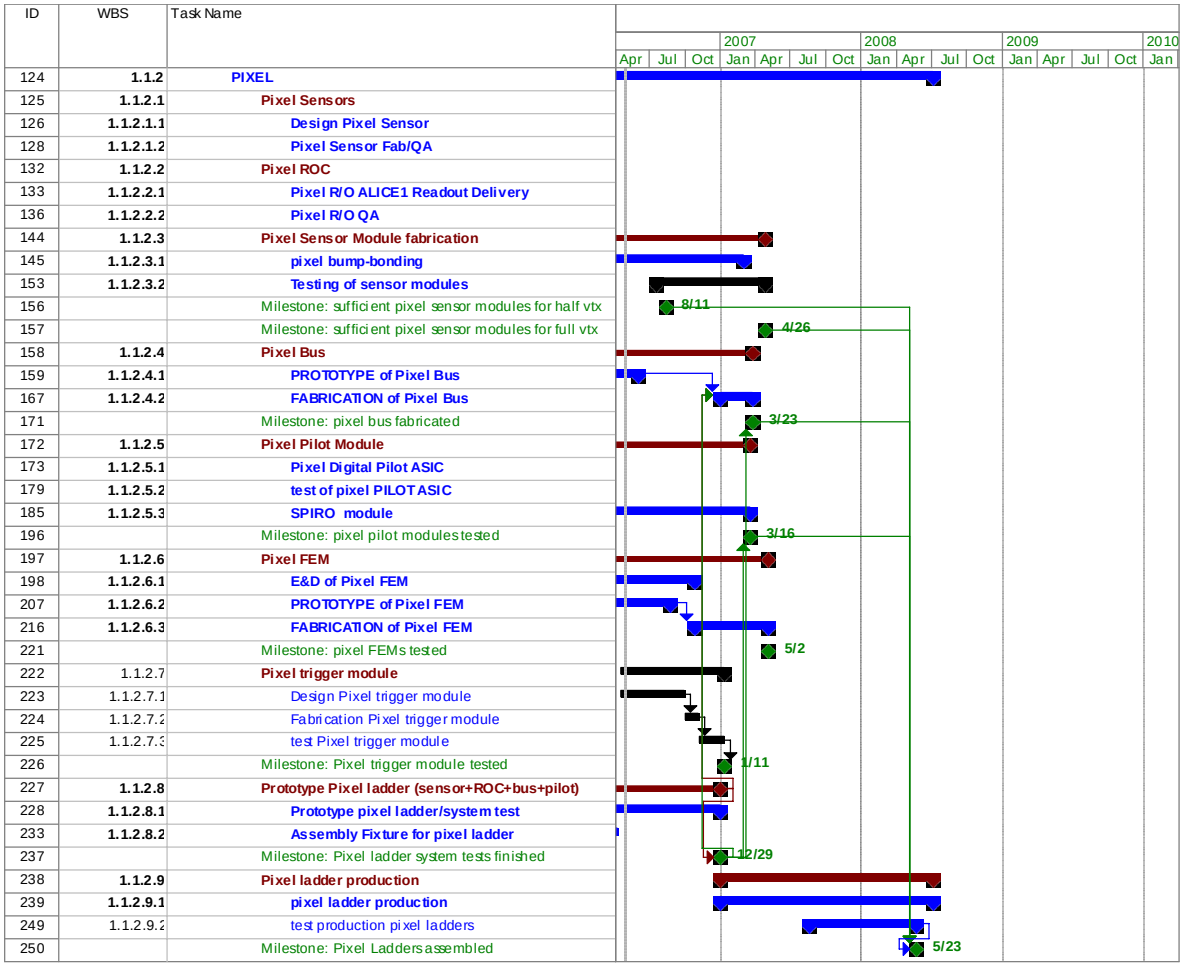

Figure 110 The schedule for the pixel layers

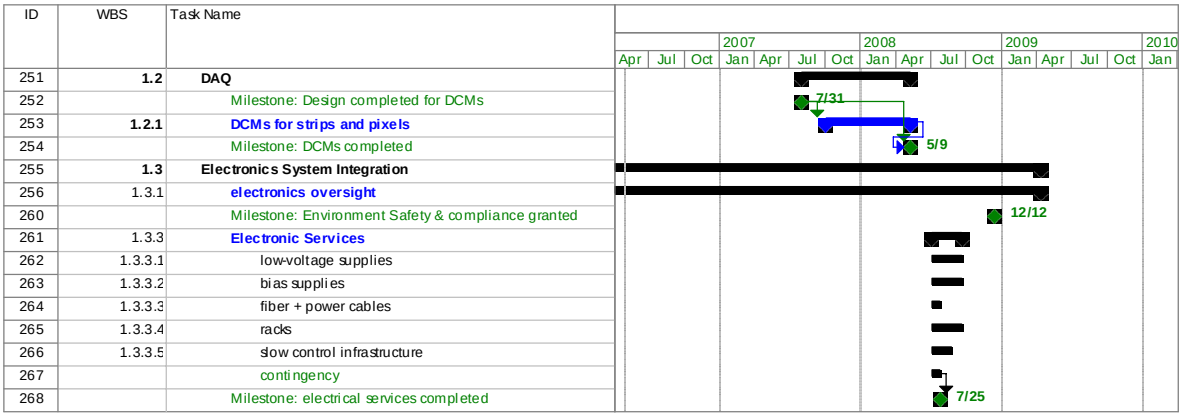

Figure 111 The schedule for DAQ amd Electonics infrastructure

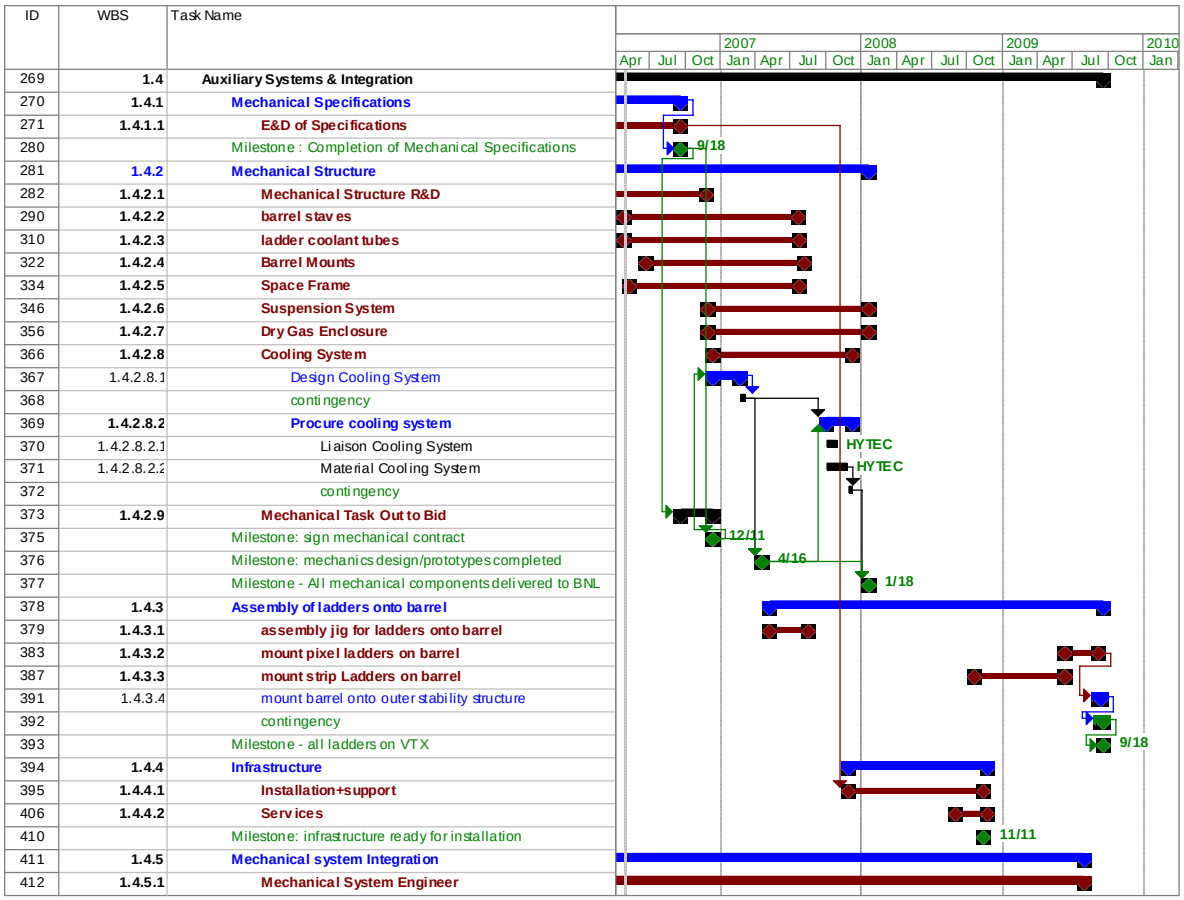

Figure 112 The schedule for the auxiliary systems and infrastructure

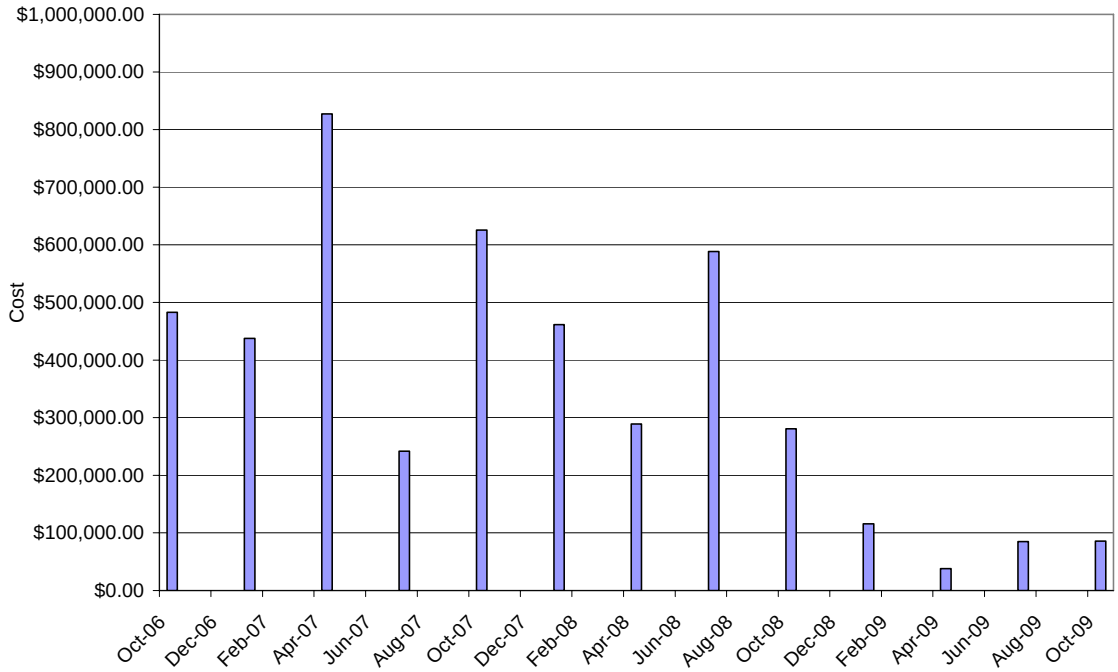

Figure 113 TPC per quarter of the VTX project in FY07 dollars

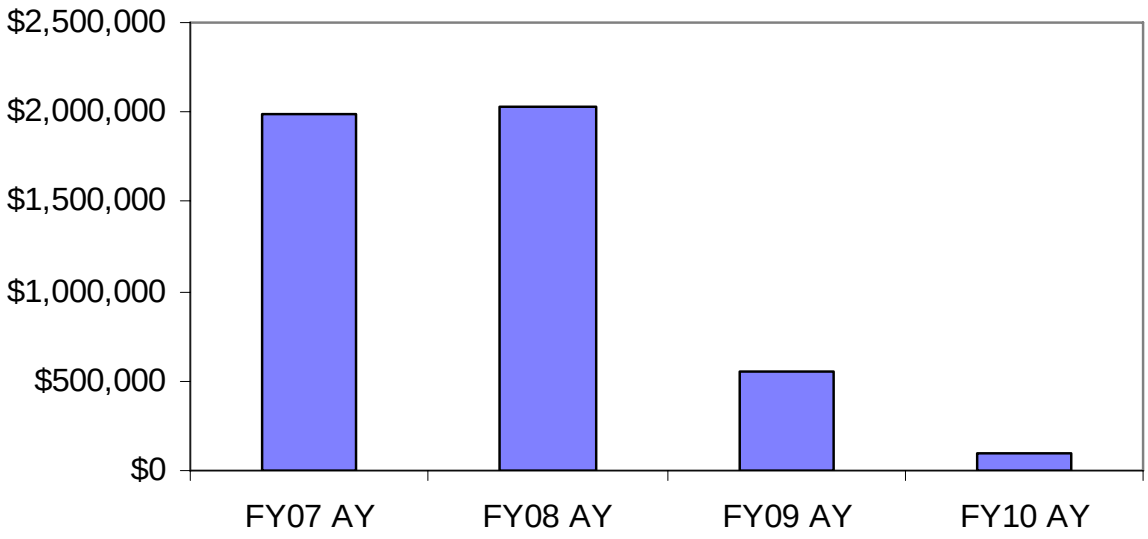

Figure 114 Budget profile for the VTX project

[1] K. Adcox et al., Nucl. Phys. A757, 184 (2005).

[2] I. Arsene et al., Nucl. Phys. A757, 1(2005).

[3] B. B. Back et al., Nucl. Phys. A757, 28 (2005).

[4] ; J. Adams et al., Nucl. Phys. A757, 102 (2005).

[5] K. Adcox et al., Phys. Rev. Lett. 88, 19203 (2002).

[6] S. S. Adler et al., Phys. Rev. Lett. 94,082301 (2005).

[7] S. S. Adler et al., Phys. Rev. Lett. 96, 032301 (2006).

[8] R. Baier, D. Schiff, B.G. Zakharov, Ann. Rev. Nucl. Sci 50, 37 (2000).

[9] U.A. Wiedemann, Nucl. Phys. B 588, 303 (2000)

[10] M. Gyulassy et al., Nucl. Phys. B594, 371 (2001)

[11] K. Adcox et al., Phys. Rev. Lett. 88, 022301 (2002).

[12] S. S. Adler et al., Phys. Rev. Lett. 91, 072301 (2003).

[13] S. S. Adler et al., Phys. Rev. Lett. 91, 072303 (2003).

[14] S. S. Adler et al., Phys. Rev. Lett. 94, 232301 (2005).

[15] Y. Akiba (for PHENIX), nucl-ex/0510008 (2005)

[16] Yuri L. Dokshitzer, D.E. Kharzeev Phys.Lett.B519:199-206 (2001)

[17] M. Djordjevic and M. Gyulassy, Phys. Rev. C68, 034914 (2003)

[18] M. Djordjevic and M. Gyulassy, Phys. Lett. B.560, 37 (2003)

[19] B. H. Zhang, E. Wang, X-N. Wang, Phys. Rev. Lett 93, 072301 (2004)

[20] S. S. Adler et al., Phys. Rev. Lett. 96, 032301 (2006).

[21] S. Butsyk (for PHENIX), nucl-ex/0510010 (2005).

[22] N. Armestron et al., Phys. Rev D71, 054027 (2005).

[23] M. Djordjevic et al., Phys. Lett. B632, 81 (2006).

[24] M.C. Abreu et al (NA50), Phys. Lett. B410, 327 (1997).

[25] B.Z. Kopeliovich and A.V. Tarasov, Nucl. Phys. A710, 180 (2002); J. Raufeisen private communication.

[26] L. Grandchamp and R. Rapp, Phys. Lett. B523, 60 (2001).

[27] A. Andronic et al., Phys Letters B571, 36 (2003)

[28] R.L.Thews, et al., Phys. Rev. C63, 054905(2001)

[29] C.Lourenco, “Workshop on Quarkonium Production in Relativistic Nuclear Collisions”, Seattle, 11 May 1998, B-> J/Psi estimates, private communication.

[30] E. Shuryak Phys. Rep 61, 71 (1980)

[31] P. Levai et al, Phys. Rev C. 51, 3326 (1995)

[32] Z. Lin and M. Gyulassy, Phys. Rev. C. 51, 2177 (1995)

[33] R. Rapp, nucl-th/0204003

[34] S. S. Adler et al., nucl-ex/0507004 (2005).

[35] J. Casalderey-Solana et al., J. Phys. Conf. Ser. 27, 22 (2005).

[36] A. Majumder and X.-N. Wang, nucl-th/0507062.

[37] M. Arnedo, Phys. Rep. 240, 301 (1994); K.J. Eskola et al., Nucl. Phys. A661, 645 (1999).

[38] L. McLerran and R. Venugopalan, Phys. Rev. D49, 2233 (1994); A.H. Mueller and J.W. Qui, Nucl. Phys. B 268 427 (1986); L.V. Bribox, E.M. Levin and M.G. Ryskin, Phys. Rept. 100, 1 (1983).

[39] L. Frankfurt, M. Strikman, Eur. Phys. J A5, 293 (99)

[40] B.Z. Kopeliovich, A.V. Tarasov and J. Huefner, Nucl. Phys. A696, 669 (2001).

[41] K.J. Eskola, V.J. Kolhinen and R. Vogt, Nucl. Phys. A696, 729 (2001).

[42] D. Kharzeev, Nucl. Phys. A702, 39 (2002).

[43] L. Frankfurt and M. Strikman, Eur. Phys. J A5, 293 (99)

[44] M.A. Vasiliev et al. (E866/NuSea), Phys. Rev. Lett. 83, 2304 (1999).

[45] Heijne, E.H.M., Nucl. Instrum. Methods Phys. Res. A465 (2001) 1-26

[46] W. Snoeys et al., Nucl. Instr. Meth. Phys. Res. A465 (2001), 176; K. Wyllie et al., Proc. Fifth Workshop on Electronics for LHC Experiments, Snowmass, Colorado, 1999.

[47] NA60 Collaboration, CERN/SPSC 2000-010, March 2000;

[48] Jorma Salmi and Jaakko Salonen, VTT, Finland, Workshop on Bonding and Die Attach Technologies CERN, Geneva, Switzerland, June 11-12, 2003,
`http://ssd-rd.web.cern.ch/ssd-rd/bond/talks/1-04_Salmi.pdf`

[49] P. Riedler, CERN, Workshop on Bonding and Die Attach Technologies CERN, Geneva, Switzerland, June 11-12, 2003,
`http://ssd-rd.web.cern.ch/ssd-rd/bond/talks/2-01_Riedler.pdf`

[50] V. Eremin *et al.*, Nucl. Instr. and Meth. A **372**, 388 (1996).

[51] Ideas ASA (Norway), http://www.ideas.no/